VTT PUBLICATIONS 266

# Detection of knots in logs using x-ray imaging

Markku Pietikäinen

VTT Electronics

*Dissertation for the degree of Doctor of Technology to be presented, with the permission of the Department of Electrical Engineering of the University of Oulu, for public discussion in the Auditorium L5, Linnanmaa, on March 8th, 1996, at 12 o'clock noon.*

TECHNICAL RESEARCH CENTRE OF FINLAND
ESPOO 1996

ISBN 951-38-4924-4
ISSN 1235-0621


JULKAISIJA – UTGIVARE – PUBLISHER

Valtion teknillinen tutkimuskeskus (VTT), Vuorimiehentie 5, PL 42, 02151 ESPOO
puh. vaihde (90) 4561, telekopio 456 4374, teleksi 125 175 vttin sf

Statens tekniska forskningscentral (VTT), Bergsmansvägen 5, PB 42, 02151 ESBO
tel. växel (90) 4561, telefax 456 4374, telex 125 175 vttin sf

Technical Research Centre of Finland (VTT), Vuorimiehentie 5, P.O.Box 42, FIN–02151 ESPOO, Finland
phone internat. + 358 0 4561, telefax + 358 0 456 4374, telex 125 175 vttin sf

VTT OFFSETPAINO, ESPOO 1996

Pietikäinen, Markku. Detection of knots in logs using x-ray imaging. Espoo 1996,
Technical Research Centre of Finland, VTT Publications 266. 70 p. + app. 18 p.
**UCD** 674.09:658.562:778.33
**Keywords** knots, detection, logs, structural timber, x-rays, x-ray inspection, quality, quality control, properties, computers, tomography

# ABSTRACT

The economy of the sawing process would be greatly improved, if the internal properties of logs were known beforehand. The output quality would be more predictable, resulting in a higher yield and better utilisation of timber.

Our fundamental idea was to apply the principles of computed tomography (CT) to knot detection in logs. CT is a standard method in medical applications for internal diagnosis of the human body. Unfortunately, the high-speed sawing process leaves a very limited time for log imaging. Rotation or multiple passes cannot be used to obtain hundreds of projections of a log; thus a detailed reconstruction in the sense of CT is not possible. However, we found that even from three fixed projections valuable information can be acquired. This was demonstrated by analysing images of both simulated and real logs. An x-ray imaging system was constructed to measure full-sized logs moving at normal sawing speeds. At the first stage, only one source-detector pair was available; thus three passes per log were needed in the tests.

A new method was developed for computing 3-D properties of knot clusters. We call it the *sector oriented reconstruction technique*, or SORT. The name refers to the principle of applying a cylindrical co-ordinate system with discrete sectors, rings, and slices. The object space is composed of volume elements with dimensions far larger than the imaging pixel size. The densities of the volume elements are estimated to recognise potential knot locations and sizes. The method uses *a priori* knowledge of typical shapes and densities of knots and stems, along with evidential reasoning when looking for candidate knot directions.

The method produces estimates of knot characteristics at two levels: (1) volumes and co-ordinates of knot clusters, and (2) thicknesses, lengths, volumes, and co-ordinates of individual knots. In some cases, the information from three projections is not enough to separate out individual knots. A confidence index is therefore calculated to indicate the reliability of the results.

The performance of the detection algorithms was tested with data from simulated and real logs. For real logs the relative volumes of detected, undetected, and ghost knots were 0.88 : 0.12 : 0.15, and for simulated logs 0.96 : 0.04 : 0.02.

# PREFACE

This thesis is based on my work in a series of projects ordered by Bintec Oy from the Technical Research Centre (VTT), Computer Technology Laboratory, Oulu, Finland.

I wish to thank Prof. Matti Pietikäinen, the supervisor of this thesis at the University of Oulu, for his comments and guidance. I am grateful to Prof. Hannu Hakalahti, the former laboratory director, for providing me the opportunity to do the research at VTT. I appreciate the constructive criticism from Prof. Arto Usenius and Asst. Prof. Juha Röning who reviewed the manuscript. Special thanks are addressed to the *primus motor* of the project, Dr. Antti Kari, managing director of Bintec Oy.

I had many useful discussions with my colleagues at VTT, first of all with Heikki Ailisto, Tuomas Ihme, and Kari Leppälä. Their co-operation is gratefully appreciated. I am greatly indebted to several persons for helping me to arrange the experiments involved. Especially, I would like to mention Mr. Viljo Pietikäinen at the Oulu University Central Hospital, Ms. Liisa Sarasoja and Mr. Markku Heikkinen at Kullaan metsä- ja puutalousoppilaitos, and Mr. Tapio Saukkonen and Mr. Juha Peltonen at the Helsinki University of Technology, Department of Mechanical Engineering. Thanks are also owed to Mr. Gordon Roberts for revising the language of the manuscript.

Financial support from VTT, Tauno Tönningin Säätiö, and Tekniikan Edistämissäätiö is gratefully acknowledged.

Finally, I wish to thank my wife Raija and my daughters Terhi and Elina, for their patience and understanding during my studies.

Oulu, 12th January, 1996

Markku Pietikäinen

# CONTENTS

# LIST OF SYMBOLS

| | |
|---|---|
| $a$ | coefficient in the attenuation law |
| $\mathbf{A}$ | projection matrix |
| $a(i, j)$ | sum of coefficients $c(h, i, j)$ related to sector element $(i, j)$ |
| ART | algebraic reconstruction technique |
| $B$ | build-up coefficient in the attenuation law |
| $b$ | coefficient in the attenuation law,<br>belief value |
| C | scaling constant in the pixel calibration |
| $c(h, i, j)$ | backprojecting coefficient |
| $c_\rho$ | density correction coefficient |
| $c_\rho(j)$ | density correction coefficient for ring $j$ |
| CT | computed tomography |
| CT-100 | a medical CT scanner |
| $d$ | knot diameter |
| $D$ | mean deviation |
| $d_{dark}$ | output of a detector element with no radiation |
| $d_{full}$ | output of a detector element with full radiation |
| $d_{lin}$ | linearised output of a detector element |
| $d_{norm}$ | calibrated output of a detector element |
| $d_{out}$ | measured output of a detector element |
| $d_1$ | distance from the x-ray source to the log axis |
| $d_2$ | distance from the x-ray source to the detector |
| $E$ | energy |
| $\mathbf{e}$ | error vector |
| E | evidence combining operator |
| $e$, $e_0$, $e_1$, $e_2$, $e_3$ | evidence values |
| $e_c(i, j, k)$ | evidence of volume element $(i, j, k)$ combined from all projections |
| $e_m(i, j, k)$ | evidence of volume element $(i, j, k)$ calculated from projection $m$ |
| $e_s(i, \beta)$ | evidence of sector $i$ at rise angle $\beta$ |
| $e_r(i, j, \beta)$ | evidence of sector element $(i, j)$ at rise angle $\beta$ |
| $e_{th}$ | evidence threshold |
| $e_t(i)$ | evidence of sector $i$ |
| $e_0(i, j, k)$ | evidence of volume element $(i, j, k)$ calculated from projection 0 |
| $e_1(i, j, k)$ | evidence of volume element $(i, j, k)$ calculated from projection 1 |
| $e_2(i, j, k)$ | evidence of volume element $(i, j, k)$ calculated from projection 2 |
| $f_i$ | fraction of an element in a material |
| $F(j, k, \beta)$ | auxiliary function for estimating rise angle $\beta$ |
| $f(x, y)$ | two-dimensional image function in Cartesian co-ordinates |
| $f(\omega, r)$ | two-dimensional image function in polar co-ordinates |
| GE9800 | a medical CT scanner |
| $G(j, k, \beta)$ | auxiliary function for backprojection |
| $h$ | detector element index |

| | |
|---|---|
| $h_c$ | index of the central element of the detector |
| $h_k$ | index corresponding to the knot boundary in a cluster |
| $h_l$ | left edge of the log |
| $h_l(k)$ | left edge of the log in slice $k$ |
| $h_{lm}$ | left edge in projection $m$ |
| $h_{max}(i, j)$ | maximum of index $h$ for non-zero coefficients $c(h, i, j)$ |
| $h_{min}(i, j)$ | minimum of index $h$ for non-zero coefficients $c(h, i, j)$ |
| $h_r$ | right edge of the log |
| $h_r(k)$ | right edge of the log in slice $k$ |
| $h_{rm}$ | right edge in projection $m$ |
| $h_1$, $h_2$ | limits of summing index $h$ |
| **i** | image column vector |
| $i$ | sector index |
| $I_k$ | set of knot sectors |
| $i_m$ | sector index $i$ with phase shift $m \cdot 120°$ |
| $i_{max}$ | maximum value of $i$ |
| Ir192 | a radioactive isotope used as photon source |
| $i_1$ | sector index $i$ with phase shift 120° |
| $i_2$ | sector index $i$ with phase shift 240° |
| $J$ | radiation intensity |
| $j$, $j_1$ | ring indices |
| $j_k$ | ring index corresponding to the cluster radius |
| $j_{max}$ | maximum value of $j$ |
| $j_t(i)$ | ring index corresponding to the length of a knot in sector $i$ |
| $J_0$ | incident radiation intensity |
| $k$ | slice index |
| $k_{max}$ | maximum value of $k$ |
| $k_{ref}$ | reference slice index |
| $k_1$, $k_2$ | indices referring to the top and bottom slices of a knot cluster |
| $L$ | length of the knot cluster |
| $l_s(h, k)$ | sum of coefficients $c(h, i, j)$ related to ray $h$ in slice $k$ |
| $l_{sm}(h)$ | sum of coefficients $c(h, i, j)$ related to ray $h$ in projection $m$ |
| LT | linearisation function |
| $M$ | number of projections |
| $m$ | projection index |
| MART | multiplicative algebraic reconstruction technique |
| $m_d$ | dry weight of wood |
| MENT | maximum entropy method |
| $m_f$ | fresh weight of wood |
| MOCT | moving object computer tomography |
| *m.p.* | moisture percentage |
| $m_1$ | statistical first moment of a data set |
| $m_2$ | statistical second moment of a data set |
| $n$ | number of elements in the detector |
| $N$ | number of radiation quanta penetrating material |
| $N_0$ | number of quanta generated by the radiation source |
| $p_a(h, k)$ | average of images $p_0$, $p_1$, and $p_2$ |
| PC | a microcomputer |
| P0, P1, P2 | imaging projections |

| | |
|---|---|
| $p_m(h, k)$ | projection image from direction $m \cdot 120°$ |
| $P_\theta(t)$ | projection function |
| $p_0(h, k)$ | projection image from direction 0° |
| $p_1(h, k)$ | projection image from direction 120° |
| $p_2(h, k)$ | projection image from direction 240° |
| $q$ | total number of samples in all projections |
| $Q(j, k)$ | collective reconstruction of a knot cluster |
| $q_h(i, j, k)$ | contribution of ray $h$ to element $(i, j, k)$ |
| $q_s(i, j, k)$ | estimated density of volume element $(i, j, k)$ |
| $Q_\theta(t)$ | filtered projection function |
| $\mathbf{r}$ | image column vector |
| $R$ | log radius at the knot cluster |
| $r$ | radial co-ordinate in the cylindrical co-ordinate system |
| $r_h$ | heartwood radius |
| $r_k$ | radius of a knot cluster |
| $r_m$ | cluster radius as seen from projection $m$ |
| $r_t(i)$ | distance of the knot end from the pith |
| $r_0, r_1, r_2$ | cluster radii in projections 0, 1, 2 |
| $s$ | a Cartesian co-ordinate,<br>sum of $S(i, j, k)$ |
| $S_a(i, j)$ | auxiliary sum array |
| $S(i, j, k)$ | 3-D array of the reconstructed image |
| SORT | sector-oriented reconstruction technique |
| $S_{rows}(k)$ | sum of pixels in slice $k$ |
| $t$ | total number of pixels in the reconstructed image,<br>threshold in edge detection,<br>a Cartesian co-ordinate |
| TINA | a gamma ray scanner |
| $u_m(i, j, k)$ | 3-D image backprojected from projection $m$ |
| $V$ | knot volume in a cluster |
| $V(i)$ | knot volume in sector $i$ |
| $V(i, j)$ | knot volume in sector $i$ and ring $j$ |
| $v(j)$ | volume of an element in ring $j$ |
| VTT | Technical Research Centre of Finland |
| $w(j, k)$ | shape mask function |
| $w_d$ | detector element width, detector pitch |
| $w_{d0}$ | detector element width projected onto the origin plane |
| $x$ | thickness of the radiated object,<br>a Cartesian co-ordinate |
| $y$ | a Cartesian co-ordinate |
| $z$ | longitudinal co-ordinate in the cylindrical co-ordinate system |
| Z-Scan | an x-ray imaging system |
| $z_0$ | starting longitudinal co-ordinate of a knot cluster |
| | |
| $\alpha$ | rotational angle in the cylindrical co-ordinate system |
| $\beta$ | rise angle of a knot |
| $\beta(i)$ | estimate of rise angle in sector $i$ |
| $\beta_{max}$ | maximum of $\beta$ |
| $\gamma$ | opening angle of a knot |

| | |
|---|---|
| $\delta$ | fraction variable |
| $\Delta\alpha$ | quantising step of $\alpha$ |
| $\Delta\beta$ | quantising step of $\beta$ |
| $\Delta r$ | quantising step of $r$ |
| $\Delta z$ | quantising step of $z$ |
| $\theta$ | projection angle |
| $\mu$ | linear attenuation coefficient |
| $(\mu/\rho)_i$ | mass absorption coefficient of an element |
| $(\mu/\rho)_m$ | mass absorption coefficient of a material |
| $\rho_{crit}$ | critical density |
| $\rho_k$ | knot density |
| $\rho_m$ | density of a material |
| $\rho_m(i, j, k)$ | density of volume element $(i, j, k)$ calculated from projection $m$ |
| $\rho_{max}$ | maximal density |
| $\rho_w$ | wood density |
| $\rho_{wh}$ | heartwood density |
| $\rho_{ws}$ | sapwood density |
| $\omega$ | rotational angle in the polar co-ordinate system |

| | |
|---|---|
| 2-D | two-dimensional |
| 3-D | three-dimensional |

# 1 INTRODUCTION

## 1.1 WHY INSPECT LOGS BEFORE SAWING THEM UP?

Trees are not created equal. This is unfortunate for a sawmill owner who would like to use homogeneous raw material for producing uniform-quality lumber for his customers. He faces the problem of how to match the varying properties of incoming timber and the product demand from the market, and specially, how to do this in an economic way.

Logs differ in their geometry and internal quality. The maximum dimensions of the sawn timber depend on the top-end diameter of the log and deformations such as crook and sweep. Internal defects like knots, cracks, or rot lower the value of the product. The basic goal of sawing is to produce boards that have as much clear face as possible.

The sawing process is irreversible: once sawn up, a piece of timber can only be accepted or rejected. If a product is rejected because of low quality, its value drops dramatically. On the other hand, sawing cheap products from high-quality timber is uneconomical. The solution to this optimising problem is log sorting.

At present, log sorting is based on visual inspection for surface defects and optical measurement of the top-end diameter. The logs are classified into 10 - 30 grades according to these properties. Each grade is then processed as a whole, using one single sawing set-up.

As one might expect, this kind of sorting is far too inaccurate for an individual log (Grönlund 1992). Even though a skilled operator may guess a lot about the internal quality of a log just by looking at its appearance, the frequency of misjudgements is high. Usenius (1988b) claims that only half of the logs are classified correctly by a human inspector. This percentage, of course, depends on the number of grades used.

With this background, it is natural to strive for better sorting of timber based on information about internal defects. Potential technologies for non-destructive detection of defects are gamma rays and x-rays combined with semiconductor detectors, which are fast enough for imaging moving logs.

Accurate grading would lead to a raised volume yield (square-edged sawn timber), thus improving the economic outcome. Grönlund (1992) estimates that the value increase of sawn timber would be in the range 7 - 10 %, if the internal defects were known. Usenius (1988b) states that the value of nearly knotless board is 3 - 5 times the value of knotty board. He also estimates that the value yield can be increased 5 - 15 % from the present level by using computed tomography (CT) to detect internal defects.

According to Zhu et al. (1991a), the first decision that must be made about a log is whether to saw it into lumber or to produce veneer. A correct decision to produce veneer can increase the log's value tenfold.

Hodges et al. (1990) have studied the economic potential of CT scanners for hardwood sawmills. The investment would be profitable for large mills, even with only moderate (5 %) increases in lumber value yields. They have calculated the cost of investment according to the prices of cur-

rent medical CT systems, even though the actual system construction would most probably be quite different.

If the internal properties of logs were well enough known, we also might think of applications other than just log sorting before sawing. Such applications are optimal positioning of the log, and quality pricing.

Usenius (1988a) estimates that the volume yield may increase by more than 10 %, if optimum positioning is used during the saw-up. This is quite in keeping with simulations by Wagner et al. (1989a), showing a 10.5 to 10.9 % increase in log value. Zhu et al. (1991a) reports a wider range of variation of improvement, from 7 up to 21 %.

Quality pricing is based on incoming inspection at the sawmill. It has been a standard procedure in Sweden for years, and is now planned to be adopted by some Finnish companies too. In quality pricing, the logs are graded individually to classes that fix the price. At the present time, the grading uses visual inspection and optical measurements. The accuracy and objectivity of the inspection would be much better if an automatic detection of internal defects were applied.

## 1.2 IMAGE RECONSTRUCTION FROM PROJECTIONS

As early as 1917, J. Radon showed that any object can be reconstructed if *all* of its projections are known (Herman 1980, pp. 279 - 283). On the other hand, Herman (1980, pp. 283 - 285) proves that a picture is not uniquely determined by any *finite* number of views. In practice, we are not looking for the exact solution, but are quite satisfied with an approximate solution containing only the substantial details of the original object. Plenty of experience of such reconstructions has been gained in both medical and industrial applications.

The method of reconstructing object cross-sections from one-dimensional projections is called computed tomography or CT. CT, using x-ray imaging, has been applied successfully to medical diagnostics for more than two decades. With 500 - 1000 projections, the accuracy of reconstructed images is good enough to show the essential details of human organs.

### 1.2.1 Radon transform and reconstruction algorithms

In Figure 1, we have a three-dimensional object imaged in parallel beam geometry. Let function *f(x,y)* represent the values of a cross section. The parallel projection of function *f(x,y)* at angle $\theta$ is given by (Kak & Roberts 1986, p. 656)

$$P_\theta(t) = \int_s f(t,s)ds\,, \tag{1}$$

where $t = x\cos\theta + y\sin\theta$ and $s = -x\sin\theta + y\cos\theta$. For continuous $\theta$, Equation (1) defines the *Radon transform* of *f(x,y)*.

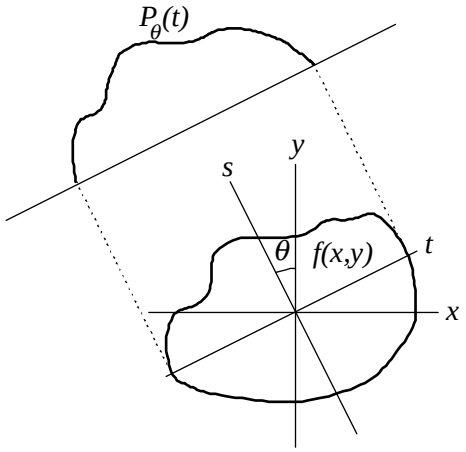


*Figure 1. Parallel-beam projection at angle θ (according to Rossi & Willsky 1984).*

The reconstruction of the cross-sectional image requires a numerical inverse of the Radon transform. This is done by superimposing all the projections onto the cross-section area. A trivial way of doing this is simply averaging the contributions of the projections onto the image area.

When the number of projections is limited, the backprojection alone is not enough. A simple example is shown in Figure 2. An object with two sharp details is imaged in three-view, parallel-beam geometry. Along with the original details, the backprojection yields undesirable effects. The black ellipses cast shadows along the projection lines, a phenomenon which is called *streaking*. Where strong streaks meet, a *ghost image* is formed. Besides, the original details are flattened because their mass is partly distributed along the projection lines.

There are two basic ways of overcoming the problems of disturbing reconstruction effects: iteration or finding an analytic solution. Sanz et al. (1988) present the principles of non-iterative analytic solutions. They start with the conventional definition of the inverse Radon transform,

$$f(x,y) = \int_0^\pi Q_\theta(x\cos\theta + y\sin\theta)d\theta\,. \qquad (2)$$

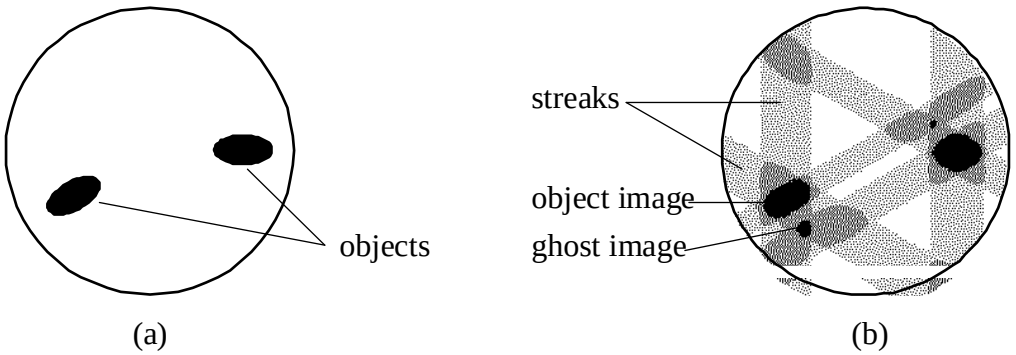


*Figure 2. The original cross section has two sharp object details (a). Backprojecting three projection images results in streaks and ghost images in addition to the correct details (b).*

In Equation (2), $Q_\theta(t)$ is obtained from projections $P_\theta(t)$ by filtering them with a high-pass filter. The discrete implementation of this inversion formula depends on the imaging geometry (parallel-beam, fan-beam equiangular, fan-beam equispaced).

If convolution in projection space is used to perform the filtering, the above reconstruction algorithm is referred to as the *convolution backprojection* technique. If filtering is performed in Fourier space, the algorithm is designated the *filtered backprojection* technique.

An example of an iterative reconstruction algorithm is the algebraic reconstruction technique, ART (Agi et al. 1992). First, the set of projections is written as one single-column vector

$$\mathbf{r} = \left[r_1, r_2, \ldots, r_q\right], \tag{3}$$

where $q$ is the total number of samples in all projections. Likewise, the image to be constructed is defined as a column vector

$$\mathbf{i} = \left[i_1, i_2, \ldots, i_t\right]^T, \tag{4}$$

where $t$ is the number of the image pixels. Then the Radon transform can be written as

$$\mathbf{r} = \mathbf{A}\mathbf{i} + \mathbf{e}, \tag{5}$$

where **A** is the projection matrix and **e** is the error vector. In each iteration round, the error between each measured and calculated ray-sum is normalised and added to the estimate of the image.

The interested reader can learn more about reconstruction algorithms from papers by Kak (1990) and Kak & Roberts (1986). Rossi & Willsky (1984) analyse the performance and robustness of reconstruction algorithms. The books by Herman (1980), Huang (1987), Sanz et al. (1988), and Krestel (1990) give a good survey of the fundamentals of CT.

### 1.2.2 The number of projections needed for reconstruction

There are some practical difficulties in applying the ideal mathematical solution to CT (Herman 1980, p. 38):

- Radon's formula determines a picture of all its line integrals. In CT we have only a finite set of measurements. Even if these were exactly the projections along a number of straight lines, a finite number of them would not alone be enough to determine the picture.
- The measurements in computed tomography can only be estimates of the line integrals. Inaccuracies are due to the width of the x-ray beam, scattering, beam hardening, detector inaccuracies, and mechanical instability of the measurement system.

When is a reconstructed cross-section acceptable? For example, two conditions might be set for successful reconstruction:

- The spatial resolution of the image is approximately the detector pitch $w_d$.
- The signal-to-noise ratio of the reconstructed image is about the same as in the projection images.

One way of getting an idea about the number of projections needed is to conclude like Pullan (1979) that if the cross section to be reconstructed contains $n$ rows and $n$ columns, we have $n^2$ unknowns to solve. Thus, $n^2$ independent simultaneous equations would be needed to calculate a unique solution to the problem. It will then be necessary to make at least $n$ individual transmission measurements from at least $n$ directions to reconstruct the cross section.

Herman (1980, p. 285) gives a measure for the necessary number of projections $M$. Expressing the image function in polar co-ordinates ($r$, $\alpha$), the image complexity is related to its frequency response about angle $\alpha$. If we choose the number of projections $M$ to be so large that the interesting object details are unlikely to have frequencies higher than $M/2\pi$, a satisfactory solution may be achievable. The higher frequencies must, of course, be filtered from the resulting image.

To apply Herman's criterion to our present problem, we can presume, for example, that most logs have maximally eight knots in one slice. Choosing a sampling frequency twice as high as the "knot frequency", we end up with 16 imaging projections. By doing this, we could find all the knots, but still could not see small details in them.

### 1.2.3 Restrictions set by the sawing process

In medical applications, some hundreds of projections are obtained with one x-ray source and one line detector. The source-detector combination is rotated step-by-step around the object, taking one image per step.

Unfortunately, the above set-up will not work with log imaging in a sawing process. The log moves at speeds of up to 2.5 m/s, and it cannot be stopped or rotated to get multiple projection images from one log slice; nor can the imaging hardware rotate around the log. The only way of obtaining several projections is to have a fixed source-detector pair for each direction. Economic reasons limit the number of projections to about three.

Obviously it is not possible to reconstruct log images from three projections, if we understand reconstruction in the traditional pixel-by-pixel sense. Instead, we shall locate the knots as a combination of greater volume elements. When doing this, we utilise *a priori* information about the geometry of the logs and the stem.

## 1.3 THE SCOPE OF THE RESEARCH

The present study was preceded by several phases of research, both at VTT and in other organisations. These projects included experimental work on applying x-rays for wood imaging, collecting knowledge of wood properties, and developing a new x-ray line camera. This previous research resulted in a set of preconditions for our study:

- X-rays are used for imaging.
- There are exactly three imaging projections at 120° intervals, with fixed source-detector hardware for each projection.
- Fan-beam imaging geometry is applied using a point source and a line detector.
- An image line consists of 256 pixels, each pixel being digitised with 16 bits.
- The nominal imaging speed is 500 lines per second, which corresponds to 2 to 5 lines per centimetre at log speeds of 1.0 - 2.5 m/s.

From these starting points, our aim was to develop a method for obtaining three-dimensional information on knots in logs. This information should be accurate enough to enable an essential improvement in log sorting. Additionally, the algorithms should be implementable with current processor technology to work at normal sawing speeds.

In this research, our interest was solely in the detection of knots. Attention was focused on developing a measuring instrument, and the questions involved with log sorting and process optimisation were not considered. We also left out the measurement of geometrical properties and the detection of cracks and rot, even though the same imaging technique is applicable.

Details of the line camera are not included because of trade secrets involved.

## 1.4 THE CONTRIBUTION OF THE THESIS

The contribution of the thesis is a method of detection of knots in logs using x-ray imaging and only three projections. The method is tested with both simulated and real log images. It is shown that the information obtained is valuable for effective log sorting before sawing. The method produces parameters such as the number of knots per metre, knot volume per metre, estimated knot co-ordinates, and amount of knotless sapwood.

All computation was carried out with a standard PC. The implementation of the real-time system is being carried out by another party according to the specification outlined in this study.

## 1.5 RELATED RESEARCH

### 1.5.1 Scanning logs with medical CT

Several research groups have applied medical CT systems for log scanning experiments. The results are promising. This is natural because a log and the human body are similar both in their dimensions and their x-ray characteristics. However, the low speed and the high cost of the present CT scanners make them impractical for real-time industrial inspection systems. These studies have been mainly demonstrations to gain justification (and financial support) for more practical research.

Funt and Bryant (1987) were probably among the first ones to try medical CT images in the detection of internal log defects. They developed an automatic method for interpretation of CT images to identify the knots, rot, and cracks occurring in a log. They met the same problem as others at that time: the scanning time was 3 minutes per slice!

Som et al. (1992) describe an automated feature extraction technique to detect and classify features such as knots, rots, and cracks from CT images of logs. The images were acquired using a hospital CT system, the GE9800, with a fan beam and a slice thickness of 2 mm. The slice data were used to reconstruct an image of 512-by-512 pixels.

According to Som, the major difficulties are the high moisture content, the high density variation within logs and the high mill throughput rates. Their experiments showed that knots were sometimes obscured by moisture. The density value of a pixel was not enough for the segmentation of the image, but also the statistical spread of the neighbourhood should be utilised.

Grundberg & Grönlund (1992) also used the GE9800 to scan test logs. They demonstrated the detectability of knots by reconstructing cross-sections with 512-by-512 spatial resolution using 4096 grey levels.

Both Wagner et al. (1989b) and Roder & Magnuson (1989) report their experiments of scanning logs with a medical CT scanner, the Imatron CT-100. The CT-100 is called a "fifth-generation" scanner because it uses a scanning electron beam instead of mechanical rotation of the x-ray imaging system. It generates a moving x-ray fan by scanning a highly focused electron beam along semicircular tungsten targets that partially surround the object to be scanned. In its ultrafast mode, the CT-100 acquires 34 images per second. As one might expect, the images were accurate, showing all the knots and even the annual rings. The scanning speed of the CT-100 for 256-by-256 images is 0.3 m/s. An array processor and backprojector hardware reconstructed the images in approximately 5 seconds.

Two papers by Zhu et al. (1991a, 1991b) describe a computer vision system aimed at locating, identifying, and quantifying the internal defects of logs by analysing their CT image data. The proposed inspection system is composed of three components: a CT scanner-based data acquisition system, a low-level module for image segmentation, and a high-level module for defect recognition. A heuristic, rule-based approach is used to perform

3-D object recognition. The performance of the method was demonstrated by experiments with CT images of red oak logs.

### 1.5.2 Experiments with a small number of projections

Sikanen (1989) has studied the properties of four selected reconstruction algorithms with very few projections. The performance of the algorithms was investigated using both simulated data and real measurements on wood samples. The results showed that non-iterative methods were not suitable due to strong streaking. The iterative algorithms (the multiplicative algebraic reconstruction technique MART and the maximum entropy method MENT) were able to detect 50 % of knots larger than 10 millimetres.

To improve the results, two methods were developed for obtaining difference images that contain only the absorption due to knots. The first method is a simple subtraction procedure that uses the projection data of a knotless slice as a reference. The other one estimates the density distribution within the stem from measurements of a knotless slice. The density distribution is presented as a series expansion. The second method is shown to yield better results and to improve the visibility of knots in the reconstructed difference images.

Sikanen concludes that - according to his experiments - approximately six projections are needed to detect 10-millimetre knots.

### 1.5.3 Unconventional imaging geometries

X-ray sources and detectors do not have to be in one plane. The only restriction is that the projections should be independent. Puumalainen (1993) describes a method called MOCT (moving object computer tomography). The imaging system uses two x-ray sources and six line detectors. Each source illuminates a group of three parallel line detectors that are placed successively across the moving direction of the log. Thus, six projections are achieved with only two sources. There are no reports on the performance of systems of this kind.

### 1.5.4 Optical scanning to find internal defects

Lee et al. (1991) have used a log profile image and a log surface image, both simultaneously captured by an optical scanner, to predict the internal properties of the log.

Grace (1992) reports a log sorting system based on information generated by the scanning frame. According to Grace, the surface smoothness is related to the knottiness of the log. The type of the log (butt, middle, top) can be guessed from the shape. The variables of log geometry, which are best related to board grade, were log type, butt-end taper and bumpiness. Using this information, a sorting system was constructed and later installed at a sawmill.

### 1.5.5 Detection systems for explosives

X-rays have been applied for a long time in the detection of weapons that could be used for hijacking. Nowadays the major threats are explosives. Passenger luggage cannot be effectively inspected for explosives using conventional one-view imaging, nor is there enough time for such computed tomography as in medical applications. So this problem has some similarities to our problem of finding defects in logs.

Bjorkholm & Wang (1992) describe a system called Z-Scan, which is based on two-view, dual-energy x-ray imaging. Because the attenuation of an element depends heavily on the radiation energy, materials can be classified much more effectively with two energies than with one. A three-dimensional mass model of the object is created using a modified multiplicative algebraic reconstruction technique (MART). To reduce ray artefacts and ghost images, a set of physical constraints is applied: (1) the reconstruction space is limited to the maximum possible dimension of the bag, (2) only physically reasonable densities are allowed, (3) the mass distribution of typical bag contents is used as a reference, and (4) the space frequency of the solution is limited. Z-Scan is claimed to be rather sensitive to explosives simulants with modest, visually resolvable false detections. The system is undergoing further sensitivity testing.

Eilbert & Krug (1992) report on their work on a one-view, dual-energy x-ray system for the detection of explosives in baggage contents. Each object in an item of baggage is examined for a match to a specific effective atomic number, density, and mass threshold. Material properties are determined by comparing the relative attenuations of the 75 kV and 150 kV beams, and electronically separating the object from its local background. The detection expert system incorporates composition analysis, and many additional heuristic factors such as the object's shape, density, and mass, as well as suspicious configurations and devices such as sheet explosives, detonators, and electronics.

Even the most advanced luggage inspection systems are only semiautomatic: a human operator has to check the images of each suspicious case before a security alarm.

### 1.5.6 Nuclear emission imaging

The next application is quite different from ours, but the basic problem is the same: how to reconstruct objects from a limited number of projections.

Lévai et al. (1990) have made feasibility studies for tomographic reconstruction of a cross-sectional activity distribution of a nuclear fuel assembly. The purpose was to determine the number of fuel pins and localise the positions where pins were missing.

Gamma radiation from an irradiated 8-by-8 fuel assembly was measured from different angles and positions. The measured data set was used as projections for reconstructing the activity profile of the assembly in a cross-sectional plane. The following *a priori* rules were utilised in the reconstruction: (1) pixel values must lie within specified ranges, (2) the image vanishes outside a region, (3) the image to be reconstructed deviates at most

by a known percentage from a similar reference image, (4) it is sufficient to make a binary decision (the pin present or absent), though the actual activity distribution function is not binary.

Lévai concludes that for reliable detection a minimum of 12 to 16 views is needed.

### 1.5.7 Convex hulls in limited-projection CT

Making use of *convex hulls* is one way of improving the reconstruction from limited-projection measurements. The convex hull of an object is the smallest convex region containing the object. It is discovered from the projections by determining the s*upport lines*, which are tangential lines bounding the object.

Tam (1987) presents an algorithm to determine an estimate of the exterior boundary of the object. This boundary as well as the upper and lower limits of the density are used as *a priori* information of the object. The actual reconstruction is an iterative process where the image is transformed back and forth between the object space, with corrections made by the *a priori* information.

Tam also uses his algorithm for detecting flaws embedded in known objects. The idea is to eliminate the contribution of the known medium, and reconstruct the difference image.

Prince & Willsky (1990) propose algorithms for reconstructing convex sets from noisy support line measurements. The measurement noise may make the set of measured lines inconsistent, i.e. there may be no convex set that has all the measured lines as support lines. Prince & Willsky show how knowledge of geometric constraints, the object's shape and position, and measurement noise models may lead to optimisation-based or probabilistic-based algorithms.

The above ideas have been tried in log scanning. The patent application by Aune & So (1989) brings up a log scanning system that uses three-view x-ray imaging. The image of the knot-free stem is first computed by filtering, and then its contribution is subtracted. Finally, the support lines of the defects are located from the difference image. To overcome the problems arising from multiple overlapped defects, several thresholds are used in this edge-looking process.

Methods based on convex hulls are highly suitable for establishing boundaries of a solid object or a single defect on a known background. On the other hand, they are not very useful when a detailed image of a more complicated object has to be reconstructed. As seen later in chapter 2, we have some special problems when detecting knots in logs. These include fading of knots and inconsistency of projections, both caused by attenuation of humidity. A knot may not appear as a unique convex object in the x-ray images because of this disturbance.

### 1.5.8 Gamma ray scanners

Grönlund (1992) presents TINA, a gamma ray scanner that has been used in Swedish sawmills for more than 10 years. It measures the under-

bark diameter and density variations along the log. Hagman (1992) describes a quality model based on the data collected by TINA. The model is a linear combination of density properties and external shape properties of the log. The external shape parameters involved are the taper in the butt half of the log and the surface unevenness. Hagman claims that their system has a better prediction capability than manual grading. For a two-class system (high quality, low quality), the precision of prediction was 75 % with equal group sizes.

Taylor et al. (1984) used an industrial tomography system with an Ir192 photon source to detect defects in a small number of test logs. With 100 projections, the detection capability was satisfactory, but the imaging time per slice was as long as one second.

### 1.5.9 Summary

The success of medical CT has encouraged researchers to try the same technology in industrial processes to detect internal defects in products. Log sawing is one process that could make great use of such a detection instrument. Most of the research within this field concentrates on off-line experiments with medical CT. However, because of certain technical difficulties, no on-line CT systems for log inspection have been developed yet. The biggest problem is the imaging speed: there is not enough time to obtain a sufficient number of projections to reconstruct cross-sections accurately. The imaging speed is limited by the x-ray technology, and no major breakthrough is expected in this area. After recognising that true CT is not possible in this application, the question is put in another way: how can one gain useful information from incomplete imaging data?

One possibility is to determine the size and shape of the log with optical, gamma ray, or x-ray detection. With gamma rays and x-rays also density can be measured. Logs may then be sorted using quality indices calculated from the above-mentioned properties. Size, shape, and density indicate if the log is from the top, middle, or butt part of the stem. This information helps indirectly in the prediction of knot characteristics.

Another approach is to look for approximate reconstruction using known properties of the object. The problem is much easier if there are only a few interesting details in the object, and their shape can be described with simple models. Obviously, this principle is a potential way of detecting knots in logs.

# 2 X-RAY IMAGING OF WOOD

## 2.1 INTERACTION OF X-RAYS WITH MATERIAL

When x-rays penetrate material, the radiation complies with the *law of attenuation* (Krestel 1990, p. 71),

$$N = N_0 e^{-\mu x}, \tag{6}$$

where $N$ = number of quanta penetrating the material,
$N_0$ = number of incident quanta,
$\mu$ = linear attenuation coefficient, and
$x$ = thickness of material.

Defining the intensity of radiation as a number of quanta through a unit area per unit time, we can rewrite Equation (6) in form

$$J = J_0 e^{-\mu x}, \tag{7}$$

where $J$ = intensity of radiation penetrating the material, and
$J_0$ = intensity of incident radiation.

The decrease in the number of quanta passing through material can be explained by three effects: the photoelectric effect, scattering and pair production (Krestel 1990, pp. 71 - 72).

In the case of the photoelectric effect, an x-ray quantum hits an electron of the inner atomic shell and transfers all its energy to this electron. If the energy transferred is greater than the binding energy of the electron, the electron is removed from its atom.

The x-ray quantum can interact with an atom without its energy being absorbed. It then leaves the atom in a changed direction. If it retains all its energy, this is called *coherent scattering* or *Rayleigh scattering*. If it loses a part of its energy, the effect is called *incoherent scattering* or *Compton scattering*.

Electron-positron pair production does not occur in the low-energy x-ray imaging systems that we are considering here.

The attenuation law of Equation (6) holds only for a very limited case when

- the radiation is monochromatic, and
- the thickness $x$ of the object is infinitesimally small, and
- the material is homogeneous.

Generally, none of these conditions is true, and the attenuation law must be adjusted.

## The case of non-monochromatic radiation

The radiation being monochromatic means that the energy of all the incident quanta is the same. In reality, x-ray tubes generate beams with a spectrum of energies; the radiation is polychromatic. For example, if we use an x-ray tube voltage 100 kV, the half-power points of the output radiation are typically 30 keV and 70 keV. Because the linear attenuation coefficient $\mu$ is a function of energy, we should integrate over the radiation spectrum:

$$J = \int J_0(E) \cdot e^{-\mu(E)x} dE \,. \tag{8}$$

We can measure the spectrum of the incident radiation, but there is still one more problem called *beam hardening*. The attenuation is generally greater for photons of lower energy, and thus the energy spectrum of the x-ray beam changes (hardens) as it passes through the object. This means that $\mu$ also depends on the position along the measurement beam, leading to

$$J = \int J_0(E) \cdot e^{-\int \mu(x,E)dx} dE \,. \tag{9}$$

## The effect of multiple scattering

When the object is not infinitesimally thin, an x-ray quantum may have multiple interactions with atoms. As stated by Wells et al. (1991), these events have practical significance when $\mu x > 1$. After multiple scattering, a fraction $b$ of primary scattered radiation will arrive at the detector. This reduces the calculated linear attenuation coefficient. Analysis by Wells gives us a revised model of attenuation:

$$J = J_0 e^{-\mu x} \cdot (1 + b\mu x) \,. \tag{10}$$

Wells extends this to higher order scattering as follows:

$$J = J_0 e^{-\mu x} \cdot \left(1 + \frac{e^{ab\mu x/(1+ab)} - 1}{a}\right). \tag{11}$$

Another parameter $a$ is introduced as a corrector for higher order scattering. Note that Equation (11) approaches Equation (10) when $a$ approaches 0.

The values of parameters $a$ and $b$ depend on the effectiveness of the *collimators* in the imaging system. Collimators are metallic screening structures to reduce unwanted scattered radiation that reaches the detector.

**The effect of density**

The linear attenuation coefficient $\mu$ includes the effect of the density of the interacting material. We introduce the *mass absorption coefficient* $(\mu/\rho)_m$, which is independent of the density $\rho_m$. The relationship between these coefficients is

$$\mu = (\mu/\rho)_m \cdot \rho_m . \tag{12}$$

The mass attenuation coefficients of primary elements in a material can be used to predict the $(\mu/\rho)_m$ of a material. This is done by summing the attenuation values $(\mu/\rho)_i$ of the elemental constituents, weighted according to their elemental fractions $f_i$,

$$(\mu/\rho)_m = \sum_i (\mu/\rho)_i \cdot f_i . \tag{13}$$

Equations (12) and (13) derive to

$$\mu = \rho_m \cdot \sum_i (\mu/\rho)_i \cdot f_i . \tag{14}$$

For a given measurement system, it is not very easy to control all the above variables analytically. Very often one has to rely on an empirical model of attenuation, which lumps together all the effects of the source spectrum, collimation, detector sensitivity, and the object properties. One way of doing this is to determine experimentally a so-called *build-up* coefficient $B$, which is a function of energy $E$ and the thickness $x$ of the object:

$$J = B(E,x) \cdot J_0 e^{-\mu x} . \tag{15}$$

If any essential change occurs in the imaging conditions, there may be a need for recalibration.

## 2.2 X-RAY CHARACTERISTICS OF WOOD

According to Wirkola (1983, p. 1522), a typical chemical composition of absolutely dry wood is: carbon 50.4 %, oxygen 42.5 %, hydrogen 6.2 %, and nitrogen 0.5 %.

Viitaniemi (1990) gives approximate dry-densities of pine: 500 kg/m$^3$ for stem wood, and 950 kg/m$^3$ for knots. According to the same report, the average moisture percentages of pine are: knot in sapwood 21 %, knot in heartwood 18 %, sapwood 88 %, and heartwood 20 %. Note that the moisture percentage (*m.p.*) is expressed here as moisture mass per dry-wood mass:

$$m.p. = \frac{m_f - m_d}{m_d} \cdot 100 \tag{16}$$

This definition comes from the way that the moisture content is usually measured: a piece of wood is first weighed fresh ($m_f$) and then again after drying ($m_d$).

The humidity of knots and heartwood is fairly low and stable. On the other hand, sapwood is the vital part of the tree, and therefore contains much water. Its moisture contents also vary considerably. Data collected by Kärkkäinen (1985) indicate that the variation range is from 80 % to 180 %.

From the above figures, we can estimate densities and chemical compositions of knots and wood, these are shown in Table 1. When calculating densities, a volume expansion of 13,5 % is allowed, as reported by Viitaniemi (1990).

Each element has its own mass attenuation coefficient as indicated in Table 2. Combining data from Tables 1 and 2, we can calculate linear attenuation coefficients for knots, heartwood, and sapwood. The results are presented in Table 3.

*Table 1. Estimated densities and chemical compositions of knots and wood.*

| Type of wood | Density / kg / m$^3$ | Percentage of chemical elements | | | |
|---|---|---|---|---|---|
| | | C | O | H | N |
| Sapwood, 80% moisture | 790 | 28.0 | 63.2 | 8.3 | 0.3 |
| Sapwood, 180% moisture | 1230 | 18.0 | 72.4 | 9.3 | 0.2 |
| Heartwood | 530 | 42.0 | 50.3 | 7.0 | 0.4 |
| Knot in sapwood | 1010 | 41.7 | 50.6 | 7.0 | 0.4 |
| Knot in heartwood | 990 | 42.7 | 49.6 | 6.9 | 0.4 |

*Table 2. Mass attenuation coefficients of carbon, oxygen, hydrogen, and nitrogen according to Compton & Allison (1960).*

| Energy / keV | Mass attenuation coefficient / ($\mu/\rho$) / (m$^2$/kg) | | | |
|---|---|---|---|---|
| | C | O | H | N |
| 50 | 0.0188 | 0.0214 | 0.0375 | 0.0199 |
| 60 | 0.0176 | 0.0191 | 0.0375 | 0.0182 |
| 70 | 0.0167 | 0.0178 | 0.0360 | 0.0172 |
| 80 | 0.0161 | 0.0168 | 0.0344 | 0.0164 |
| 90 | 0.0156 | 0.0161 | 0.0327 | 0.0158 |
| 100 | 0.0151 | 0.0155 | 0.0313 | 0.0153 |

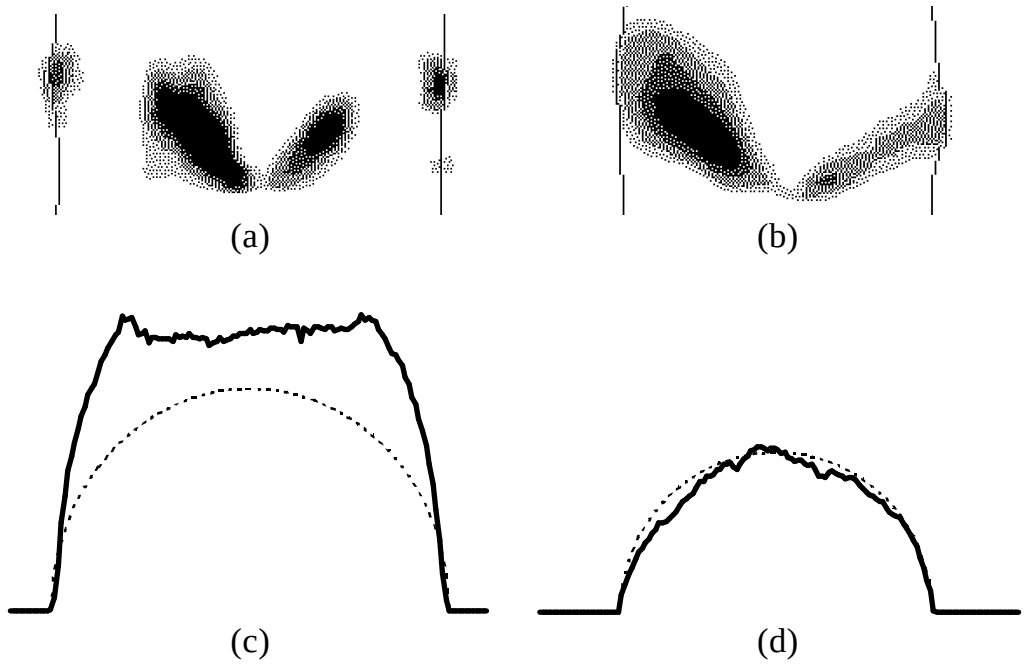


*Figure 3. (a) High moisture contents of sapwood weaken the visibility of knots in an x-ray image. For comparison, (b) shows an image of a dry log. The corresponding curves (c) and (d) characterise the cross-sectional densities of the logs. Dotted lines represent cross-sections of ideal homogeneous objects.*

*Table 3. Estimated linear attenuation coefficients of knots and wood.*

| Type of wood | Radiation energy / keV | | | | | |
|---|---|---|---|---|---|---|
| | 50 | 60 | 70 | 80 | 90 | 100 |
| Sapwood, 80% moisture | 39.6 | 38.2 | 36.3 | 34.6 | 33.0 | 31.7 |
| Sapwood, 180% moisture | 66.1 | 63.8 | 60.7 | 57.8 | 55.2 | 52.9 |
| Heartwood | 23.8 | 23.0 | 21.9 | 20.9 | 19.9 | 19.1 |
| Knot in sapwood | 45.6 | 43.9 | 41.8 | 39.9 | 38.1 | 36.6 |
| Knot in heartwood | 44.3 | 42.6 | 40.6 | 38.7 | 37.0 | 35.5 |

The contributions of hydrogen and nitrogen to the x-ray attenuation of wood appear to be negligible, and the attenuation of x-rays in wood is dictated by carbon and oxygen. Because the atomic weights of these elements are closely similar, their coefficients are nearly the same at energies used. This leads to the unfortunate fact that high moisture content of sapwood may cause considerable difficulties in the detection of knots.

Som et al. (1992), for example, state that the knots are sometimes obscured by moisture and no obvious image segmentation is available through simple histogram processing. If the humidity of the sapwood is high, the density of the normal sapwood may be nearly the same as with the knot or even higher. This finding is supported by Taylor et al. (1984).

Figure 3 demonstrates the fading effect caused by moisture. X-ray images of a fresh log and a dry log are shown. In both cases the projections have been selected so that the knot shades should continue from the middle to the border of the image. In the fresh log, however, the knots seem to dis-

appear in the sapwood region. They reappear near the surface, where the outcoming branch deforms the stem. Obviously, the fading effect should be kept in mind when developing a method for knot detection.

## 2.3 EQUIPMENT FOR X-RAY IMAGING

### 2.3.1 X-ray sources and detectors

An x-ray source consists of a high-voltage generator and an x-ray tube. According to the literature, all experimental log scanning systems use a voltage of less than 150 kV. This choice is based on medical applications research seeking the best matches for the radiation energy and the object density. Since the tube current may be 10 mA or more, the total power consumption of the tube is more than 1 kW, and water cooling is necessary.

The most advanced generators use primary regulation by means of power level compensation and microprocessor control to achieve a good long term stability. The deviation of the output power is stated to be less than 1 %.

For fast imaging, the short-term characteristics are even more important. The output ripple must not exceed digitising resolution. In practice this is realised with frequency inverters, a typical switching frequency being 500 kHz.

To date, three types of detector systems have been used in CT systems (Krestel 1990, p. 437):

- scintillation crystals with photomultipliers,
- scintillation crystals with photosensitive semiconductors, and
- xenon gas ionisation chambers.

The crystal-semiconductor combination is the most popular type of detector in the newest systems, probably because of its high packing density. Scintillation crystals convert x-rays into visible light, which is then measured with a photodiode and proper amplification electronics. Typical scintillation materials are NaI, CsI, and $Bi_4Ge_3O_{12}$.

### 2.3.2 Imaging geometry

The first x-ray scanning systems had only one source and one detector. The source-detector pair was first moved in a translational manner, producing a *parallel-beam* image at one projection angle (see Figure 4). Then the source-detector combination was rotated by an angle increment, and the next projection was measured. This is apparently a slow way of scanning.

The *fan-beam* imaging system has a combination of one x-ray tube and a line detector with multiple elements. There are several implementation principles of this geometry. The source and detector may rotate together around the object, or only the source rotates while the detector is a fixed ring. In fifth-generation imaging systems, there is no mechanical ro-

tation at all (Roder & Magnuson 1989). The electron beam is deflected by coils before it hits an arc-shaped anode located around the imaging area. Thus the direction of the x-ray beam can be controlled electronically, making the scanning much faster than in conventional systems.

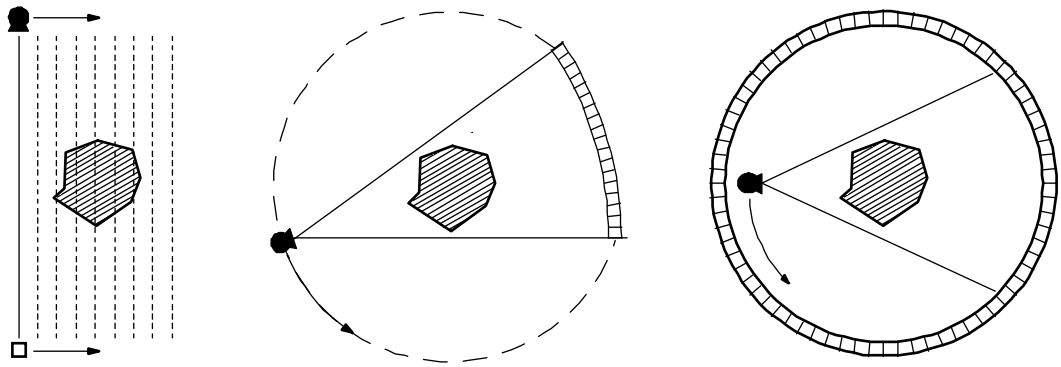


*Figure 4. Imaging geometries: (a) parallel beam, (b) rotating fan beam, and (c) fan beam with a fixed detector ring.*

We want to measure the straight beam coming from the x-ray tube to a detector cell. Because of scattering, a part of the radiation zigzags through the object and does not truly represent the points in the ideal line-of-sight path. To reduce the scattered radiation, a *collimator* is installed in front of the detector. The simplest collimator is a narrow slot in a plate of strongly attenuating metal such as lead. This kind of structure obstructs radiation coming from outside the imaging plane. A lamellar structure with a hole for each detector element also reduces scattered beams in the imaging plane.

The speed requirement in our system dictates that fixed fan-beam geometry must be used. This means that each projection has its own x-ray tube and line detector.

# 3 SECTOR-ORIENTED RECONSTRUCTION

## 3.1 SEARCH FOR THE METHOD

The message from the previous chapters is clear: a pixel-by-pixel reconstruction - in the sense of conventional tomography - is a hopeless task from a small number of projections. However, the literature cited and our own preliminary tests imply that useful information can be gained even from three projection images. According to the opinions of some sawmilling professionals, even such parameters as knot volume per unit length and thickness of knot-free sapwood would greatly help in log sorting. It is also known that the value of the log is significantly correlated to the part of the stem it is cut from (Hagman 1992). Even more valuable, and possibly still obtainable, would be knowledge about approximate knot areas on given surfaces of sawn timber.

The project was begun by testing a few hypotheses with experimental data. The data were acquired with an imaging set-up consisting of an x-ray source, a line detector, and a mechanism to move pieces of logs through the system. The images went through pre-processing, which included gain and offset correction of individual pixel values, logarithmic transformation, and adjustment of the mutual positioning of the projections. Finally, the background was filtered out from the images to show only the variations due to knots. These difference images were used in testing the hypotheses described below.

### 3.1.1 The hypotheses tested

*Hypothesis 1: Knot directions in 3-D space can be determined from knot vectors in the projection images.*

The idea of Hypothesis 1 comes easily into mind when looking at images such as in Figure 5. Indeed, if the endpoints of a line are known at least from two views, the line can be located in 3-D space. The essential problem seems then to be how to find the endpoints. The projection images have to be filtered, segmented, and examined for knot-like objects. When a knot shape is found, its orientation must be determined in order to look for the endpoints from the proper directions. Surprisingly enough, the endpoints do not generally lie on the border line of the knot shadow, but rather within it. This finding can be shown with elementary geometry.

When trying to formulate a robust algorithm for the calculation of knot directions, we faced considerable difficulties. First of all, the accuracy of endpoint detection was inadequate. Even though the shadow of the knot is located correctly, it is not self-evident where exactly the endpoints lie. Unfortunately, the result of the calculation is sensitive to endpoint inaccuracy.

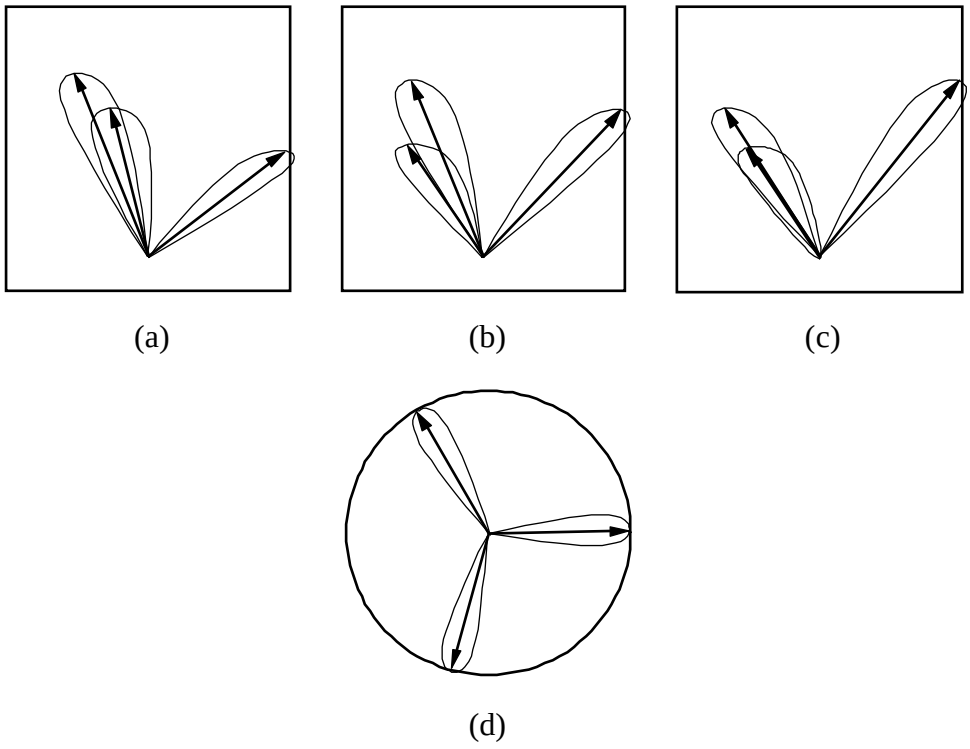


*Figure 5. Knot vectors found in three projection images (a - c) are used to calculate the directions of knots. (d) shows the result as a cross-sectional view.*

Furthermore, some of the endpoints are shadowed by other knots. Aune & So (1989) claim that overlapping knots can be distinguished with multiple thresholding. We witnessed no evidence of this in our tests. It follows from the shadowing that there may be a different number of endpoints found in the projection images. When we add to this the inaccuracy of the endpoints, it is understandable that consistency between projections is often hard to find.

The above aspects decreased the attraction of the principle in Hypothesis 1, and so this idea was rejected already at an early phase of the project.

*Hypothesis 2: Convex hulls can be utilised to reconstruct simple objects such as knots.*

The principle of convex hulls is suggested for example by Tam (1987), Prince & Willsky (1990), and Aune & So (1989). The idea is to approximate a convex object with a polygon, which is bordered by the *support lines* of the object. In a given view direction, the support lines are the two straight tangential lines of the object to that direction (see Figure 6). The convex hulls are determined separately for successive cross-sections, and the results are then combined to obtain a 3-D reconstruction of the object.

In our case, the aim would be to find a set of convex hulls, each containing one single knot. Figure 6 shows an example with two cross-sections reconstructed. The result seems quite satisfactory, but still there are indica-

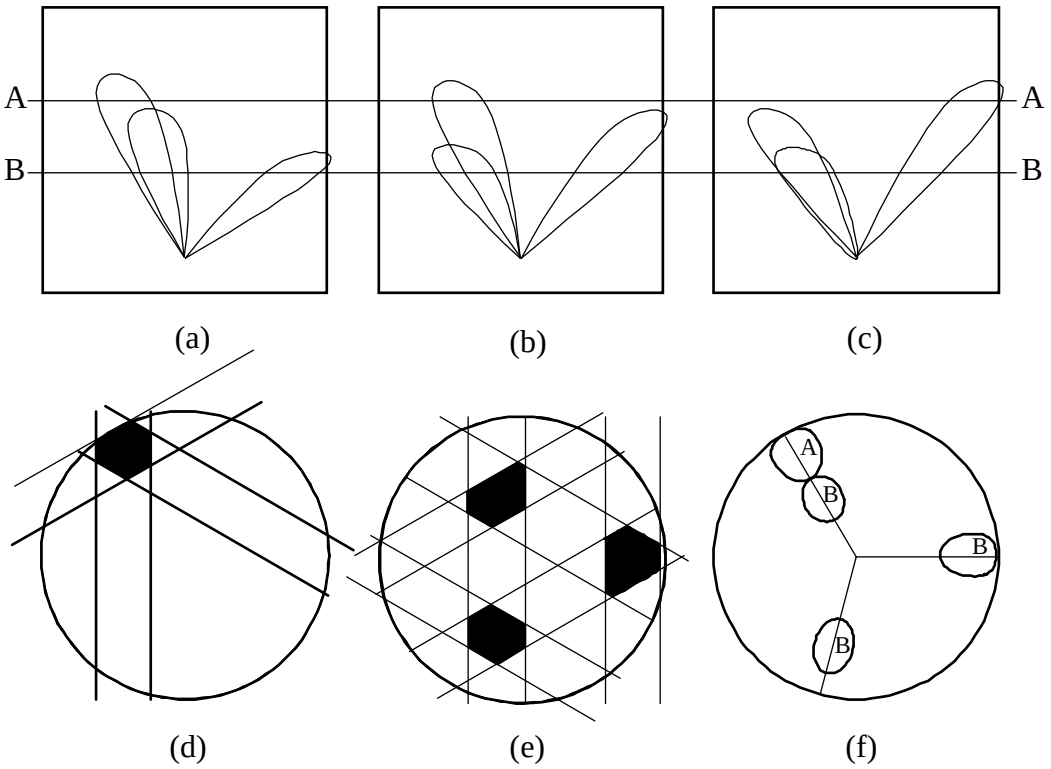


*Figure 6. Convex hull principle: support lines from three projection views border convex hulls that contain the knots. Cross-section A is shown in (d) and cross-section B in (e). The original objects at both cross-sections are presented in (f).*

tions of potential problems even in this simple case. The object areas in Figure 6.e are wider than they should be. This is obviously because two partially overlapping knots appear as one object in the projection images, thus generating only one pair of support lines instead of two pairs. When the number of knots increases, the knot segments in the reconstruction images tend to combine, which makes the results worthless. Multiple thresholding may help to distinguish overlapping knots (Aune & So 1989), but it is not a generally applicable solution according to our experiments.

Another harmful phenomenon is the splitting of knot images. As explained in Chapter 2, the moisture in sapwood often causes fading, and therefore some knots do not appear as continuous regions in the projection images. This results in inconsistent support lines from the projections.

Because of the above mentioned factors, Hypothesis 2 was also discarded.

*Hypothesis 3: Cross-section images of reasonable quality can be achieved with backprojecting, if enhanced with angular filtering.*

We learned in Chapter 1 that using a small number of projections will create streaks and ghost images in reconstruction. Hypothesis 3 is based on the fact that knots grow from the heart of the stem towards the surface. Figure 7 illustrates what is meant by *angular filtering*. Suppose that the cross-section generated by backprojecting is expressed in polar co-ordinates as

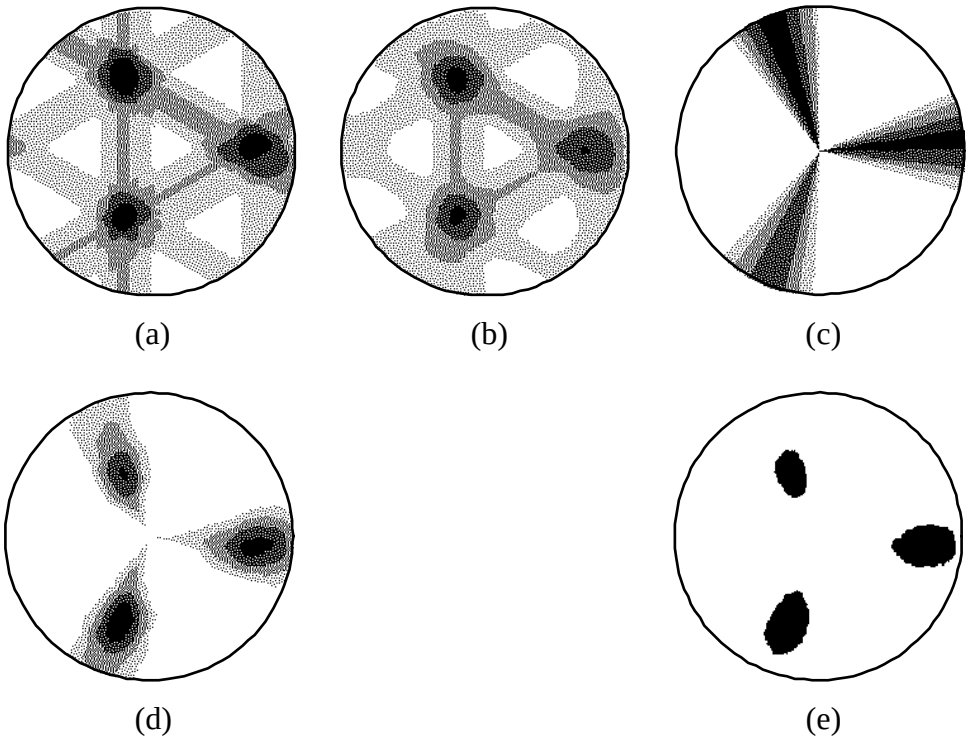


*Figure 7. Enhancing the reconstructed image with angular filtering: (a) cross-section backprojected from three projections, (b) cross-section after filtering in regard to polar angle ω, (c) image density averaged as function of angle ω, (d) weighted sum of (b) and (c), (e) the final image after thresholding.*

$f(\omega, r)$. The image is low-pass filtered in regard to $\omega$ producing the image in Figure 7b. In addition to that, an average is calculated from the image as a function of $\omega$. The result of averaging is visualised by Figure 7c showing the directions in which the knot patterns are concentrated. Streaks in 7b can now be attenuated by using 7c as a mask or a weighting function. The image in Figure 7d is obtained as a weighted sum of 7b and 7c. Thresholding yields the final reconstruction in Figure 7e.

The procedure of angular filtering is expected to reject shapes that do not fit in with the characteristics of natural knot patterns. Preliminary tests with measured and simulated data were so promising that the efforts were directed to developing this principle further.

### 3.1.2 Guidelines for developing the method

The essential objective in developing the knot detection method was to find algorithms that could be run in reasonable hardware in real time. In this case "reasonable hardware" was defined as commercially available multi-processor units that would work under the control of a standard PC computer. The task to be implemented included computation of about 500 cross-sections per second, the size of a cross-section being typically 256 by 256 pixels. Each image had to be filtered and segmented, and then the

successive cross-sections should be combined to find 3-D knot shapes. This was considered computationally far too heavy for the suggested equipment.

Conventional CT in fact sums all projections onto the cross-section to be reconstructed. When we are trying to do the reconstruction from only three projections without iteration, summing is not effective. Suppose that two projections contribute strongly to a certain area in the cross-section, but the corresponding part of the third projection is empty. Summing would yield a non-zero value for that area, even though the method should clear it according to information from the third projection. In other words, the reconstruction method should be *exclusive*.

Starting from these prerequisites, we stated our strategy as follows:

- Rather than trying to reconstruct log slices pixel-by-pixel, we look for three-dimensional shapes that have a direct relationship to the geometry of knots in wood. The cylindrical co-ordinate system is used to present the object.
- Data is compressed as fast as possible to reduce computation and keep the memory requirements reasonable. A log image represents several megabytes of data that must be processed in seconds. Thus, a non-iterative method with the pixel-by-pixel processing minimised would be desirable.
- *A priori* knowledge of knots and stems is utilised. The knowledge is associated with the geometry, density, and moisture contents in different parts of the log.
- The locating of knots is based on uncertain, incomplete data. A principle called *fuzzy reasoning* is applied to combine measured data and a priori knowledge.
- The reliability of the detection result is estimated.

The above principles have led us to a method that we call the *sector-oriented reconstruction technique*, SORT.

### 3.1.3 Overview of SORT

Figure 8 presents the computing phases and data flow in the SORT method. The first four phases are similar for all three projections P0, P1, and P2, and can be implemented totally in parallel.

Imaging is followed by pre-processing that includes normalisation of individual pixel values and adjustment of the mutual positioning of the projections. Background elimination is a two-part process: an image of the knotless stem is first determined by low-pass filtering; then the share of the stem is subtracted from the original image to show only the variations due to knots.

Backprojection in CT means superimposing all projections on to a cross-section. Our procedure differs from that in two ways. First, the intermediate results of each projection are saved separately for further processing. Second, the contribution of the projection is not directed to pixels, but rather to elements of sector-shaped areas. The purpose of this practice is to

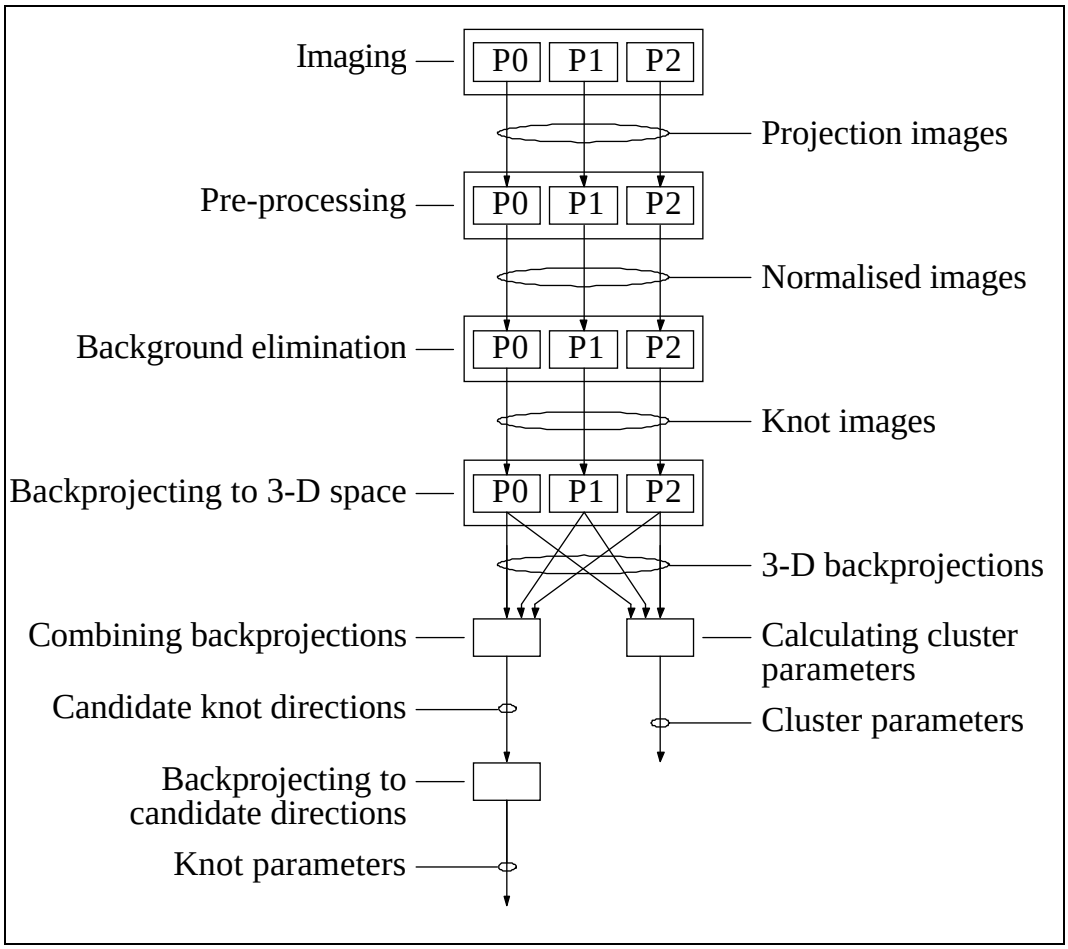


*Figure 8. Flowchart of the sector-oriented reconstruction technique, SORT. P0, P1, and P2 refer to the three imaging projections.*

decrease the amount of computation in filtering and segmentation, as described later.

The process divides into two branches after backprojection. The branch on the right computes collective parameters of the whole knot cluster, such as bounding dimensions and the total knot volume of the cluster.

The left branch handles individual knots, and its input data are the three backprojections consisting of density-related values. These values involve uncertainty that must be handled statistically. To do this, they are transformed to probabilities, or *evidences*. Combining the backprojections is then carried out as a process called *fuzzy reasoning*, where evidence of elementary image segments yield probabilities for candidate knot directions. Finally, the original projections are backprojected to the knot directions selected, and the resulting patterns are analysed to obtain the co-ordinates and volume of each knot.

## 3.2 FUNDAMENTALS

### 3.2.1 Co-ordinate system

The cylindrical co-ordinate system is a natural choice for describing logs and the knots in them. A short piece of a stem is approximately a cylinder with its pith on the longitudinal axis. The knots start from the pith and grow radially towards the surface of the log. Each knot is contained in a sector, which does not include any other knot.

The cylindrical co-ordinate system is defined by the rotational angle $\alpha$, the radius $r$, and the longitude $z$. We quantise the co-ordinates to obtain discrete *volume elements* $(i, j, k)$ in the cylinder space:

$$\begin{aligned} &\textit{sector } i\text{:} && (i - 0.5)\cdot\Delta\alpha \le \alpha < (i + 0.5)\cdot\Delta\alpha\ , \\ &\textit{ring } j\text{:} && (j - 1)\cdot\Delta r \le r < j\cdot\Delta r\ , \\ &\textit{slice } k\text{:} && (k - 1)\cdot\Delta z \le z < k\cdot\Delta z\ . \end{aligned} \qquad (17)$$

If the slice number is not relevant, we refer to *sector elements* $(i, j)$. The quantising steps selected are $\Delta\alpha = \pi / 18 = 10$ degrees, $\Delta r = 2$ centimetres, and $\Delta z = 1$ centimetre. The selection is a compromise between computational load and spatial resolution. The angle step is such that about all the knots reside in 1 to 4 sectors. The number of volume elements associated with a typical knot is in order of one hundred. Improving the spatial resolution would increase the computation almost linearly, but it would not automatically improve the accuracy in the same proportion. When the details become smaller, the uncertainty about their reconstruction increases.

The log is analysed in parts that contain one knot cluster each. The knot cluster under examination is placed at the origin of the co-ordinate system. To adjust the co-ordinates correctly, the central line of the log and the starting point of the knot cluster are first determined.

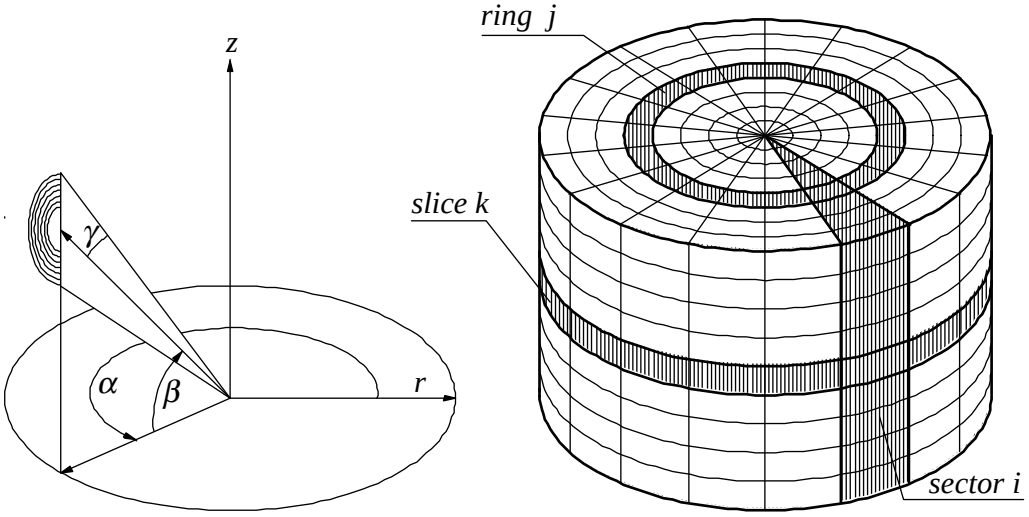


*Figure 9. On the left: the cylindrical co-ordinates are $\alpha$, r, and z. Angles $\beta$ and $\gamma$ are measures of steepness and width of the knot. On the right: the co-ordinates are quantised to rings, slices, and sectors.*

If $R$ and $L$ denote the radius and the length of the part of the log to be analysed, the maximum values of indices $i$, $j$, and $k$ are then

$$\begin{aligned} i_{max} &= 2\pi / \Delta\alpha - 1 \ , \\ j_{max} &= R / \Delta r \ , \\ k_{max} &= L / \Delta z \ . \end{aligned} \tag{18}$$

Additional variables used to describe knot characteristics are the rise angle $\beta$ and the opening angle $\gamma$. $\beta$ is the angle that the axis of a knot makes with the origin plane $z = 0$. As the knot is modelled as a cut cone, $\gamma$ is the average opening angle of that cone (see Figure 9). The positive direction of $z$ is towards the top end of the log, and thus the values of $\beta$ are normally positive.

### 3.2.2 Imaging geometry

The x-ray tube is considered here as a point source. The imaging geometry is defined by source-to-log-axis distance $d_1$, and source-to-detector distance $d_2$. Figure 10a shows a scheme of the geometry for one projection. The distance $d_2$ is a fixed property of the equipment, while $d_1$ varies with the shape and diameter of the log and with its position on the conveyor.

To interpret the images correctly, distance $d_1$ must be determined separately for all projections. To do that, the central lines from the x-ray sources to the middle of the log are calculated from the edge points of the projection images. The central lines are drawn in Figure 10b with dotted lines. Parameter $d_1$ is the distance from a source to the intersection of those lines. The SORT method also requires that the images are shifted to make the middle of the log coincide with the $z$ axis.

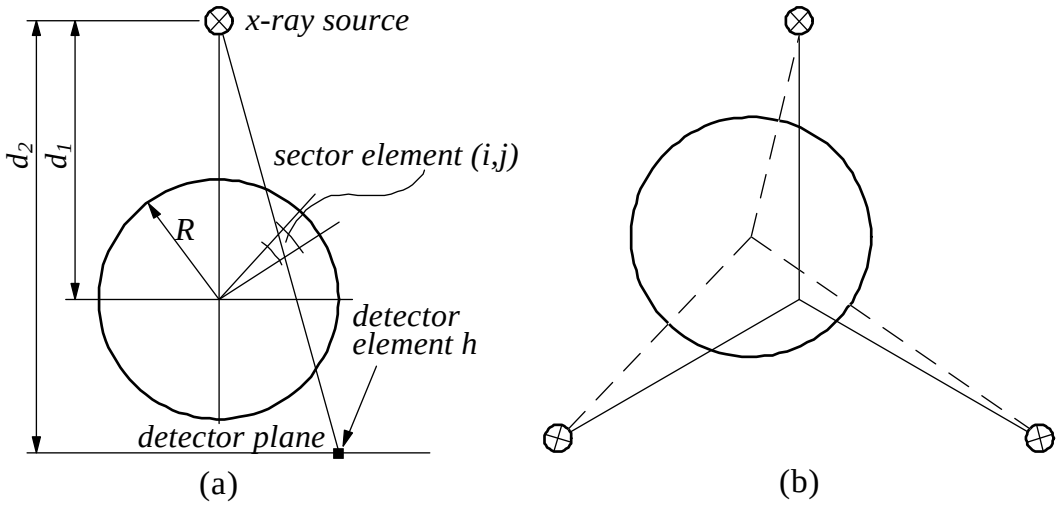


*Figure 10. (a) The concepts and parameters associated with the imaging geometry. (b) The origin of the imaging geometry is where the continuous lines meet. The dotted lines show the directions from the x-ray sources to the middle of the log.*

The detector elements are indexed by $h$. On some occasions, the ray from the source to the element $h$ is called *ray h*.

The detector consists of those elements whose width is $w_d$. The detector element width projected onto the origin plane is

$$w_{d0} = \frac{d_1}{d_2} \cdot w_d \,. \tag{19}$$

Parameter $w_d$ is used to scale log dimensions from pixels to centimetres.

### 3.2.3 Backprojecting coefficients

The imaging system produces three 2-D images $p_m(h, k)$ of the object, with $m$ = 0, 1, and 2. To compute the contribution of a projection pixel $p_m(h, k)$ to a volume element $(i, j, k)$, a set of coefficients $c(h, i, j)$ is used. The coefficient $c(h, i, j)$ equals the length of the ray $h$ within the sector element $(i, j)$ expressed in centimetres.

The coefficients $c(h, i, j)$ are applicable for all three projections with proper phase shifts of index $i$. Bearing in mind the conventions in Chapter 3.2.1, the shifted indices of projections 1 and 2 are $i_1 = (i - 12) \bmod 36$ and $i_2 = (i + 12) \bmod 36$, respectively.

Most of the coefficients $c(h, i, j)$ are zero. For a given $i$ and $j$, the coefficients are non-zero if and only if $h$ lies within a certain interval $[h_{min}, h_{max}]$. This is most fortunate; a great deal of computing time is saved by tabulating these limits for later use:

$$h_{\min}(i, j) = \left\{ \min(h) \,\middle|\, c(h, i, j) > 0 \right\}, \tag{20}$$

$$h_{\max}(i, j) = \left\{ \max(h) \,\middle|\, c(h, i, j) > 0 \right\}. \tag{21}$$

The sum of all ray fractions inside the sector element $(i, j)$ gives a measure of the area of the element:

$$a(i, j) = \sum_h c(h, i, j) \,. \tag{22}$$

Since the ray width varies in a fan beam geometry, $a(i, j)$ is not a true area. Nevertheless, it represents adequately the size of the element needed in the following calculations.

The coefficients $c(h, i, j)$ are calculated for a given log distance $d_1$. To apply these coefficients to other distance values, the input images must be zoomed by remapping the detector element index $h$. To obtain accurate results with a wide range of log positioning, there must be several sets of coefficients, each being used for a certain distance interval.

### 3.2.4 The application of knowledge on wood

A few simple rules are utilised in the detection of knots. The rules are concerned with the geometry and density of typical stems and knots. It has to be understood that the assumptions below are approximations and do not hold exactly for natural wood. We have to be satisfied with a simplified solution that best fits the insufficient data. For that purpose, the rules are valuable.

- The cross-section of the stem is approximately elliptical. The size of the cross-section can be estimated with the average of the diameters from the three projections. The maximum value of those diameters is used to define a circle containing the reconstructed image of the cross-section.

- The starting point of the knot is located on the axis of the stem. A knot is modelled as a cut cone, which can be described with the rotation angle $\alpha$, the rise angle $\beta$, the opening angle $\gamma$, and the radial length $r_k$. The radial length is the distance between the end of the knot and the pith. In most cases, the rise angle $\beta$ is from 0° to 50°.

- All the knots in a cluster start nearly at the same point. The neighbouring knots cannot lie immediately side-by-side; we assume a minimum rotational distance of 40°. In a very knotty log, the rotational distance can be smaller. Such a knot pattern could not be distinguished with our method.

- The stem density varies both radially and longitudinally. The radial variation is so wide that it has a considerable effect on the visibility of knots in x-ray images. This effect must be compensated for.

### 3.2.5 Evidential reasoning

Later in this chapter we shall use *evidential reasoning* for locating knots. A group of pixels in a projection image gives us evidence that certain volume elements might belong to a knot. Pieces of evidence are gathered from all the projections and combined, resulting in a *belief value* for each volume element. The process continues with combining beliefs of adjacent volume elements, producing a belief value for a sector to contain a knot.

In our case, evidence can be either positive or negative. Evidence is actually a probability value that is scaled in the interval [–1, 1]. Values –1, 0, and +1 correspond to the phrases “definitely no”, “undetermined”, and “definitely yes”.

For combining evidences $e_1$ and $e_2$, we introduce an operator recommended by Cheng & Kashyap (1989),

$$\mathrm{E}(e_1, e_2) = \frac{e_1 + e_2}{1 + e_1 e_2}. \qquad (23)$$

The operation is extended to more arguments by noting that

$$\mathrm{E}(e_1, e_2, e_3) = \mathrm{E}(\mathrm{E}(e_1, e_2), e_3)\,. \tag{24}$$

Cheng's operator was selected, because it is easy to use, and it has certain good properties. The operation is *commutative* and *associative* meaning that the result does not depend on the order in which the set of evidence is gathered. The combination function is also *monotonic*, i.e. stronger evidence creates higher belief values for the hypothesis.

Evidence is derived from some logical or physical variables, such as density in our case. To gain robustness in the reasoning, the elementary evidence must be determined carefully. One erroneous value near the end-points –1 or +1 may distort the combined belief. When calculating evidence on density values of volume elements, we must make sure of the reasonableness of the result by setting an upper limit for the density.

The number of pieces of evidence also affect the scaling of evidence values. For example, we may state that combining *n* "fairly positive" elements should produce belief *b*. We then have to find proper evidence *e* that fulfils the condition E(*n* pieces of *e*) = *b*.

## 3.3 PRE-PROCESSING OF X-RAY IMAGES

Pre-processing means normalisation and linearisation of pixel values, as well as locating the object and centring it for 2-D processing. All these functions are quite mechanical operations that could be implemented with hardware in the imaging system. In our case, however, the processing has been executed off-line in a PC.

### 3.3.1 Log end detection

In continuous operation, the imaging system has to detect the start and stop ends of the log. This can be done easily by observing row sums of the image. When the sum exceeds a given threshold, a log is present at the imaging line. If a log end has been cut slanting, the three projections may see the end lines at different places. We must then use some logic to resolve the discrepancy. Our rule is that all projections must agree about the presence of the log.

### 3.3.2 Averaging lines to slices

A length encoder is included in the conveyor so that the longitudinal co-ordinate can be attached to every line of pixels. The number of lines per unit length varies with the conveyor speed. As we would like to handle slices of constant thickness, the pre-processing should include an algorithm for transforming a number of lines to slices. In our system, the slices are calculated by averaging the lines whose longitudinal co-ordinates fall within the same centimetre.

### 3.3.3 Pixel value normalisation

Every detector element is an individual. The sensitivity variation within an array of photodiodes is typically less than 1 %, but more inaccuracy comes from optical coupling between the scintillation crystal and the photodiode. The total sensitivity of an element may be as low as 50 % of the sensitivity of the best element in an array. Another problem is the temperature dependence of the photodiode: the dark current of the diode is doubled with a temperature rise of 10 degrees. This results in an offset current, which is summed into the current caused by the optical signal. To overcome the gain and offset variations, each measured detector element of value $d_{out}$ is normalised with two calibration values $d_{dark}$ and $d_{full}$:

$$\mathrm{d}_{\mathrm{norm}} = \mathrm{C} \cdot \frac{\mathrm{d}_{\mathrm{out}} - \mathrm{d}_{\mathrm{dark}}}{\mathrm{d}_{\mathrm{full}} - \mathrm{d}_{\mathrm{dark}}}. \tag{25}$$

The offset value $d_{dark}$ is measured without x-rays, and the maximum value $d_{full}$ with full radiation when no object is present. The constant C scales $d_{norm}$ to the appropriate number range.

### 3.3.4 Linearisation

In order to establish the object density, values proportional to the linear attenuation coefficient $\mu$ have to be obtained. The attenuation law of Equation (7) can be solved for $\mu$ by taking logarithms of both sides and rearranging,

$$\mu = \frac{1}{x} \log \frac{J_0}{J}. \tag{26}$$

As stated in Chapter 2.1, this simple law is distorted by multiple scattering and beam hardening. The linear attenuation coefficient given by Equation (26) decreases with increasing object thickness, resulting in inconsistency between measurements from different angles. To determine a more accurate model of attenuation, we have measured values $J_0/J$ with varying material thickness. The experiment showed that the attenuation law appropriate for our imaging equipment is

$$J / J_0 = (1 + b \cdot (\mu x)^2) \cdot e^{-\mu x}, \tag{27}$$

where $b$ is an experimental coefficient.

We would like to linearise the pixel values to produce the thickness of the material in centimetres at a given average density, e.g. 1000 kg/m$^3$. Knowing the chemical elements of wood, a typical value of $\mu$ can be gathered from literature (as Compton & Allison 1960). The energy spectrum of the source has to be considered when determining the proper value for $\mu$. Coefficient $b$ depends on the radiation collimation of the set-up, and must always be determined experimentally.

Object thickness $x$ is solved from Equation (27) by iteration and saved into a look-up table for use in the linearisation process:

$$\mathrm{LT}(d_{norm}) = \left\{ x \,\middle|\, d_{norm} = (1 + b \cdot (\mu x)^2) \cdot e^{-\mu x} \right\}, \tag{28}$$

where $d_{norm}$ is the normalised value of a pixel, $d_{norm}$ = 1...65535. Then, the linearised pixel value $d_{lin}$ can be taken from the look-up table,

$$d_{lin} = \mathrm{LT}(d_{norm}) . \tag{29}$$

### 3.3.5 Edge detection and object centring

The edges of the log are determined for two reasons: the radius of the log must be known in the following computation, and the log must be centred in relation to the co-ordinate system.

Finding the edges is performed by simply thresholding the projection slice values with $t$:

$$\begin{aligned} h_l &= \left\{ \min(h) \,\middle|\, d_{lin}(h) > t \right\}, \text{ and} \\ h_r &= \left\{ \max(h) \,\middle|\, d_{lin}(h) > t \right\}. \end{aligned} \tag{30}$$

Symbols $h_l$ and $h_r$ refer to the left and right edges of the log, as projected on the detector. The threshold $t$ is selected to correspond to some centimetres of wood.

The mid point of the slice is the average of $h_l$ and $h_r$. Before the actual centring, the centre line consisting of successive mid points must be filtered to remove the effects from curved edges. Then, every slice is centred by shifting its pixels by such number of steps that the mid point coincides with the central line of the image space.

## 3.4 ACQUISITION OF 2-D KNOT DATA

### 3.4.1 Locating knot clusters

To save computation time, we pay attention to only those pieces of the log that seem to contain knots. A hint of a knot cluster is obtained from the row sums: an image row containing knot pixels has a greater sum than its neighbours without knot pixels. Therefore we calculate the sum of all slices $k$ of the log from the three projection images $p_0$, $p_1$, and $p_2$:

$$S_{rows}(k) = \sum_{m=0}^{2} \sum_{h=1}^{n} p_m(h,k) . \tag{31}$$

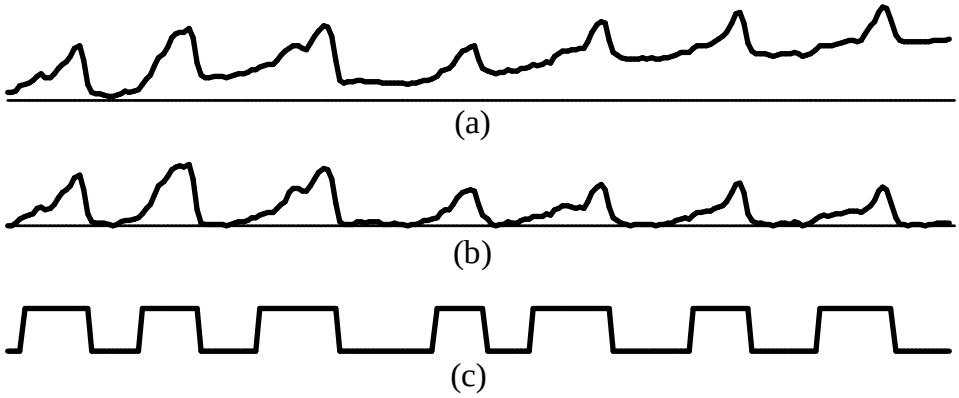


*Figure 11. (a) Row sum of a log image indicates the locations of knot clusters. (b) The effect of changing stem thickness is eliminated by comparing each point to the minimum of a gliding window. (c) The knot sections in the log are detected by median filtering of curve b.*

We include all three projections in the row sums to get a reliable result. Figure 11 presents an example of the variation of row sums along the length of the log. The locations of knot clusters are clearly seen in the curve. As one might expect, the thickness of the log also contributes to the sums. Local characteristics of the curve should therefore be observed to locate the clusters. We do this by comparing each point with the minimum of a neighbourhood window. The window should be as narrow as possible to keep the calculation simple, but it still should be wide enough to contain a long cluster. We have selected the width of 31 points, because most knot clusters are shorter than 31 centimetres.

The start and end co-ordinates of the clusters are then determined by median filtering which is highly suitable for this application because of its robustness. Additionally, we expect that more than half of the log is normal wood without knots, and so the rows with sums above the median would most likely contain all the knot areas.

We used a brute-force method based on sorting to determine the median. Since this operation is needed only once per piece of a log, its computational effectiveness is not critical. Better methods are surveyed by Juhola et al. (1991) and Astola & Campbell (1989).

### 3.4.2 Removing the background

After locating the knot clusters, we shall filter out the normal wood from the image to uncover deviations caused by knots. The nature of our object suggests one-dimensional filtering. As the log is scanned lengthwise, the gradients in image columns are small, while rows reflect the round shape of the stem. Figure 12 shows some columns of a log image.

Potential methods for approximating the body of the wood include averaging or median filtering with a sliding window. When selecting the method, we have to take into account that the thickness of the stem changes at the knot cluster. This is especially true for the top part of the stem. The

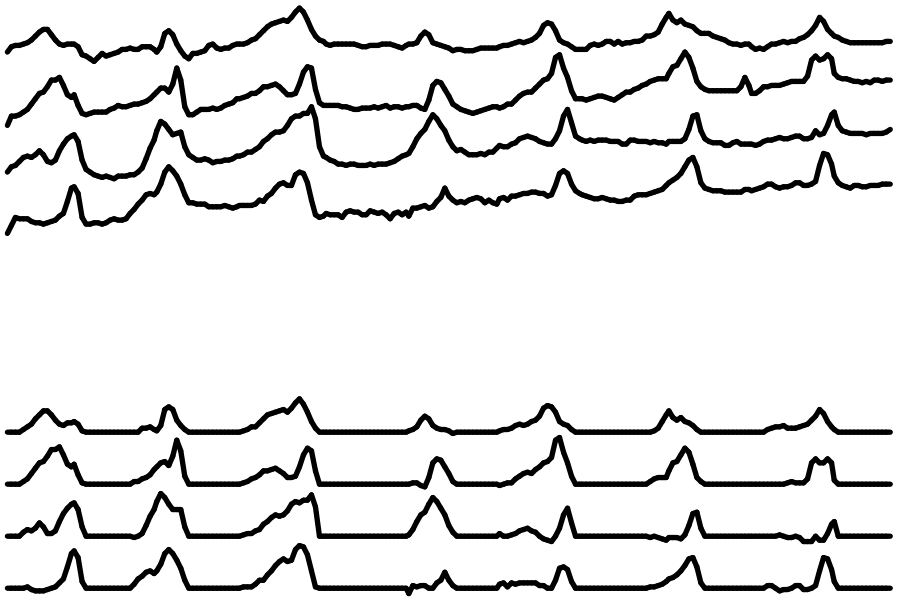

*Figure 12. Curves at the top refer to columns of a log image. The background is removed by zeroing the points outside cluster sections and subtracting interpolated values inside clusters (bottom).*

thickness change appears as a step in the image column. Most easily, the step is eliminated by linear interpolation over the cluster section. The background is then removed column-by-column producing a difference image:

- Outside cluster sections, set the difference image to zero.
- Inside a cluster section,
  - pick up reference values from rows just preceding and following the cluster section,
  - calculate the background value for a pixel by linear interpolation from the reference values, and
  - subtract the background value from the original pixel value.

For every knot cluster, the two-dimensional processing results in three projection images $p_m(h, k)$ containing the knot information. Additional parameters to be saved are the starting co-ordinate $z_0$, and the left and right edge points of the cluster.

## 3.5 RECONSTRUCTION OF KNOTS

The three-dimensional processing falls into three parts. First, we compute some collective properties of a knot cluster describing the over-all quality of that part of the log. As we shall see later, this may be the only information we are able to obtain in the worst case. Then we look for candidate angles for the knots utilising fuzzy reasoning. Finally, the reconstruction is concluded by backprojecting the three projection images into the candidate angles.

### 3.5.1 Computing collective cluster properties

The main input of this stage are the three projection images $p_0(h,k)$, $p_1(h,k)$, and $p_2(h,k)$. We start with fitting them into the co-ordinate system, i.e. finding values $k_1$, $k_2$, and $j_{max}$, which set boundaries to the cylinder containing the knot cluster. The basis for most of the following calculation will be a new image obtained by averaging the six halves of the input images:

$$p_a(h,k) = \sum_{m=0}^{2}((p_m(h,k) + p_m(n+1-h,k))/6\,. \tag{32}$$

Averaging is done for all slices $k$ of the cluster with $h = 1...h_c$, where $h_c$ is $n/2$, half of the number of detector elements (see Figure 13). The idea behind using image $p_a$ instead of the original images $p_m$ is to reduce computation. At the moment, we are only interested in properties that are symmetrical in respect to the central line of the images.

***Boundaries of the knotty volume in a cluster***

The limits $k_1$ and $k_2$ of the longitudinal co-ordinate are set so that the knot volume lies within them. Because images always contain some noise, it is not reasonable to include all non-zero slices. We have to allow for a tolerance that is represented by the multiplier $\delta$ in the following equations. The value of $\delta$ is not critical, and it may be for example 0.01.

$$k_1 = \left\{\max(k_x) \,\middle|\, \sum_{k=1}^{k_x}\sum_{h} p_a(h,k) \le \delta \cdot \sum_{k}\sum_{h} p_a(h,k)\right\}, \tag{33}$$

$$k_2 = \left\{\max(k_x) \,\middle|\, \sum_{k=1}^{k_x}\sum_{h} p_a(h,k) \le (1-\delta) \cdot \sum_{k}\sum_{h} p_a(h,k)\right\}. \tag{34}$$

To simplify things later, $k$ is normalised by subtracting $k_1$–1. Then the slice numbers under examination are $k = 1...k_{max}$, where $k_{max} = k_2 - k_1 + 1$.

We have found earlier the edge pixels of each projection along the stem, defined by Equation (30). Taking these edge points from a reference line $k_{ref}$ just below the knot cluster, we can calculate an approximate radius for the cluster in centimetres as seen from direction $m$,

$$r_m = \left[h_{rm}(k_{ref}) - h_{lm}(k_{ref})\right] \cdot w_{d0}/2\,, \tag{35}$$

where $w_{d0}$ is the pixel width at the origin plane, and $m$ = 0, 1, and 2.

The maximum of the three projection radii $r_m$ is then quantised with $\Delta r$ = 2 centimetres to obtain the number of rings $j_k$ in the cylindrical co-ordinate system:

$$j_k = \mathrm{Int}(\max(r_0, r_1, r_2) / \Delta r) + 1\,. \tag{36}$$

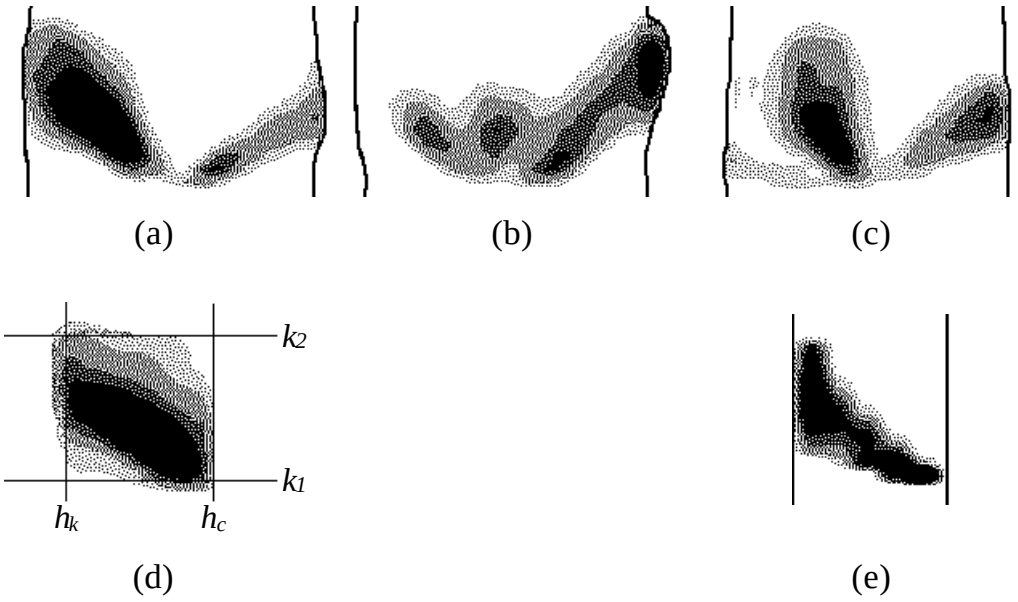


*Figure 13. The six halves of the three projections (a-c) are averaged to obtain an image characterising the over-all properties of the knot cluster (d). The top and bottom slices of the cluster are numbered $k_2$ and $k_1$. Horizontally the knots are located between the central line $h_c$ and the outer limit $h_k$. A collective reconstruction of the cluster is then computed (e), as described later in this chapter.*

Especially in butt end logs, knots do not always reach the stem surface. The knotless sapwood has a high value, and thus it is important to know its thickness. We determine the cylinder holding the knots, which is characterised by radius $r_k$. First, an image column $h_k$ is sought such that the interval $h = 1...h_k$ contains only a minor portion $\delta$ of the knot volume. Again, the parameter $\delta$ is a tolerance multiplier as in Equations (33) and (34).

$$h_k = \left\{ \max(h_x) \,\middle|\, \sum_k \sum_{h=1}^{h_x} p_a(h,k) \le \delta \cdot \sum_k \sum_{h=1}^{h_c} p_a(h,k) \right\}. \qquad (37)$$

The knot cylinder radius in centimetres is then calculated as

$$r_k = (h_c - h_k + 1) \cdot w_{d0}. \qquad (38)$$

### *Cluster shape*

An important constraint for the reconstruction comes from the cluster shape. It is quite reasonable to assume that, in most cases, the following is true in our approximate log model:

- All knots start at the origin of the co-ordinate system when the projection images are centred and cut as described earlier.
- All knots are inside radius $r_k$.
- The steepest knots reach the topmost slice $k_{max}$ at radius $r_k$.
- The rise angles of all knots are positive.

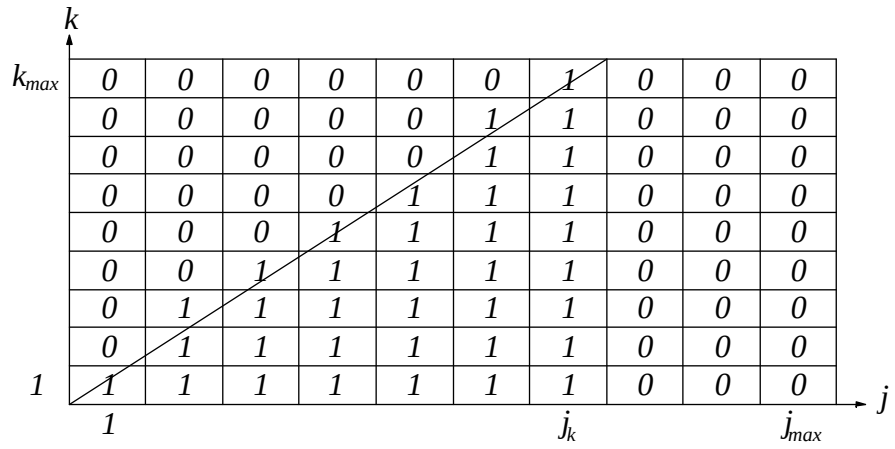


*Figure 14. Mask function w(j, k) includes elements (j, k) under the maximum slope line and excludes those above the line. The value of w(j, k) is also 0 for rings $j > j_k$.*

The model stated above is not exact. Knots in a natural log do not start at the geometrical centre of the log but at the pith, which may be centimetres away from the centre. Likewise, real knots are not always straight as assumed by the last rule. These remarks are not totally relevant, because we are looking for a simplified model that best fits the data measured, not an exact form of natural knots.

A *shape mask function w(j, k)* is developed according to the rules above. Figure 14 illustrates this coefficient function, which is 1 where knots are expected to reside and 0 everywhere else. The maximum slope is fixed by coefficient $k_{max} / j_k$, and the maximum distance from the centre by ring number $j_k$. The shape mask function is defined as

$$w(j,k) = \begin{cases} 1 & \text{if } k < \dfrac{k_{\max}}{j_k} \cdot j + 0.5 \text{ and } j \le j_k, \\ 0 & \text{otherwise.} \end{cases} \tag{39}$$

To take function *w(j, k)* into account in the reconstruction, we need to calculate another variable $l_s(h, k)$. It is the sum of coefficients *c(h, i, j)* along ray *h* in slice *k*, weighted by function *w(j, k)*. Effectively it gives the length of the potential knot space along that ray.

$$l_s(h,k) = \sum_i \sum_j w(j,k) \cdot c(h,i,j), \tag{40}$$

which is calculated for all $k = 1...k_{max}$ and $h = h_{min}(i, j)...h_{max}(i, j)$. See Figure 15 for clarification.

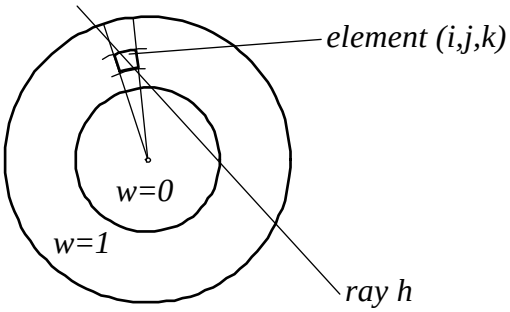


*Figure 15. In a given slice k, function w(j, k) is zero within the inner circle, and unity outside the circle. The actual length of ray h through the slice is the sum of c(h, i, j) of every passed element (i, j, k). The effective ray length $l_s$ is obtained by weighting each c(h, i, j) with w(j, k).*

***Radial density variation***

The wood density is known to vary considerably as a function of distance from the pith, as described in Chapter 2.2. The heartwood is dry, whereas the vital sapwood contains a lot of moisture and is more dense. How a knot stands out from the background wood depends on the location of the knot and on the freshness of the log. With wood density $\rho_w$ and knot density $\rho_k$, the contrast of the knot image is proportional to $\rho_k$ - $\rho_w$. To enhance the contrast, we shall multiply the images by a correction coefficient

$$c_\rho = \frac{\rho_k}{\rho_k - \rho_w}. \tag{41}$$

We shall face problems when $\rho_w$ approaches $\rho_k$ or possibly exceeds it: the image disappears and $c_\rho$ comes vague. Obviously the coefficient must be restricted to some reasonable positive values, say 1 to 10.

If an object is known to be cylindrically symmetrical, it can be reconstructed from one projection (Deutsch et al. 1990). To a certain extent, a log can be considered to be a cylindrical object. Thus we can find an estimate for the radial density variation using the principles given in the literature. Appendix A presents a derivation of the radial density function and the radial correction coefficient $c_\rho(j)$.

***Collective reconstruction of a cluster***

Our next target is to derive the *collective reconstruction Q(j, k)* of the knot cluster. We start with backprojecting $p_a(h, k)$, the average of the three projections, to volume elements *(i, j, k)*. The contribution of ray *h* to element *(i, j, k)* in slice *k* is

$$q_h(i,j,k) = w(j,k) \cdot c(h,i,j) \cdot p_a(h,k) / l_s(h,k). \tag{42}$$

The ray sum $p_a(h, k)$ is simply distributed along ray *h*, taking into account the shape function *w(j, k)*. Note that Equation (32) defines $p_a(h, k)$ only for

one half of the projection where $h \le n/2$. For greater values of $h$, $p_a(h, k)$ are replaced with $p_a(n+1 - h, k)$ by symmetry.

We then sum up all rays relevant to element $(i, j, k)$, and divide the result by the sum of ray sections within that element:

$$q_s(i, j, k) = \frac{1}{a(i, j)} \sum_{h=h_1}^{h_2} q_h(i, j, k), \tag{43}$$

where $h_1 = h_{min}(i, j)$, $h_2 = h_{max}(i, j)$. Since $q_h(i, j, k)$ is a line integral of density, Equation (43) gives an estimate for the density of element $(i, j, k)$.

To obtain the final reconstruction as one single 2-D image, we combine all sectors $i$. At the same time, we compensate for the effect from radial density variation with the multiplier $c_\rho(j)$.

$$Q(j, k) = c_\rho(j) \cdot \sum_i q_s(i, j, k), \tag{44}$$

where $i = 0...i_{max}$, $j = 1...j_{max}$, and $k = 1...k_{max}$.

$Q(j, k)$ is a combined cross-section of all knots in the cluster. It comprises information about the maximal dimensions, density distribution, and total volume of the cluster. Figure 13 gives an example of how three projections develop into a collective reconstruction image.

Each $Q(j, k)$ is a sum of densities from equal-sized elements. Assuming an average knot density $\rho_k$, we obtain an estimate for the total knot volume as

$$V = \frac{1}{\rho_k} \sum_{j=1}^{j_{max}} v(j) \cdot \sum_{k=1}^{k_{max}} Q(j, k), \tag{45}$$

where $v(j)$ is the volume of an element in ring $j$. It is obtained by

$$v(j) = \frac{\Delta\alpha \cdot (\Delta r)^2 \cdot \Delta z}{2} \cdot (2j - 1), \tag{46}$$

where $\Delta\alpha$ is the sector angle, $\Delta r$ the ring width, $\Delta z$ the slice thickness, and $j$ the ring index.

### *Density parameters*

In the next section, we use the parameters *critical density* and *maximum density* calculated as

$$\rho_{max} = \max\{Q(j, k) \mid 1 \le j \le j_{max},\ 1 \le k \le k_{max}\}, \text{ and} \tag{47}$$

$$\rho_{crit} = \rho_{max}/(2 \cdot j_{max}). \tag{48}$$

Maximum density $\rho_{max}$ is the highest value in the collective reconstruction image. We expect that there are normally no higher densities than $\rho_{max}$ in the cluster. Usually $\rho_{max}$ is due to multiple knots, and it is noticeably greater

than actual densities of any volume element. Critical density $\rho_{crit}$ is the detection limit for a knot: if a volume element has a calculated density lower than $\rho_{crit}$, it probably does not contain knots.

Equation (48) needs some explanation. The diameter of a slice is $2 \cdot j_{max}$. If there is only one knot element with density $\rho_{max}$ in the slice, it will produce element densities of at least $\rho_{crit}$ when distributed along any projection line. Thus, volume elements with densities greater than $\rho_{crit}$ are considered to be potential knot elements, while the others are likely to be empty.

As will be discussed later, parameters $\rho_{max}$ and $\rho_{crit}$ are not used as hard thresholds, but rather as a basis for calculating evidence of knot existence.

### 3.5.2 Finding the candidate angles

After having found some over-all characteristics of the cluster, we now start looking for locations of individual knots. First, the three projection images - one at a time - are backprojected on to cross-sections. This produces approximated density values for each volume element. Using parameters $\rho_{crit}$ and $\rho_{max}$ defined in Chapter 3.5.1, the densities are then scaled into evidence values. Finally, combining evidence results in belief values that indicate the potential knot sectors.

The backprojection process is the same as that described earlier in the case of the collective reconstruction. The contribution of the projection image $p_m(h, k)$ to a given volume element $(i, j, k)$ is calculated as

$$u_m(i,j,k) = w(j,k) \cdot \sum_{h=h_1}^{h_2} c(h,i_m,j) \cdot p_m(h,k) / l_s(h,k) . \qquad (49)$$

The three projections $m = 0...2$ are handled with all sectors $i = 0...i_{max}$, rings $j = 1...j_{max}$, and $k = 1...k_{max}$. The summing limits of h are $h_1 = h_{min}(i, j)$ and $h_2 = h_{max}(i, j)$.

The resulting $u_m(i, j, k)$ is a line integral of density, as in $p_m(h, k)$. The sum of the rays within element $(i, j)$ is $a(i, j)$. Therefore, dividing $u_m(i, j, k)$ by $a(i, j)$ yields a number proportional to the density. The radial density correction is accomplished with another multiplier $c_\rho(j)$, yielding

$$\rho_m(i,j,k) = u_m(i,j,k) \cdot c_\rho(j) / a(i,j) . \qquad (50)$$

The density value of a volume element is converted into evidence defined as

$$e_m(i,j,k) = \begin{cases} e_2 \cdot \dfrac{\rho_m(i,j,k) - \rho_{crit}}{\rho_{max} - \rho_{crit}} & , \rho_{crit} \le \rho_m(i,j,k) \le \rho_{max} , \\ e_2 & , \rho_m(i,j,k) > \rho_{max} , \\ e_0 \cdot \dfrac{\rho_{crit} - \rho_m(i,j,k)}{\rho_{crit}} & , \rho_m(i,j,k) < \rho_{crit} . \end{cases} \qquad (51)$$

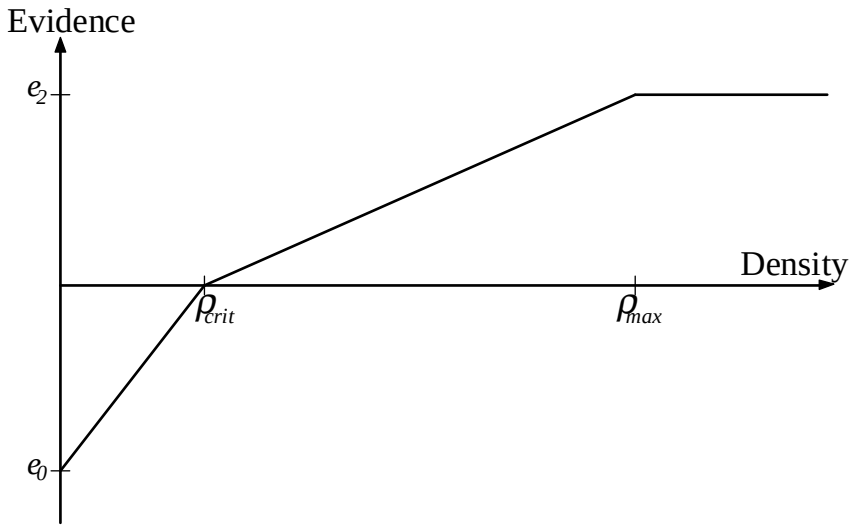


*Figure 16. The function transforming estimated element density to evidence of knot existence.*

Figure 16 portrays the function in Equation (51). The evidence values are limited between $e_0$ and $e_2$ to suppress the effect of abnormally high or low densities. The absolute values of $e_0$ and $e_2$ should always be clearly less than 1 to prevent one erroneous value from distorting the final result. Safe figures are $e_0 = -0.5$ and $e_2 = 0.5$. Densities $\rho_{crit}$ and $\rho_{max}$ are the parameters defined in Chapter 3.5.1.

The evidence from the three projections are combined, element by element, using the operator defined in Equations (23) and (24),

$$e_c(i,j,k) = \mathrm{E}\left[e_0(i,j,k), e_1(i,j,k), e_2(i,j,k)\right]. \tag{52}$$

At this point we have generated a three-dimensional image $e_c(i, j, k)$ of the object into a cylindrical co-ordinate system. The image is *fuzzy*, meaning that the values of individual volume elements are rather probabilities of knot existence than densities. In the following, we shall combine elements to knot shapes and calculate the evidence values of those shapes. First we go through all sectors $i$ observing a discrete set of rise angles $\beta = 0 \ldots \beta_{max}$. The evidence of the sector element $(i, j)$ at rise angle $\beta$ is calculated as

$$e_r(i,j,\beta) = \left(\sum_k \mathrm{F}(j,k,\beta)\cdot e_c(i,j,k)\right)/(j_{max}/2). \tag{53}$$

Equation (53) computes a weighted sum of the evidence of volume elements. The weighting function F includes the elements occurring in direction $\beta$; the exact definition of F is in Appendix A. Evidence is scaled with $2/j_{max}$ to obtain reasonable values when combining $j_{max}$ elements in the next step:

$$e_s(i,\beta) = \mathrm{E}(e_r(i,1,\beta),\ldots,e_r(i,j_{\max},\beta)). \tag{54}$$

This intermediate result expresses the evidence of knot existence in sector $i$ at rise angle $\beta$. The greatest of $e_s(i, \beta)$ is selected to represent the sector:

$$e_t(i) = \max(e_s(i,0),\ldots, e_s(i,\beta_{\max})) . \tag{55}$$

Angle $\beta$, which maximises the sector evidence, is taken as an estimate for the rise angle, and is denoted by $\beta(i)$.

Each sector $i$ now has evidence $e_t(i)$ characterising its probability of containing a knot. Figure 17 shows the evidence curve of an example case. Which sectors should we select as probable knot sectors? Obviously, a candidate must be a local maximum, but how wide a neighbourhood should be considered? The experimental part in Chapter 4 includes tests on this property; the results have encouraged us to choose a window size of seven sectors. It is yet another question if all local maxima are potential knot candidates. This was also tested, resulting in the condition that the evidence has to exceed a given threshold $e_{th}$. Not surprisingly, an appropriate value for $e_{th}$ appears to be about 0. To conclude, the sectors meeting all the criteria in Equation (56) are selected as candidate knot angles.

$$\begin{cases} e_t(i) > \max(e_t(i-3), e_t(i-2), e_t(i-1)) , \\ e_t(i) > \max(e_t(i+1), e_t(i+2), e_t(i+3)) , \text{and} \\ e_t(i) > e_{th} . \end{cases} \tag{56}$$

One would expect that evidence $e_t(i)$ is a measure of certainty of the hypothesis that the selected sector $i$ really contains a knot. We shall return to this question in Chapter 4 with the experimental results.

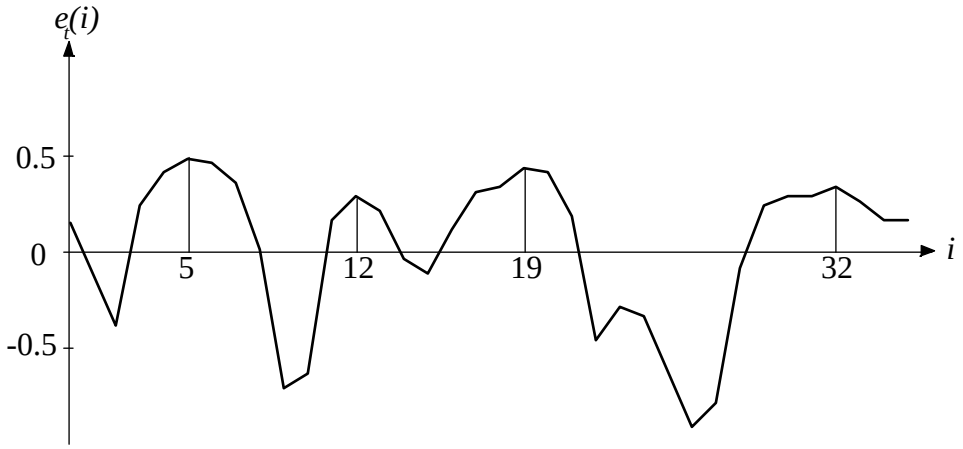


*Figure 17. Evidence curve of a cluster indicates knot candidates in sectors 5, 12, 19, and 32.*

### 3.5.3 Backprojection

The last step in the reconstruction of knots is the backprojection of the three images $p_m(h, k)$ into a 3-D cylindrical space. The computation is very much similar to that described in Equations (49) and (50). However, this time we consider only those sectors $i$ that have been selected as candidate sectors; rest of the volume is thought to be empty. We denote the set of knot sectors by $I_k$. Also the approximate rise angle $\beta(i)$ is taken into account when restricting the knot location. The rise angle constraint is set by mask function $G(j, k, \beta)$ defined in Appendix A.

We first calculate $l_{sm}(h, k)$, the sum of coefficients $c(h, i, j)$ along ray $h$ in slice $k$ weighted by function $G(j, k, \beta)$. This is done for all slices $k = 1...k_{max}$, all rays $h$, and all projections $m = 0, 1, 2$.

$$l_{sm}(h,k) = \sum_{i \in I_k} \sum_{j=1}^{j_k} \mathrm{G}(j,k,\beta(i_m)) \cdot c(h,i_m,j)\,. \tag{57}$$

The contributions of the three projections are backprojected into the cylinder space $S(i, j, k)$. For knot angles $i \in I_k$, all rings $j$, and all slices $k$, the three projections are averaged by

$$S(i,j,k) = \frac{1}{3} c_\rho(j) \cdot \sum_{m=0}^{2} G(j,k,\beta(i_m)) \sum_{h=h_1}^{h_2} c(h,i_m,j) \cdot p_m(h,k) / l_{sm}(h,k)\,, \tag{58}$$

where $h_1 = h_{min}(i_m, j)$ and $h_2 = h_{max}(i_m, j)$. The total knot mass is thus distributed this way to those sectors that have been chosen as candidate sectors. The radial density variation is compensated for with $c_\rho(j)$. Figure 18 shows an image of $S(i, j, k)$ for a given knot sector $i$.

An auxiliary variable $S_a(i, j)$ is calculated for the estimation of knot lengths. It represents all the knot mass in sector $i$ that resides in rings $1...j$:

$$S_a(i,j) = \sum_{j_1=1}^{j} \sum_{k=1}^{k_{max}} S(i,j_1,k)\,. \tag{59}$$

The length of the knot in sector $i$ is found by observing the growth of $S_a(i, j)$ with increasing $j$. In an ideal case $S_a(i, j)$ drops to zero with a particular $j$. In reality, interference from other knots may create non-zero values also for empty volume elements. Thus we have to allow a fraction $\delta$ of the calculated volume to remain outside the knot length $r_t$. The knot length is interpolated using Equations (60) and (61):

$$j_t(i) = \left\{ j \,\middle|\, S_a(i,j) \le (1-\delta) \cdot S_a(i,j_{\max}) < S_a(i,j+1) \right\}, \tag{60}$$

$$r_t(i) = \Delta r \cdot \left[ j_t(i) + \frac{(1-\delta) \cdot S_a(i,j_{\max}) - S_a(i,j)}{S_a(i,j+1) - S_a(i,j)} \right]. \tag{61}$$

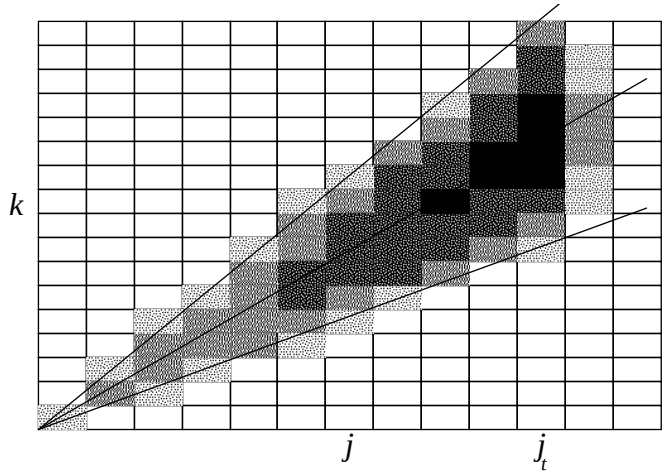


*Figure 18. A knot profile obtained from the backprojection process.*

The rise angle $\beta$ and opening angle $\gamma$ are sought by calculating statistical properties of the knot pattern in Figure 18. Imagine a straight line from the origin to the centre of element *(j,k)*. When the dimensions are expressed in centimetres, the slope of such a line is

$$t(j,k) = \frac{(k-0.5)\cdot \Delta z}{(j-0.5)\cdot \Delta r}. \tag{62}$$

The first and second moments of the slopes *t(j,k)* are

$$m_1 = \frac{1}{s}\sum_{j=1}^{j_{\max}}\sum_{k=1}^{k_{\max}} t(j,k)\cdot S(i,j,k), \text{ and} \tag{63}$$

$$m_2 = \frac{1}{s}\sum_{j=1}^{j_{\max}}\sum_{k=1}^{k_{\max}} t(j,k)^2\cdot S(i,j,k), \tag{64}$$

where *s* is the sum of all *S(i, j, k)* in sector *i* calculated by

$$s = \sum_{j=1}^{j_{\max}}\sum_{k=1}^{k_{\max}} S(i,j,k). \tag{65}$$

The first moment $m_1$ is the average of *t(j,k)*, and thus an estimate for the rise angle can be obtained by

$$\beta = \tan^{-1}\left(m_1\right). \tag{66}$$

Recalling the statistics, the mean deviation is calculated from the moments by

$$D = \sqrt{m_2 - m_1^2}. \tag{67}$$

In an ideal case with a conical and homogeneous knot, the mean deviation D turns out to be exactly half of the maximum deviation. Noticing the effect of $\beta$ on the slope, we finally obtain an estimate for the opening angle $\gamma$ by

$$\gamma = \tan^{-1}\left(2D\cos^2\beta\right). \tag{68}$$

The total knot volume in sector $i$ can now be estimated from other geometrical parameters of the knot:

$$V(i) = \frac{\pi \cdot r_t(i)^3 \cdot \tan^2\gamma}{3\cos^3\beta}. \tag{69}$$

Equations (68) and (69) are derived in Appendix A.

## 3.6 USE OF THE RESULTS

We have obtained two kinds of measures describing the knots in a log: collective cluster properties and individual knot properties.

The collective cluster properties include total knot volume $V$ and knot cylinder radius $r_k$. $V$ and $r_k$ can be used to estimate the log quality without knowing the detailed knot pattern. For example, the knot volume per log volume may serve as an index for the log quality. Radius $r_k$ defines the cylinder containing all the knots in a cluster, thus indicating the thickness of clear sapwood. Normally only the knots on the sawn surfaces matter, so $r_k$ guides us in selecting the blade set-up.

The size and orientation of individual knots are characterised by the length $r_t$ and angles $\alpha$, $\beta$, and $\gamma$. Starting from these parameters, one is able to calculate the expected locations and areas of knots on potential sawing surfaces. Thus the value of the log can be estimated for several blade set-ups before sawing. Further process optimisation might include trimming the log or finding the best sawing position according to the knot information.

Even though not discussed here in detail, log geometry is an essential part of log sorting. At least the top end diameter must be known for proper classification. An x-ray detector has an advantage over optical instruments because of its ability to find the diameter of the log under the bark.

# 4 EXPERIMENTS

The experiments included both simulations and imaging of real pine logs at normal sawing speeds with x-rays. These two methods were complementary to each other: while true x-ray images contained typical variations of natural wood and noise from the measurement system, simulations were useful for obtaining accurately controlled test material.

## 4.1 PRELIMINARY TESTS

The first trial in the research project was to take a piece of log to a local hospital, where it was imaged using a medical x-ray generator and a short detector module.

The results encouraged us to set up a test environment in a laboratory. It included a controllable x-ray generator, a line detector block with 8-bit resolution, and a mechanism to move logs over the detector. With this equipment, we could image log pieces as big as 40 centimetres thick and 80 centimetres long. A series of tests was conducted to gain further knowledge about the x-ray characteristics of wood. Especially important was to check the total attenuation of normal-sized logs and the contrast between various knots and stemwood. The experience from these tests also helped in the development of new imaging hardware which was to be used in the next stage of the project.

## 4.2 LOG IMAGING WITH A FULL-SCALE SYSTEM

Finally, we were able to construct a full-scale imaging system to handle logs in sawmill-like conditions. A conveyor moved the logs at typical saw-mill speeds from 1 to 2.5 m/s. The detector was now 90 centimetres long, and its resolution was 16 bits. This was good enough to manage logs up to 50 centimetres in diameter.

Only one source-detector pair was available, and thus three passes were needed to image one log. This caused some trouble in controlling the rotational angle: some logs refused to keep their position during the transport through the system. Obviously, the consistency of the three projections suffers if their rotational angles are inaccurate. The only way to overcome this problem was to observe visually the log passage, and then reject those logs that moved their position.

After imaging, the logs were sawn up into square timber and visually inspected for knots. This practice was a compromise: most of the information needed was achieved with a tolerable amount of work. A complete autopsy of logs would have been extremely laborious.

The sawn surfaces were inspected visually, recording the knot size and the knot co-ordinates $x$, $y$, $z$. The size of the knot is expressed by diameter $d$, which is the average of the main diameters of the elliptical knot

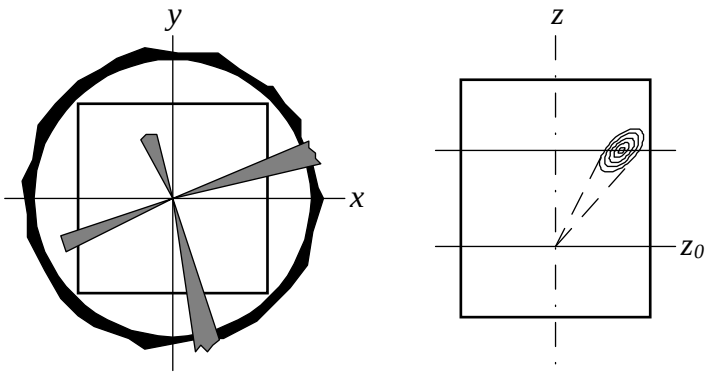


*Figure 19. After imaging, the log under inspection was sawn into square timber as shown in the picture on the left. The co-ordinates and sizes of knots were measured on the log surface as well as on the faces of the sawn timber.*

pattern. The origin of the knot cluster $z_0$ was measured from the x-ray images. Knowing these values, parameters $\alpha$, $\beta$, and $\gamma$ could then be calculated.

The knot length $r_k$ cannot be measured accurately from a piece of square timber. However, to get some idea of this parameter, its value was estimated using experience gained from earlier knot analyses. The estimation was based on the size and appearance of the knot on the surfaces of the stem and the sawn timber.

The logs analysed included 82 clusters with 288 knots altogether. Note that some of the knots escape inspection, since they do not reach the sawn surface (see Figure 19). Some of the hidden knots would appear on the surfaces if the log were sawn in a different way.

The test objects were pine logs. Their lengths varied from 2.5 to 4.5 metres, and their diameter from 20 to 45 centimetres.

## 4.3 SIMULATIONS

Simulated images were synthesised taking into consideration typical shapes and density variations of knots and stems. The imaging geometry was the same as in actual log imaging. The number of clusters was 160, each cluster consisting of 1 to 6 knots, making a total of 590 knots.

The parameters used in the calculation of the synthetic log images are the following:

- radius of the log, $R$ = 20 cm
- radius of heartwood, $r_h$ = R/2
- distance of the knot end from the pith, $r_k$
- rotational angle of the knot, $\alpha$
- rise angle of the knot, $\beta$
- opening angle of the knot, $\gamma$
- density of sapwood, $\rho_{ws}$ = 800 kg/m$^3$
- density of heartwood, $\rho_{wh}$ = 500 kg/m$^3$
- density of knots, $\rho_k$ = 1000 kg/m$^3$

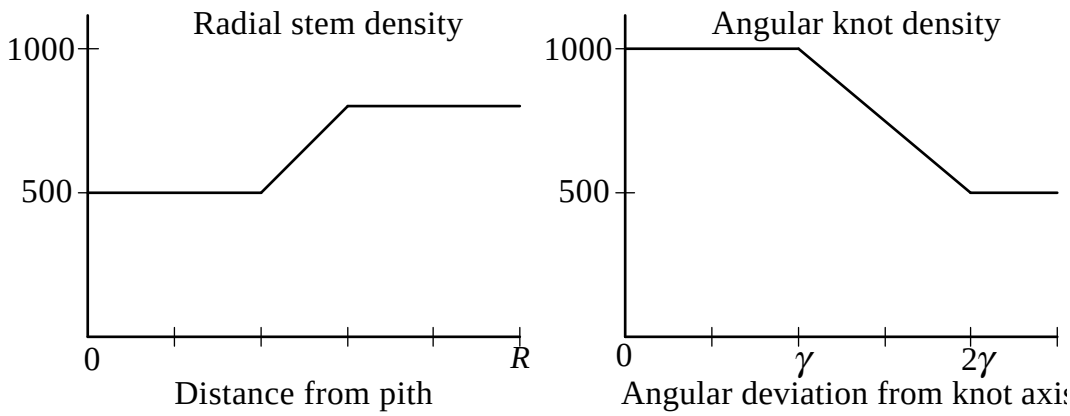


*Figure 20. The density model of the stem includes constant values for heartwood and sapwood with a linear transition between them (left). The density inside the knot is assumed to be constant; outside the knot the density decreases linearly towards the wood density (right). Densities are expressed in kg/m$^3$.*

- mass attenuation coefficient, $\mu/\rho$ = 0.017 m$^2$/kg.

The radial stem density and the knot density were assumed to follow the curves in Figure 20. In reality the density variation curves are smoother than those in the figure, of course, but this has no great effect upon the knot image. When a knot grows, it displaces surrounding wood, and forces its density to increase. We have estimated from x-ray images that the radius of the tighter wood around the knot is typically twice the radius of the knot, as is suggested by Figure 21.

In a small number of cases, the variables $\alpha$, $\beta$, $\gamma$, and $r_k$ were set manually to generate especially interesting test samples. However, mostly the parameter values were selected randomly by the simulation program. The constraints in doing this were:

- The rotational angles $\alpha$ of two neighbouring knots must differ by at least 40 degrees.
- The rise angle $\beta$ is limited to between 0 and 50 degrees.

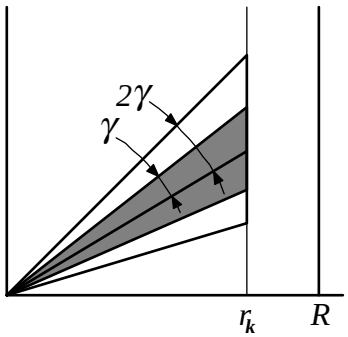


*Figure 21. The knot is modelled as a cone with opening angle $\gamma$. The knot is surrounded by denser wood up to angle $2\gamma$. The knot does not always reach the surface of the log (radius R) but ends at distance $r_k$ from the pith.*

- The opening angle $\gamma$ is between 4 and 10 degrees.
- The number of knots is from 1 to 6.

## 4.4 RESULTS

In this section we present the results of real-log experiments and simulations side by side and compare them. Appendix B contains the charts generated from the experimental data.

### 4.4.1 Angular distance between knots

The selection of candidate knot sectors is based on their evidence values. Our strategy is to look for local maxima in the evidence-versus-$\alpha$ curve. Additionally, we expect that knots do not reside very close to each other. Thus the evidence of a true knot sector should be greater than the evidence within a certain window of neighbouring sectors. The first test searches for the window size giving the best detection results. We compare window sizes of three, five, and seven sectors, which correspond to minimum knot distances of 20, 30, and 40 degrees.

Efficiency in knot sector detection means two things: (1) most of the true knot sectors should be found, and (2) not many false alarms should appear. Depending on the final optimisation arguments, the mutual importance of the two criteria may vary. The first principle coming to mind is to balance them by minimising their sum.

Looking at Figures B1 and B2 in appendix B, one can easily conclude that the neighbourhood of seven sectors is the best. Wider windows were not tested, but the results imply that it would have been unnecessary. The 7-sector window already results in more undetected knots than ghosts, meaning that the optimum has been passed. Using nine sectors in the comparison would also force the minimum knot distance to 50 degrees, which is hardly acceptable.

Besides the window size, a threshold value for evidence was determined in this analysis. Using the sum-of-error curves in Figures B1 and B2, the threshold was set to 0.0.

### 4.4.2 Over-all performance

Figure B3 and Table 4 show the ability of the method to detect knots. The number and volume of correctly detected, undetected, and false knots are compared to those of actual knots. It is not surprising that the results are better for simulated logs than for real ones. Noise from the natural structure of wood, and inaccuracies in the log positioning cause errors in x-ray images. Additionally, some of the false knots could have been true

*Table 4. The quantities of detected, undetected, and false knots in relation to the quantity of actual knots.*

| Result | Simulated logs | | Real logs | |
|---|---|---|---|---|
| | by volume | by number | by volume | by number |
| Detected | 0.96 | 0.91 | 0.88 | 0.87 |
| Undetected | 0.04 | 0.09 | 0.12 | 0.13 |
| False knots | 0.02 | 0.04 | 0.15 | 0.21 |

ones, even though they did not appear on the sawn surfaces. Of course, some small knots have escaped both the detection and the visual inspection.

The quantities of undetected and false knots balanced fairly well for both simulated and real logs. The detection parameters (evidence threshold, acceptance window) were the same in both cases, which suggests that they are not very sensitive to variations in object properties.

### 4.4.3 Evidence as a measure of confidence

One could expect that the evidence value of a sector is high, if there is a strong knot in that sector. Figure B4 in appendix B presents the probability of successful knot detection as function of evidence. Clearly the probability increases with growing evidence, and thus the sector evidence can be regarded as a confidence measure of knot findings. The level of probability seems to depend strongly on the object properties. For simulated knots, the detection probability is higher than 0.95 for all evidence values above zero, and thus its slope is small. The parameter has a greater importance in the case of real logs, as can be seen from the steepness of the lower curve in Figure B4.

### 4.4.4 Cluster classification

One way of classifying logs is based on their relative knot volume. This property may be called *knottiness*, or the *knot volume index*.

We split the clusters in the experiments into two halves both by their actual and estimates volumes, producing four classes. This was done separately for simulated and real logs. Table 5 summarises the results.

The percentages of correct classification were 98 % for simulated logs and 86 % for real logs. These figures are considered to be satisfactory. For comparison, Hagman (1992) reports 75 % success in similar tests with a gamma ray scanner.

The correlation between actual and estimated cluster volumes is presented in Figure B5. Figure B6 shows the same kind of charts for the maximal knot lengths in clusters. A linear regression model is applied to these test cases. The regression parameters have been collected into Table 6. Although the volume correlation is clear, one might wonder at the slope coefficients of 1.7 for simulated logs and 1.4 for real logs. The phenomenon is associated with the denser wood around knots, which is not counted in knot

*Table 5. The knot clusters are classified according their actual and estimated volumes as small and large using the median as threshold. The classification is done for both simulated logs and real logs.*

| Volume class | | Relative class size | |
|---|---|---|---|
| Actual | Estimated | Simulated logs | Real logs |
| small | small | 0.49 | 0.43 |
| large | small | 0.01 | 0.07 |
| small | large | 0.01 | 0.07 |
| large | large | 0.49 | 0.43 |

*Table 6. Linear regression coefficients indicating the dependence of estimated and actual volumes and the maximal knot lengths of clusters.*

| Coefficient | Simulated logs | | Real logs | |
|---|---|---|---|---|
| | Volume | Length | Volume | Length |
| Slope | 1.7 | 0.91 | 1.4 | 0.70 |
| Intercept | -23 | 1.6 | 67 | 3.8 |
| Correlation | 0.99 | 0.93 | 0.78 | 0.78 |

volume but which still affects the x-ray attenuation.

The results of the knot length test are not very representative. Looking at Figure B6, one can see that the sample points would be well located around the unity-slope line, but the regression curve is vague because of small the deviation of values.

### 4.4.5 Accuracy of co-ordinates and size measures

Figures B7, B8, and B9 visualise the error distributions of knot parameters $\alpha$, $\beta$, and $\gamma$, respectively. The corresponding standard error deviations have been calculated into Table 7.

A serious concern in Table 7 is the 17-degree error of $\alpha$ for real logs. This means that a notable share of detected knots would be located inaccurately on sawn surfaces. An acceptable and still realistic target for a standard error of $\alpha$ is 10 degrees. Our believe is that this target is reached when a complete three-projection system is available. Probably most of the error originates from the inconsistency of separate passes in the present one-projection imaging equipment.

Figures B10 and B11 show the correlation between actual and estimated volumes and lengths of individual knots. The corresponding regression parameters are presented in Table 8.

*Table 7. Standard error deviations of knot parameters.*

| Parameter | Simulated logs | Real logs |
|---|---|---|
| $\alpha$ | 9.1° | 17° |
| $\beta$ | 1.9° | 3.4° |
| $\gamma$ | 1.5° | 2.4° |

*Table 8. Linear regression coefficients indicating the dependence of estimated and actual volumes and lengths of individual knots.*

| Coefficient | Simulated logs | | Real logs | |
|---|---|---|---|---|
| | Volume | Length | Volume | Length |
| Slope | 0.87 | 0.22 | 0.85 | 0.61 |
| Intercept | 29 | 15 | 20 | 4.9 |
| Correlation | 0.88 | 0.53 | 0.71 | 0.66 |

# 5 DISCUSSION

## The course of the research

The target of the research project was to develop a method that would detect knots in logs using x-ray imaging. The system should work in real time without slowing down the sawing process. The basic idea was borrowed from computed tomography: three-dimensional object reconstruction from projections. However, traditional CT was soon discarded as unrealistic. Even the most modern fifth-generation CT systems were not capable of imaging logs at sawing speeds. We were forced to look for a simpler system that still could produce useful information for log sorting.

The conclusion from the speed requirements was that an imaging system with fixed projections should be used. It was not possible to rotate the object nor the imaging equipment without disturbing the process flow. The number of projections was limited to three for economic reasons.

Several reconstruction methods were tested with empirical data. In the first method, we tried to determine the knot directions from knot vectors extracted from 2-D projection images. The second one used the idea of determining convex hulls from their support lines. The third was based on backprojecting the projections to cross-section images that were then enhanced with angular filtering.

The first two trials yielded unsatisfactory results. The main problems were caused by overlapping knots and fading of knot patterns. Fading is due to the moisture content of the sapwood that attenuates x-rays badly. The third method seemed promising: angular filtering decreased streaks and ghost images, thus highlighting the knot pattern. The reason for this enhancement is that the filtering method matches well with the natural shape of knot patterns. The disadvantage of the method is its computational heaviness. It included several phases of pixel-level processing that would have been costly to implement.

We applied the idea of the third method, but modified it to reduce the pixel operations. The object space was expressed in cylindrical co-ordinates and divided into discrete volume elements. The sizes of the elements were chosen so that a coarse shape of a knot could be produced with a small number of elements. Typically, that number is in the order of one hundred. Each element is characterised by one single value after the backprojection; density variation inside the element is not considered.

## The results achieved

The output of the computation is two-level information on knots in the log. First, collective data on the knot cluster is obtained, including location and the bounding cylinder of the cluster, and the estimated knot volume in it. The bounding cylinder indicates how much knotless sapwood there is around the cluster. Secondly, the co-ordinates and size parameters of indi-

vidual knots are used to estimate the knot area on given sawing surfaces. This enables the selection of the product type that would yield the best economic result.

The hierarchy of the quality data is useful, because the three projection images are not always enough for exact detection of knots. The upper levels of information are quite reliable, offering a basis for log sorting. The second level, determining of detailed knot parameters, involves uncertainty when the number of knots in a cluster is high. However, these difficult cases could be classified to lower grades by the upper-level parameters. The easier ones with fewer knots are associated with high-quality logs, and then the knowledge of individual knots is of great importance. The calculated knot pattern can be tested for several blade set-ups to find the most beneficial one. The computation results include a confidence figure indicating the reliability of the estimated knot data. The confidence figure and the cluster volume help to decide which level of information should be used in log sorting.

To keep the hardware requirements reasonable, data is compressed quickly. After obligatory pre-processing at the pixel level, lines are averaged to slices of one centimetre thick. Thereafter, only the interesting parts of the images are processed, dropping out knotless wood and the areas outside the stem. At this point, the information has been reduced by a decade or more. The original imaging resolution is used when backprojecting the 2-D images to the cylindrical object space, but later a much coarser volume-element grid is applied. This reduces the information by another decade, and so megabytes have turned to tens of kilobytes. The results of a log are compressed into some hundreds of parameters.

The ability to find knots is expressed by the relative volumes of detected, undetected, and false knots. For real-log knots these figures were 0.88 : 0.12 : 0.15, and for simulated knots 0.96 : 0.04 : 0.02. It was difficult to compare the performance of our method with the performance other systems. Reliable data on visual inspection was not found. Hagman (1992) claims that their gamma ray scanner has a greater ability to classify logs than human inspectors typically have; thus we tried to repeat Hagman's test. The clusters in the experiments were split into two equal-sized halves, and then classified according to the computed results. The percentages of correct classification were 98 % for simulated logs and 86 % for real logs. For comparison, Hagman reports 75 % success with a gamma ray scanner.

The results from the simulated clusters were better than those from the real clusters. One reason for this is that the simulated clusters did not include natural noise present in real logs. Another reason is the different imaging quality. The simulated cases lack some inaccuracies involved with the present imaging system. Since only one source-detector pair was available in the tests, three passes were needed. This caused inaccuracy in both the rotational and longitudinal co-ordinates. It is quite reasonable to expect that the performance of a complete three-view system would fall between the levels obtained in the simulated and real cases of our experiments.

The detection system which applies our method is expected to have value in log sorting. The existing sorting systems are based on optical scan-

ners and visual inspection. They have some draw-backs: internal defects are not found, and the log dimensions cannot be measured under the bark.

**Problems and restrictions**

Reconstruction from a small number of projections has inherent uncertainty. In a general case, an infinite number of solutions may be derived from the same projections. The possibility of finding a correct result is better in our application, where the object is fairly simple. The object can be modelled, and constraints can be set to guide the reconstruction process. Nevertheless, there is no unique solution even in this case.

In our method, uncertain detail information is combined to find probable knot locations. In most cases this process is successful, but not always. For example, some knot patterns produce different results when imaged from different directions. This is because the projection angles affect how the shadows of real objects are cast on the cross-section, and how ghost images are generated. If we are fortunate, a certain pattern is located perfectly; on the other hand, the result from the same cluster may become vague with projection angles rotated.

Because the density of a volume element cannot be determined reliably, quality grading of knots is not possible. This is a pity, because it would be very useful to know if a knot appears on a sawn surface as sound, dry, or rotten.

One problem is the uncontrolled movements of the log on the conveyor; this may cause inaccuracy in the measurement of rotation angles and log geometry. The type of the conveyor must be selected carefully to avoid this difficulty.

**Computational factors**

The knot detection system must work in real time; the knot data is needed some seconds after the log has passed the inspection point. The data flow from the detector has to be at least 500 lines per second to cope with the conveyor speeds of up to 2.5 m/s used in present-day sawmills.

The computing problem at hand includes parallelism, a property which can be utilised in the implementation. The operations closely associated with imaging and pixelwise pre-processing are executed independently for each projection. This applies nearly as well to two-dimensional processing of the projection images. Only minor interaction between projections is needed when locating knot clusters. Also a significant part of the three-dimensional processing is involved with separate projections, and can be divided to three parallel processes.

Although the computation should run at the same average speed as the logs, rather long pipelining delay can be allowed. The log is cut into sections that are pipelined through the separate phases of the processing. Data buffering is needed between imaging, pre-processing, 2-D processing, and 3-D processing. However, the complete data from the whole log length need not be stored in the buffers, only the data from the latest section.

A real-time system has been implemented in another project, and it has been proved to work at a log speed of 2 m/s.

## Potential development subjects

The resolution of the cylindrical co-ordinate system was a compromise between accuracy and computational load. The sector angle is 10 degrees, the ring width 2 cm, and the slice thickness 1 cm. This means that the width of the largest elements in a log with 40-cm diameter is about 3.5 centimetres. If enough processing power were available, the sector and ring widths could be halved. Further resolution improvement is hardly cost-effective at the moment, since the requirements for processing capacity would increase dramatically.

The method uses many parameters that are set as default values based on knowledge of the properties of typical wood. Some of the parameters are densities and moisture percentages in heartwood, sapwood and knots. To be more flexible, the system should be able to adapt itself to variations in object characteristics. The present computation method disregards this. For example, the accuracy of the knot volume estimates will most probably get worse if the log is wet. In this case, adaptability would mean adjusting a density coefficient.

Important parameters are $\rho_{max}$ and $\rho_{crit}$, which are used to derive evidence values from densities. If the density of a volume element is over $\rho_{max}$, the knot evidence of the element is set to its highest value, while if it is under $\rho_{crit}$, the evidence is the lowest possible. These parameters are now determined from the maximum of the collective reconstruction (see Chapter 3.5.1). To add adaptivity, the variation of the stem density and the distribution of the knot pattern should be basis for the calculation of $\rho_{max}$ and $\rho_{crit}$.

A frequently asked question is about the number of projections. Three was selected by the project management fairly heuristically. Why not two or four? Using two projections does not seem very attractive. The ability for determining 3-D characteristics of a knot would be definitely worse than from three projections. The system would also lose the competition with optical instruments in the measurement of geometrical properties. The only use for a two-projection system would be the estimation of the total knot mass in logs. A four-projection system can produce more accurate results, but the value of the improvement is not clear without an extensive analysis of the sawing process.

## Other variables to be measured

We have concentrated here on knot detection only. Also other defects and log geometry parameters are important to know in the sawing process. X-ray imaging can also be applied to determine some of these properties.

The usable size of the log should be known to select a proper blade set-up. At present, optical instruments are used to measure the diameter at the top end. Some systems measure also the shape of the log. Moreover, the length and volume of the log can be obtained from scanned data. Optical scanners suffer from one handicap: they cannot establish log dimensions under the bark. Wood is what counts, not bark; thus x-rays are useful because of their capability to distinguish differences in material density.

The shape is characterised by such properties as taper, crook, and sweep. Shape determination is not just an imaging problem, but also a mechanical one. The conveyor system must assure a smooth and straight passage of the log through the imaging plane. If the log keeps jumping and turning on the conveyor, the shape information is distorted. To a certain extent, such problems can be compensated for with additional detectors.

The method described in Chapter 3 does not include shape computation at the moment. It only locates the over-bark log edges from the 2-D images for diameter calculation and image centring.

Other potential defects are rot, cracks, and resin pockets. Rotten wood is separated from sound wood by its low density. Obviously rotten heartwood in the butt end as well as other large areas of rot are recognised, but small defects associated with knot clusters are hopeless to find.

Typical cracks would escape this kind of inspection. A crack may be radial or ring-shaped, following the annual rings. The poor visibility of cracks in x-ray images is because their influence is distributed smoothly within the image. Resin pockets are gaps between annual rings filled with resin. They too are hard to detect if not especially large.

### Applying the method to other species of tree

The method was intended for pine only, and all the test objects were pine logs. Applying the method to different species of tree will require modifications. Spruce, for example, has a different knot distribution from that of pine: between knot clusters there are single knots here and there. A new way of finding the clusters and handling the single knots must be developed. Also the stem density profile is different, which affects the density parameters.

# 6 CONCLUSIONS

The basis for selecting x-ray technology for log inspection is its capability to see the internal properties of objects. Producing several projection images with x-rays and applying the principle of computed tomography would yield three-dimensional data on the log. However, no such inspection systems have been realised because of the high speed requirements of the sawing process.

The subject of this research work was a knot detection system with three fixed projections. It was known in advance that three projections cannot guarantee exact reconstruction of a 3-D object. Strong object details tend to hide weaker ones, or their shadows may combine into extra ghost details. However, utilising knowledge of the properties of knots and stems, we were able to develop a method for determining the coarse shapes of the knots. The inherent uncertainty from insufficient information is managed with a confidence figure, which is calculated for each candidate knot to judge the usefulness of the results. Our method is called the sector-oriented reconstruction technique, or SORT.

The performance of the method is expressed in terms of the relative volumes of detected, undetected, and ghost knots. In our experiments, these figures were 0.88 : 0.12 : 0.15 for real logs. Unfortunately, there was no performance data from the present-day systems for comparison.

Very knotty logs are the most difficult to analyse. Knots are not distinguished reliably enough to determine knot areas on planned sawing surfaces. However, estimates for total knot volume and thickness of knotless sapwood are obtained, and the log sorting is possible on the basis of these data. The knottiest logs are sorted into the lowest-quality classes anyhow, and detailed knot information is not so important. The best logs are easier to analyse, and more detailed information is obtained for the sorting.

It would be valuable for log sorting to know the knot quality, i.e. if a knot is fresh, dry, or dead. However, the density values determined from three projections are inaccurate, and thus the quality of individual knots cannot be calculated.

X-ray scanners are suitable for measuring important geometrical properties of the log, such as top end diameter, total volume, crook, sweep, and taper. The advantage of x-instruments over optical ones is that the log diameter can be measured under the bark.

The algorithms presented are tuned to knot detection in logs. Still, similar principles might be useful in developing an inspection system for objects other than logs, if the object can be modelled with simple geometrical forms. Examples of such objects are pipes, tiles, boards, bottles, or canned products.

# REFERENCES

Agi, I., Hurst, P.J. & Current, K.W. 1992. An expandable computed tomography architecture for non-destructive inspection. In: Connelly, J.M. & Cheung, S.M. (ed.) Applications of signal and image processing in explosives detection systems. Proc. SPIE 1824, Boston 16 - 17 November 1992. Bellingham, WA: SPIE - The International Society for Optical Engineering. Pp. 41 - 52. ISBN 0-8194-1025-X

Astola, J.T. & Campbell, T.G. 1989. On computation of the running median. IEEE Transactions on Acoustics, Speech, and Signal Processing, vol. 37, no. 4, pp. 504 - 507.

Aune, J.E. & So, P.K.L. 1989. Tukkiskanneri (Log scanner). Finnish patent application no. 893938. (In Finnish.)

Bjorkholm, P.J. & Wang, T.R. 1992. Explosive detection using three dimensional computer assisted image analysis. In: Connelly, J.M. & Cheung, S.M. (ed.) Applications of signal and image processing in explosives detection systems. Proc. SPIE 1824, Boston 16 - 17 November 1992. Bellingham, WA: SPIE - The International Society for Optical Engineering. Pp. 122 - 126. ISBN 0-8194-1025-X

Cheng, Y. & Kashyap, R.L. 1989. A study of associative evidential reasoning. IEEE Transactions on Pattern Analysis and Machine Intelligence, vol. 11, no. 6, pp. 623 - 631.

Compton, A.H. & Allison, S.K. 1960. X-rays in theory and experiment. 2nd ed. Princeton, NJ: D. van Nostrand. 828 pp.

Deutsch, M., Notea, A. & Pal, D. 1990. Inversion of Abel's integral equation and its application to NDT by x-ray radiography. NDT International, vol. 23, no. 1, pp. 32 - 38.

Eilbert, R.F. & Krug, K.D. 1992. Aspects of image recognition in Vivid Technology's dual-energy x-ray system for explosive detections. In: Connelly, J.M. & Cheung, S.M. (ed.) Applications of signal and image processing in explosives detection systems. Proc. SPIE 1824, Boston 16 - 17 November 1992. Bellingham, WA: SPIE - The International Society for Optical Engineering. Pp. 127 - 143. ISBN 0-8194-1025-X

Funt, B.V. & Bryant, E.C. 1987. Detection of internal log defects by automatic interpretation of computer tomography images. Forest Products Journal, vol. 37, no. 1, pp. 56 - 62.

Grace, L.A. 1992. Using external log geometry to determine log quality. In: Seminar on scanning technology and image processing on wood. Skellefteå, 30 August - 1 September 1992. Skellefteå: Luleå University, Dept. of Wood Technology. 24 pp.

Grundberg, S. & Grönlund, A. 1992. Log scanning - extraction of knot geometry. In: Seminar on scanning technology and image processing on wood. Skellefteå, 30 August - 1 September 1992. Skellefteå: Luleå University, Dept. of Wood Technology. 11 pp.

Grönlund, A. 1992. Benefits from knowing the interior of the log. In: Seminar on scanning technology and image processing on wood. Skellefteå, 30 August - 1 September 1992. Skellefteå: Luleå University, Dept. of Wood Technology. 7 pp.

Hagman, P.O.G. 1992. Automatic quality grading of logs with TINA, a gamma ray log scanner. In: Seminar on scanning technology and image processing on wood. Skellefteå, 30 August - 1 September 1992. Skellefteå: Luleå University, Dept. of Wood Technology. 5 pp.

Herman, G.T. 1980. Image reconstruction from projections. 2nd ed. New York: Academic Press. 318 pp. ISBN 0-12-342050-4

Hodges, D.G., Anderson, W.C. & McMillin, C.W. 1990. The economic potential of CT scanners for hardwood sawmills. Forest Products Journal, vol. 40, no. 3, pp. 65 - 69.

Huang, H.K. 1987. Elements of digital radiology. A professional handbook and guide. Englewood Cliffs, NJ: Prentice-Hall. 370 pp. ISBN 0-13-264136-4

Juhola, M., Katajainen, J. & Raita, T. 1991. Comparison of algorithms for standard median filtering. IEEE Transactions on Signal Processing, vol. 39, no. 1, pp. 204 - 208. ISSN 1053-587X

Kak, A.C. 1990. Image reconstruction from projections. In: Trivedi, M.M. (ed.) Selected papers on digital image processing. Bellingham, WA: SPIE - The International Society of Optical Engineering. Pp. 270 - 299. (SPIE Milestone Series, volume MS 17). ISBN 0-8194-0474-8

Kak, A.C. & Roberts, B.A. 1986. Reconstruction from projections: Applications in computerized tomography. In: Young, T.Y. & Fu, K.-S. (ed.). Handbook of pattern recognition and image processing. San Diego, CA: Academic Press. Pp. 649 - 693. ISBN 0-12-774560-2

Krestel, E. (ed.). 1990. Imaging systems for medical diagnostics. Berlin and Munich: Siemens Aktiengesellschaft. 630 pp. ISBN 3-8009-1564-2

Kärkkäinen, M. 1985. Puutiede. Sotkamo: Sallisen Kustannus. 346 pp. ISBN 951-99628-2-4 (In Finnish.)

Lee, S.C., Qian, G.S., Chen, J. & Hay, D.A. 1991. Scanning logs for knots. In: Johansen, P. & Olsen, S. (eds.) Proceedings of the 7th Scandinavian Conference on Image Analysis, Aalborg, August 13 - 16, 1991. Copenhagen: Pattern Recognition Society of Denmark. Pp. 513 - 520. ISBN 87-983795-1-8

Lévai, F., Tikkinen, J., Tarvainen, M. & Arlt. R. 1990. Feasibility studies of computed tomography in partial defect detection of spent BWR fuel. Helsinki: The Finnish Government Printing Centre. 41 pp. (Publications by the Finnish Centre for Radiation and Nuclear Safety STUK-A97). ISBN 951-47-4258-3

Prince, J.L. & Willsky, A.S. 1990. Reconstructing convex sets from support line measurements. IEEE Transactions on Pattern Analysis and Machine Intelligence, vol. 12, no. 4, pp. 377-389.

Pullan, B.R. (1979). Computed tomography limits and resolution. In: Kreel, L. (ed.) Medical imaging. A basic course. Aylesbury: HM+M Publishers. Pp. 10 - 22.

Puumalainen, P. 1993. Paperin laadun ja siihen valmistusprosessissa vaikuttavien tekijöiden on-line mittaukset. Dissertation. Lappeenranta: Lappeenranta University of Technology. 279 pp. (Research Papers 29). ISBN 951-763-774-8 (In Finnish.)

Roder, F. & Magnuson, P. 1989. High speed CT scanning of logs. In: Proceedings 3rd International Conference on Scanning Technology in Sawmilling, San Francisco 5 - 6 October 1989. San Francisco: Forest Industries. Pp. V1 - V9.

Rossi, D.J. & Willsky, A.S. 1984. Reconstruction from projections based on detection and estimation of objects - Parts I and II: Performance analysis and robustness analysis. IEEE Transactions on Acoustics, Speech, and Signal Processing, vol. 32, no. 4, pp. 886 - 906.

Sanz, J.L.C., Hinkle, E.B. & Jain, A.K. 1988. Radon and projection transform-based computer vision. Berlin: Springer-Verlag. 123 pp. ISBN 3-540-18396-5

Sikanen, P. 1989. X-ray computed tomography of a limited number of projections applied to the detection of branches in wood. Dissertation. Kuopio: University of Kuopio, Department of Physics. 86 pp. (Publications of the University of Kuopio, Natural Sciences, Original Reports 6/1989) ISBN 951-780-764-3

Som, S., Wells, P. & Davis, J. 1992. Automated feature extraction of wood from tomographic images. In: ICARCV '92, Second International Conference on Automation, Robotics and Computer Vision, Singapore 15 - 18 September 1992. Singapore: Nanyang Technological University. Pp. CV-14.4.1 - CV-14.4.5.

Tam, K.C. 1987. The construction and use of convex hulls in limited-angle computerized tomography. Journal of Nondestructive Evaluation, vol. 6, no. 4, pp. 189 - 203.

Taylor, F.W, Wagner, F.G, McMillin, C.W., Morgan, I.L. & Hopkins, F.F. 1984. Locating knots by industrial tomography - A feasibility study. Forest Products Journal, vol. 34, no. 5, pp. 42 - 46.

Usenius, A. 1988a. Automation in sawing of log and cant. Paper and Timber, vol. 70, no. 5, pp. 421 - 424.

Usenius, A. 1988b. Tomografiatekniikan (läpivalaisu) käyttömahdollisuudet puuteollisuudessa. SEITEC 88, Puualan seminaari, Seinäjoki 1.9.1988. 4 pp. (In Finnish.)

Viitaniemi, P. 1990. Puun sisäoksan ja normaalin runkopuun puuaineen erot. Espoo: VTT Forest Products Laboratory. Unpublished literature survey. 4 pp. (In Finnish.)

Wagner, F., Taylor, F., Steele, P. & Harless, T.E.G. 1989a. Benefit of internal log scanning. In: Proceedings 3rd International Conference on Scanning Technology in Sawmilling, San Francisco 5 - 6 October 1989. San Francisco: Forest Industries. Pp. V1 - V17.

Wagner, F.G., Taylor, F.W., Ladd, D.S., McMillin, C.W., & Roder, F.L. 1989b. Ultrafast CT scanning of an oak log for internal defects. Forest Products Journal, vol. 39, no. 11/12, pp. 62 - 64.

Wells, P., Shadbolt, P., Davis, J.R. & Davies, D.R. 1991. Tomographic imaging of wood. In: Paper Summaries of 1991 Industrial Computed Tomography II Professional Program, May 20 - 24, 1991, San Diego, CA. Columbus, Ohio: The American Society for Nondestructive Testing. Pp. 27 - 31. ISBN 0-931403-28-6

Wirkola, N.E. (ed.). 1983. Suomen paperi-insinöörien yhdistyksen oppi- ja käsikirja 2: Puumassan valmistus. 2nd edition. Helsinki: Teknillisten tieteiden akatemia. 1930 pp. ISBN 951-99117-1-5 (In Finnish.)

Zhu, D., Conners, R. & Araman, P.A. 1991a. CT image processing for hardwood log inspection. In: Tescher, A.G. (ed.) Applications of Digital Image Processing XIV. 22 - 26 July 1991, San Diego, CA. Bellingham, WA: SPIE. Pp. 232 - 243. (Proceedings of SPIE, Vol. 1567). ISBN 0-8194-0695-3

Zhu, D., Conners, R. & Araman, P.A. 1991b. 3-D image segmentation and recognition in an intelligent vision system. In: Casasent, D.P. (ed.) Intelligent Robots and Computer Vision X: Algorithms and Techniques. 11 - 13 November 1991. Bellingham, WA: SPIE. Pp. 286 - 297. (Proceedings of SPIE, Vol. 1607). ISBN 0-8194-0744-5

# AUXILIARY FUNCTIONS

## RADIAL DENSITY VARIATION

A log can be considered as a cylindrical object, the density of which varies with the distance from the axis. This is due to the way the tree grows: the vital functions take place in the sapwood near the surface, while the heartwood is dead. Thus the sapwood contains much humidity, and the heartwood is quite dry. The wet parts of the stem weaken the visibility of knots; this effect needs to be compensated for to obtain more accurate information on knot properties.

We handle the cross-section of the stem as a set of discrete rings, assuming a constant density within each ring. This is not exactly true, of course, but we are now interested only in rough estimates of averages. Each ring *j* is bordered by two circles, whose tangential rays from the source hit the detector at points $h_1(j)$ *and* $h_2(j)$ as shown in Figure A1. The passage length of ray *h* within ring *j* is denoted by *l(h, j)*.

Let us define *L(j, k)* as the sum of ray segments that belong to ring *k* and are parts of rays $h_1(j)$ ... $h_2(j)$:

$$L(j,k) = \sum_{h=h_1(j)}^{h_2(j)} l(h,k). \qquad \text{(A1)}$$

We have obtained an attenuation curve *p(h)* for a stem cross-section from normalised x-ray images. Curve *p(h)* represents the line integral of the density through the object.

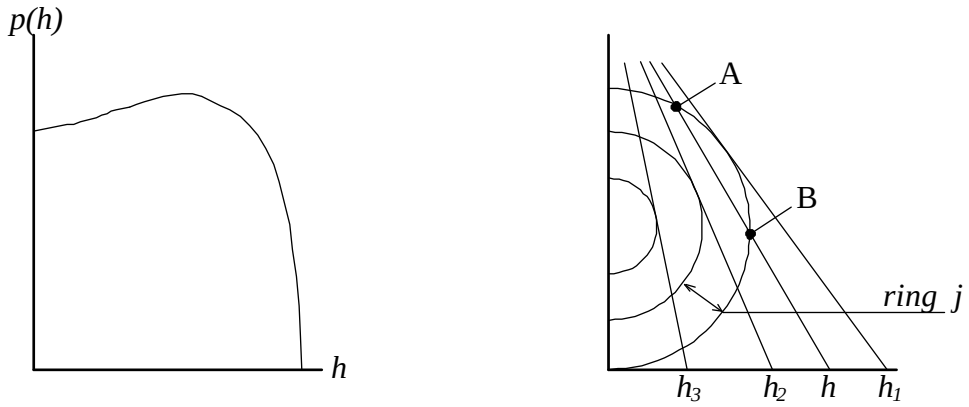


*Figure A1. On the left: curve p(h) shows typical attenuation of a log cross-section. On the right: the tangents of the inner and outer borders of ring j hit the detector at pixels* $h_1$ *and* $h_2$*. Respectively, the border pixels of the next inner ring are* $h_2$*-1 and* $h_3$*. The length of segment A-B of ray h is denoted as l(h, j) in the text.*

Starting from the outermost ring *n*, we add up both the ray segment lengths and attenuation values

$$L(n,n) = \sum_{h=h_1(n)}^{h_2(n)} l(h,n), \text{ and} \tag{A2}$$

$$P(n) = \sum_{h=h_1(n)}^{h_2(n)} p(h). \tag{A3}$$

A measure of the density of the outermost ring is the quotient of the above sums:

$$\rho(n) = \frac{P(n)}{L(n,n)}. \tag{A4}$$

Let us look at the next ring *n-1* having tangential border pixels $h_1 = h_1(n-1)$ and $h_2 = h_2(n-1)$. The values *p(h)* now come from both rings *n* and *n-1*. Knowing $\rho(n)$, *P(n-1)*, *L(n, n-1)*, and *L(n-1,n-1)*, we are able to solve $\rho(n-1)$. The following equation holds for any given *j*:

$$P(j) = \sum_{k=j}^{n} \rho(k) \cdot L(j,k), \tag{A5}$$

which derives to

$$\rho(j) = \frac{1}{L(j,j)} \cdot \left( P(j) - \sum_{k=j+1}^{n} \rho(k) \cdot L(j,k) \right). \tag{A6}$$

Thus the densities can be determined for all rings proceeding from the outside to the inside. Because of the nature of this reconstruction problem, the output is sensitive to any noise or irregularities in the object. One has to use conservative rules to keep the results within reasonable limits; for example, only a given percentual deviation from the average value may be allowed.

A density correction function $c_\rho(j)$ is now calculated from $\rho(j)$ and the typical knot density $\rho_k$ to enhance the projection image,

$$c_\rho(j) = \frac{\rho_k}{(\rho_k - \rho(j))}. \tag{A7}$$

Note that Equation (A7) is useful only if a proper estimate of $\rho_k$ is available. Some limits must be set on $c_\rho(j)$ to recover from exceptional situations.

## FUNCTION F FOR RISE ANGLE SEARCH

When candidate knot sectors are sought, the evidence values of the volume elements are saved in table *S(i, j, k)*. Indices *i*, *j*, and *k* refer to sectors, rings, and slices, respectively. Given a certain knot sector $i_c$, the table under consideration is two-dimensional, as shown in Figure A2. We should like to find out direction $\beta$ that matches best the evidence values in the table. The apex of angle $\beta$ is in the origin O in the lower left corner, and the right side of $\beta$ is the horizontal line passing through the origin.

We test a set of discrete values for $\beta$. For each $\beta$, a weighted sum is calculated using the weighting function F*( j, k, β)* defined as

$$\mathrm{F}(j,k,\beta) = A(j,k,\beta) / \sum_{k} A(j,k,\beta) . \qquad \text{(A8)}$$

As visualised by Figure A2, the function is determined from the element areas falling into an angle interval ($\beta - \Delta\beta$, $\beta + \Delta\beta$). We have used 5 degrees as the value of parameter $\Delta\beta$.

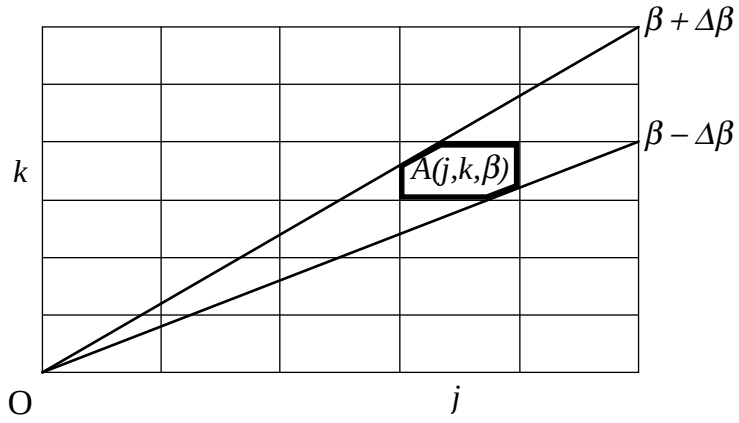


*Figure A2. A(j, k, β) is the area of element (j, k) bordered by lines at angles β - Δβ and β + Δβ.*

## MASK FUNCTION G FOR BACKPROJECTION

In the backprojection, we need a mask function G*(j, k, β)*, which is fairly similar to F*(j, k, β)*. With the same geometrical prerequisites, we define

$$\mathrm{G}(j,k,\beta) = A(j,k,\beta) / (\Delta r \cdot \Delta z) , \qquad \text{(A9)}$$

where $\Delta r$ and $\Delta z$ are the horizontal and vertical measures of the elements. So G*(j, k, β)* equals 1 if the element *(j, k)* totally belongs to the angle interval; otherwise its value is between 0 and 1.

We have used 15 degrees as the value of parameter $\Delta\beta$ when determining function G*(j, k, β)*.

## ESTIMATING THE KNOT VOLUME

We remember from elementary geometry that the volume of a cone with height $h$ and base area $A$ is

$$V = \frac{1}{3} hA . \tag{A10}$$

Let us examine the knot geometry according to Figure A3. The rise angle and the opening angle are denoted by $\beta$ and $\gamma$, respectively. The central point of the knot cone at $x = r_t$ is

$$z = \frac{1}{2} r_t \cdot \left[ \tan(\beta + \gamma) + \tan(\beta - \gamma) \right]. \tag{A11}$$

So the central point is not exactly in direction $\beta$. However, to simplify the equations, we approximate that

$$z \approx r_t \cdot \tan(\beta) . \tag{A12}$$

The error in co-ordinate $z$ caused by the approximation is less than 8 %, when $0° < \beta < 50°$ and $0° < \gamma < 10°$.

The vertical radius of the knot pattern ellipse is

$$b = \frac{1}{2} r_t \cdot \left[ \tan(\beta + \gamma) - \tan(\beta - \gamma) \right] = \frac{r_t \sin\gamma \cos\gamma}{\cos^2\beta \cos^2\gamma - \sin^2\beta \sin^2\gamma} \approx \frac{r_t \tan\gamma}{\cos^2\beta} . \tag{A13}$$

This time the basis for the approximation is that the sine term in the denominator is small compared to the cosine term. The error in diameter $b$ is less than 5 %, when $0° < \beta < 50°$ and $0° < \gamma < 10°$.

To calculate the horizontal radius of the ellipse, we first determine knot length $l$. Remembering the approximation of Equation (A12), we get

$$l = r_t / \cos\beta . \tag{A14}$$

The horizontal radius is now

$$a = l \tan\gamma = r_t \tan\gamma / \cos\beta . \tag{A15}$$

Substituting $A = \pi ab$ and $h = r_t$, we obtain from Equations (A10), (A13), and (A15)

$$V = \frac{\pi \cdot r_t^{\,3} \cdot \tan^2\gamma}{3\cos^3\beta} . \tag{A16}$$

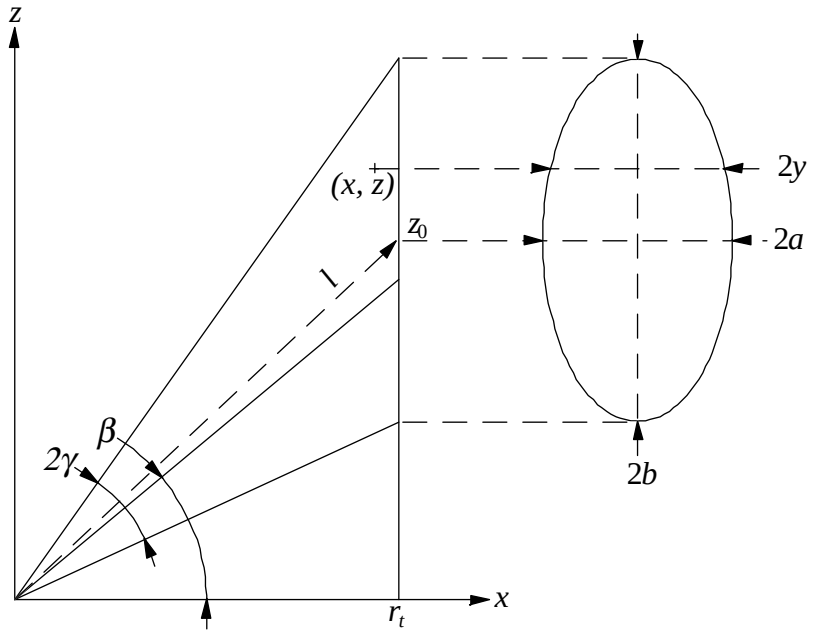


*Figure A3. The knot axis forms angle $\beta$ with the horizontal plane. The length of the knot is l while the horizontal component of its axis is $r_t$. The width of the cone is characterised by opening angle $\gamma$. The base of the cone is an ellipse with main diameters 2a and 2b.*

## ESTIMATING THE RISE AND OPENING ANGLES

Our aim is to determine the rising angle $\beta$ and the opening angle $\gamma$ from statistical properties of the knot profile. Let us take a look at the ideal knot cone shown in Figure A3. A straight line from the origin to a point ($x$, $z$) has a slope $z / x$. At that point, the cone has a thickness $2y$. The properties we need to calculate are the first and second moment of the slope $z / x$. The task is simplified dramatically when noticing that the distribution of the slope is exactly the same for every $x$. This is because the cross-section of the cone for all $x$ is the same ellipse, only scaled linearly with $x$:

$$\begin{aligned} &\frac{y^2}{a^2}+\frac{(z-z_0)^2}{b^2}=1, \\ &a = x\tan\gamma/\cos\beta, \\ &b = x\tan\gamma/\cos^2\beta, \\ &z_0 = x\tan\beta. \end{aligned} \qquad \text{(A17)}$$

The moments are calculated from the following integrals:

$$m_1 = \frac{1}{A}\int_z 2y\cdot\frac{z}{x}\,dz = \frac{1}{\pi ab}\int_{z_0-b}^{z_0+b}\frac{2az}{bx}\sqrt{b^2-(z-z_0)^2}\,dz, \qquad \text{(A18)}$$

$$m_2 = \frac{1}{A}\int_z 2y \cdot \frac{z^2}{x^2}\,dz = \frac{1}{\pi ab}\int_{z_0-b}^{z_0+b} \frac{2az^2}{bx^2}\sqrt{b^2-(z-z_0)^2}\,dz\,. \qquad \text{(A19)}$$

After some work, the results are obtained:

$$m_1 = \frac{z_0}{x} = \tan\beta\,, \qquad \text{(A20)}$$

$$m_2 = \frac{z_0^{\,2}}{x^2} + \frac{b^2}{4x^2} = \tan^2\beta + \frac{\tan^2\gamma}{4\cos^4\beta}\,. \qquad \text{(A21)}$$

Equation (A20) yields the rising angle b, which is simply

$$\beta = \tan^{-1}(m_1)\,. \qquad \text{(A22)}$$

The mean deviation is expressed through the moments by

$$D = \sqrt{m_2 - m_1^{\,2}} = \frac{\tan\gamma}{2\cos^2\beta}\,. \qquad \text{(A23)}$$

Opening angle $\gamma$ is thereby solved as

$$\gamma = \tan^{-1}\left(2D\cos^2\beta\right). \qquad \text{(A24)}$$

Conclusion: When the moments $m_1$ and $m_2$ are calculated from the knot pattern obtained in the reconstruction, Equations (A22) and (A24) help to estimate the parameters $\beta$ and $\gamma$.

# RESULTS OF EXPERIMENTS

The experiments included both simulated and real log images. Simulated images were synthesised having regard to typical shapes and density variations of knots and stems. The imaging geometry was the same as in actual log imaging. The number of clusters was 160 with 1 to 6 knots per cluster, making a total of 590 knots.

Tens of pine logs were imaged with the x-ray line camera developed in the project. Each log was imaged three times to obtain the three projections. Some of these logs were then sawn up into square timbers and visually inspected for knots. The logs analysed included 82 clusters and 288 knots altogether (as discovered by visual inspection).

The first test summary in Figures B1 and B2 is involved with the selection of candidate knot sectors. Each candidate sector has an evidence value that must be greater than the evidence of all other sectors within a given window. Window sizes of 3, 5, and 7 sectors are compared, the width of one sector being 10 degrees.

Figure B3 shows the efficiency of the method in detecting knots. The number and volume of correctly detected, undetected, and ghost knots are compared to those of the actual knots.

The sector evidence is considered as a confidence measure of a knot finding. Figure B4 presents the probability of successful knot detection as function of evidence.

Figures B5 and B6 portray the accuracy of determining volume and radius of clusters, whereas Figures B7 to B11 are involved with individual knot parameters.

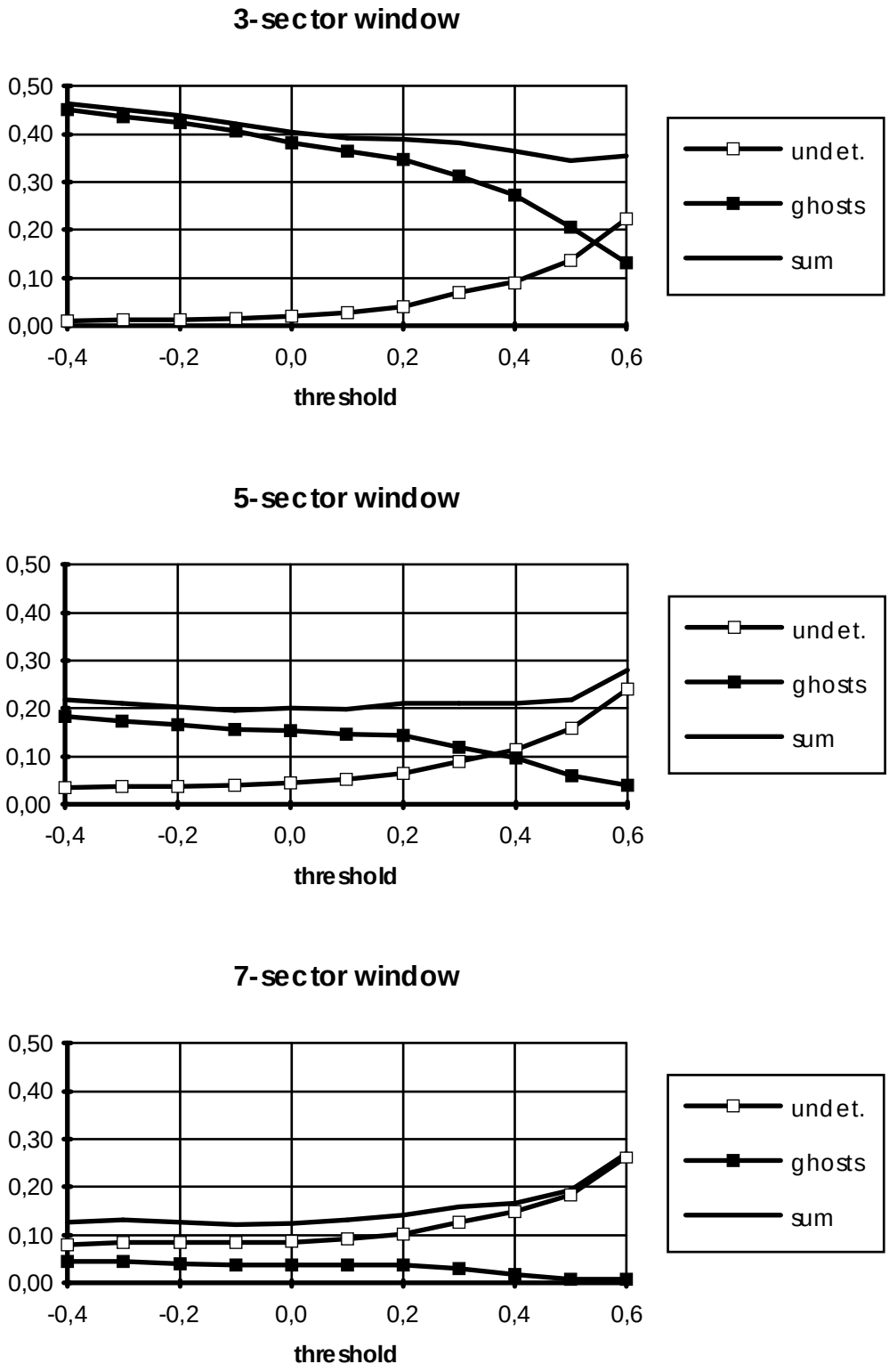


*Figure B1. The detection performance of the sector evidence as a function of the acceptance threshold for simulated test clusters. The numbers of undetected knots, ghost knots, and their sum are compared to the actual number of knots using three sizes of the acceptance window.*

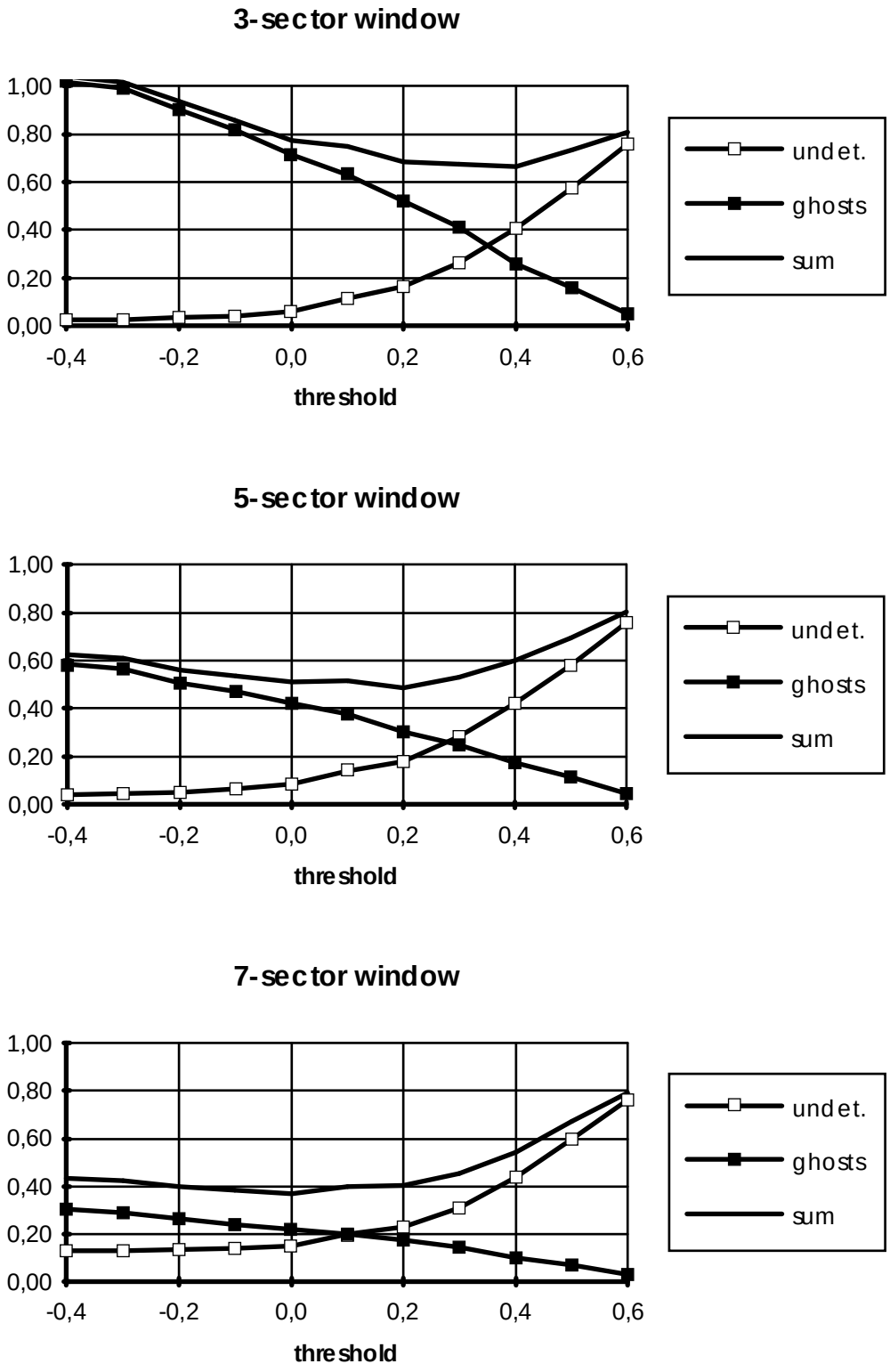


*Figure B2. The detection performance of the sector evidence as a function of the acceptance threshold for real-log test clusters. The numbers of undetected knots, ghost knots, and their sum are compared to the actual number of knots using three sizes of the acceptance window.*

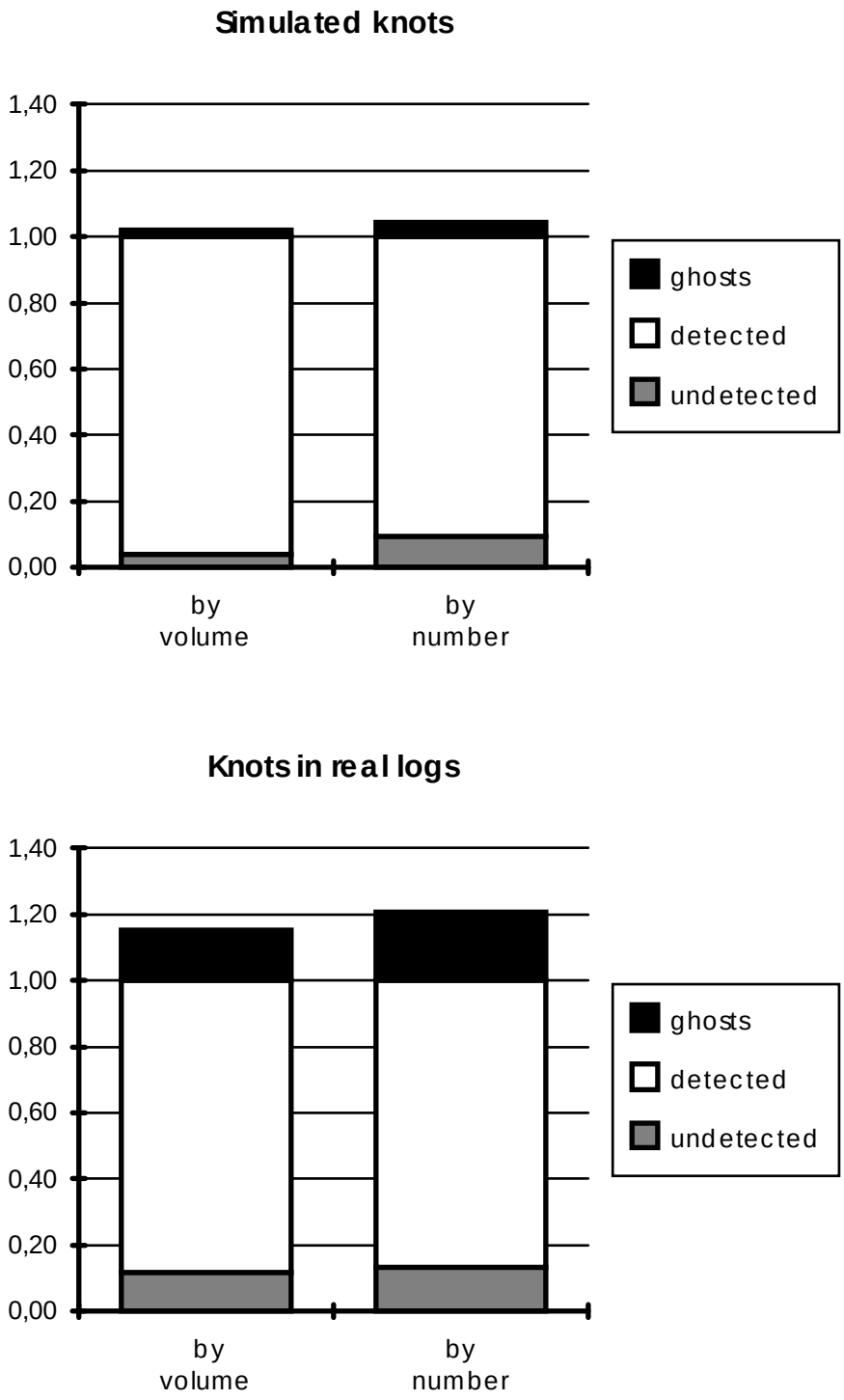


*Figure B3. The amounts of detected, undetected, and ghost knots are compared to the amount of actual knots by number and by volume.*

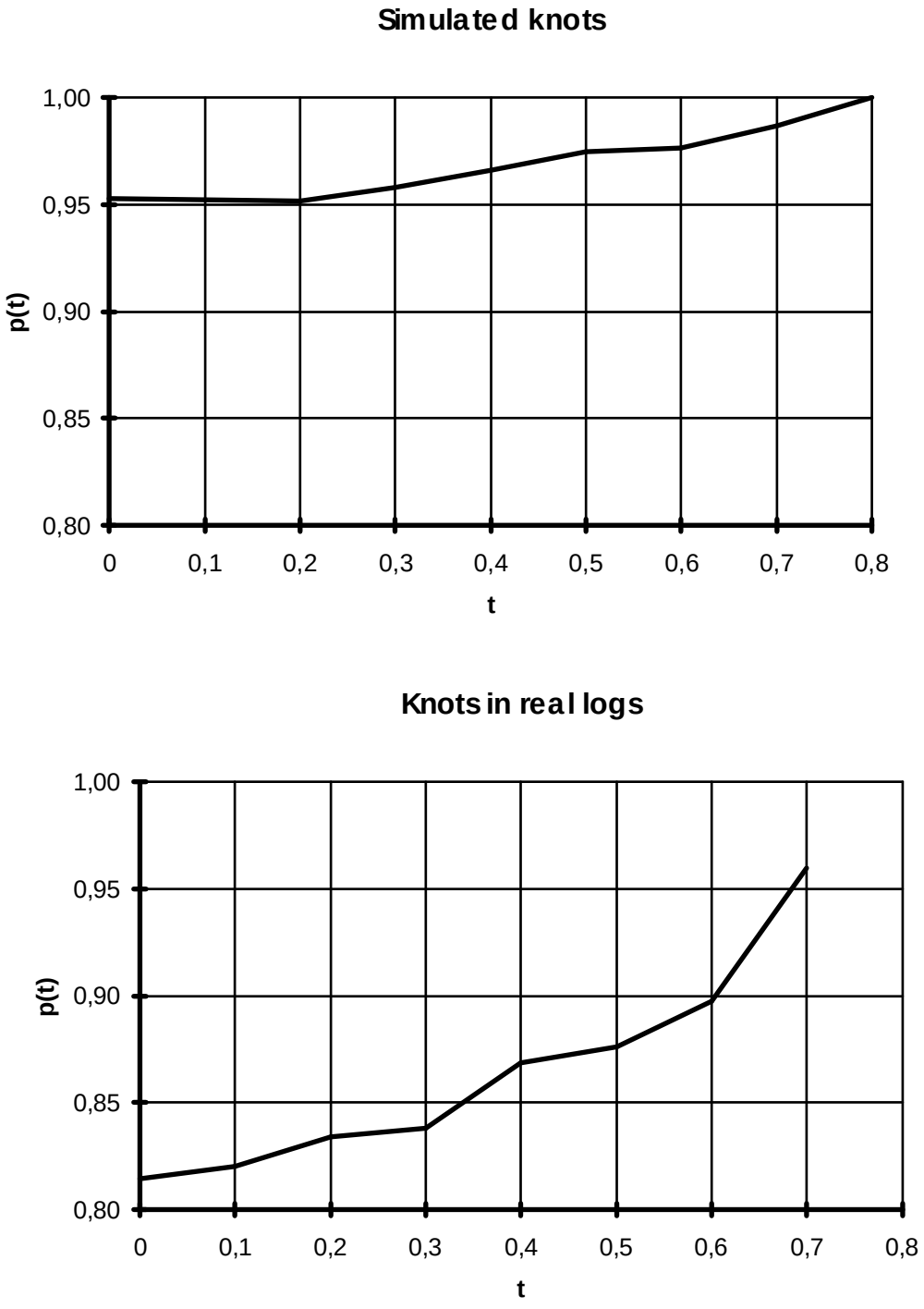


*Figure B4. The probability of correct knot detection as a function of sector evidence. Probability p(t) is defined as the number of detected knots per the actual number of knots when evidence ≥ t.*

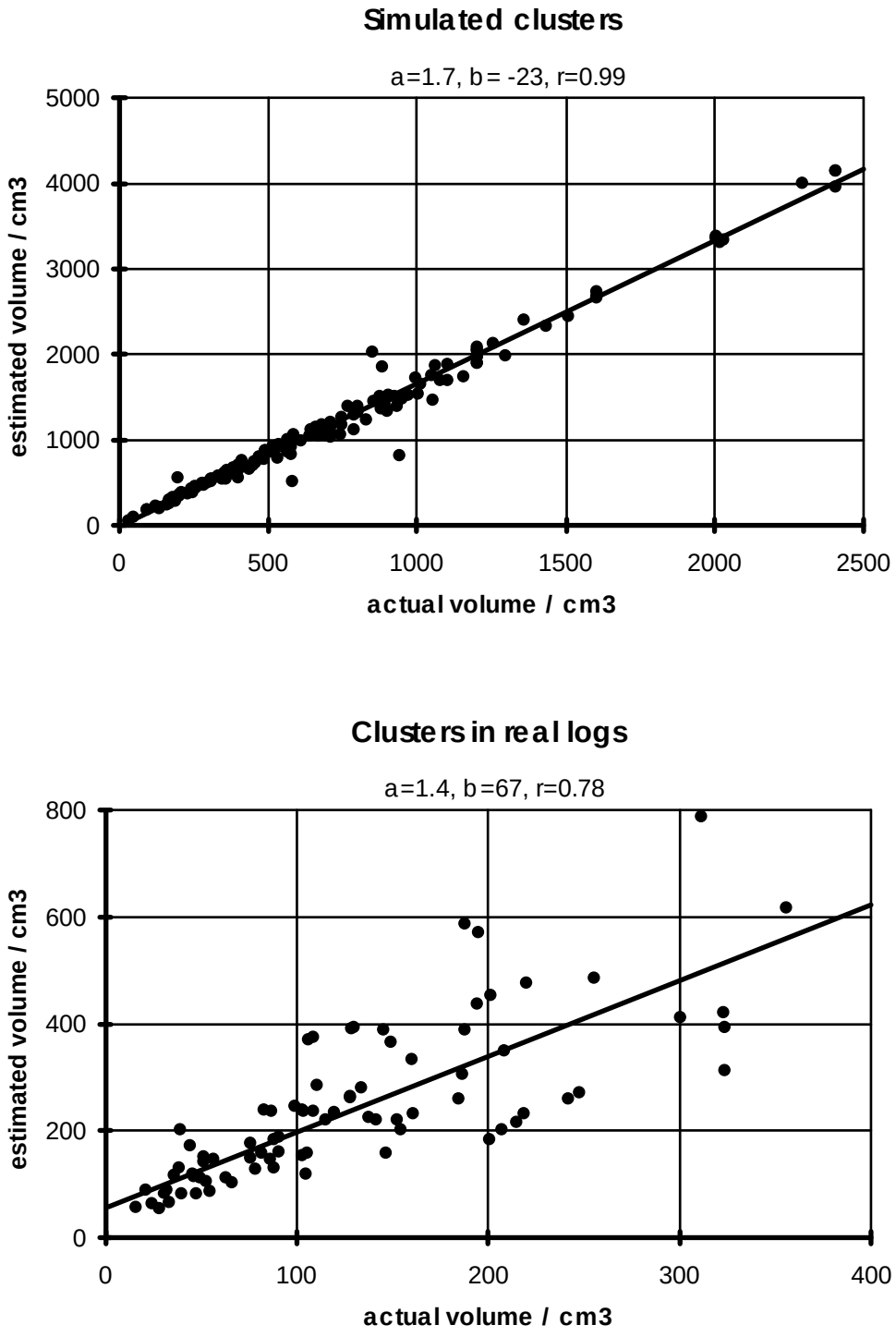


*Figure B5. Estimated volume versus actual volume of knot clusters. Parameters a and b are the coefficients of linear regression y = ax +b, and r is the corresponding correlation coefficient.*

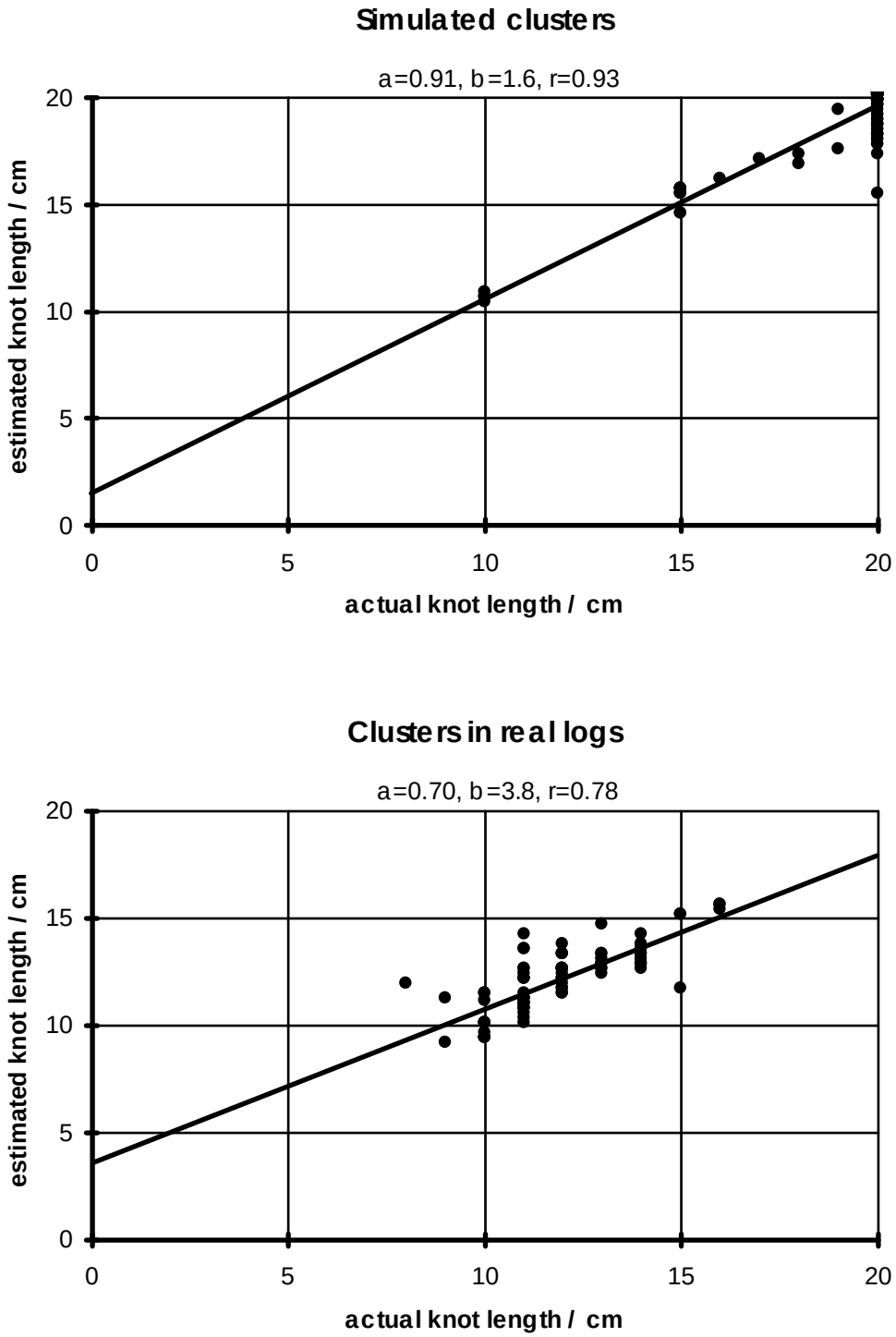


*Figure B6. Estimated knot length versus actual knot length of knot clusters. If there are several knots with different lengths in the cluster, the maximum among them is used. Parameters a and b are the coefficients of linear regression y = ax +b, and r is the corresponding correlation coefficient.*

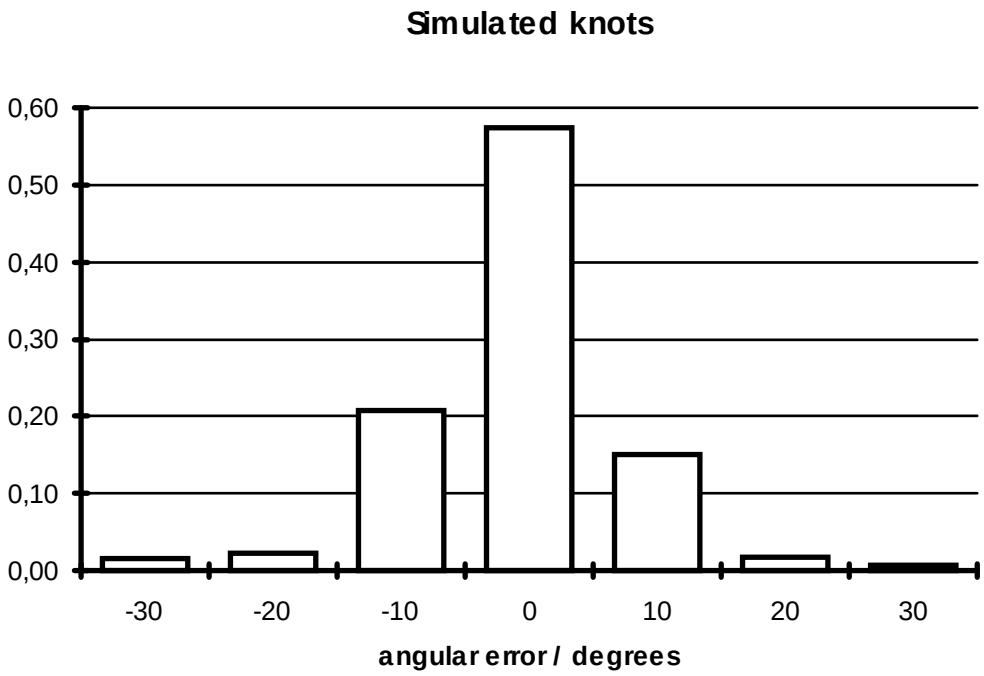


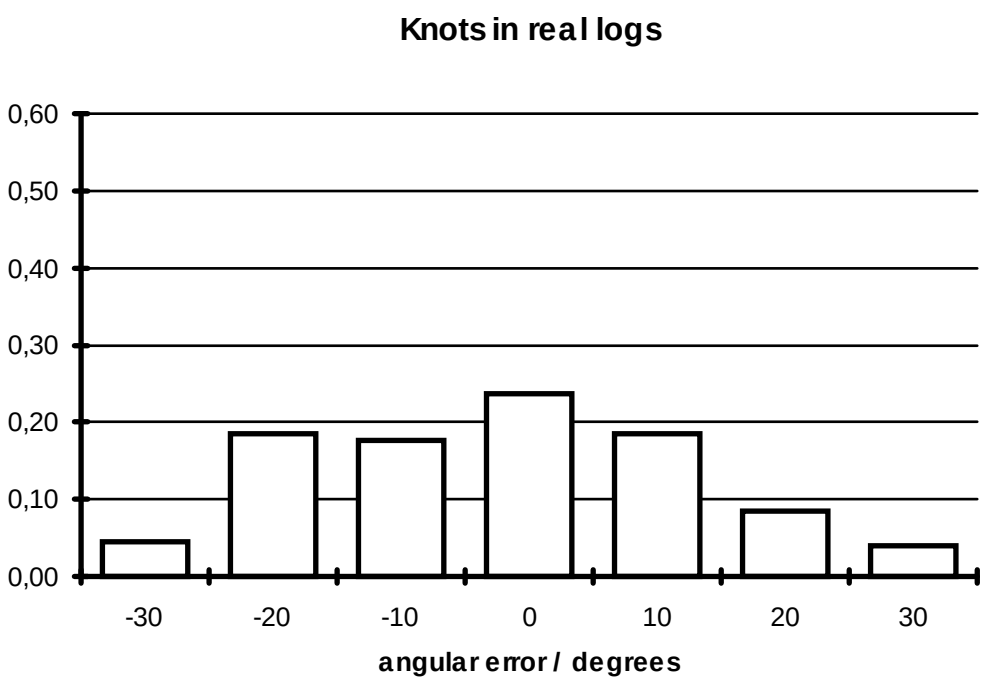


*Figure B7. Error distribution of rotation angle $\alpha$.*

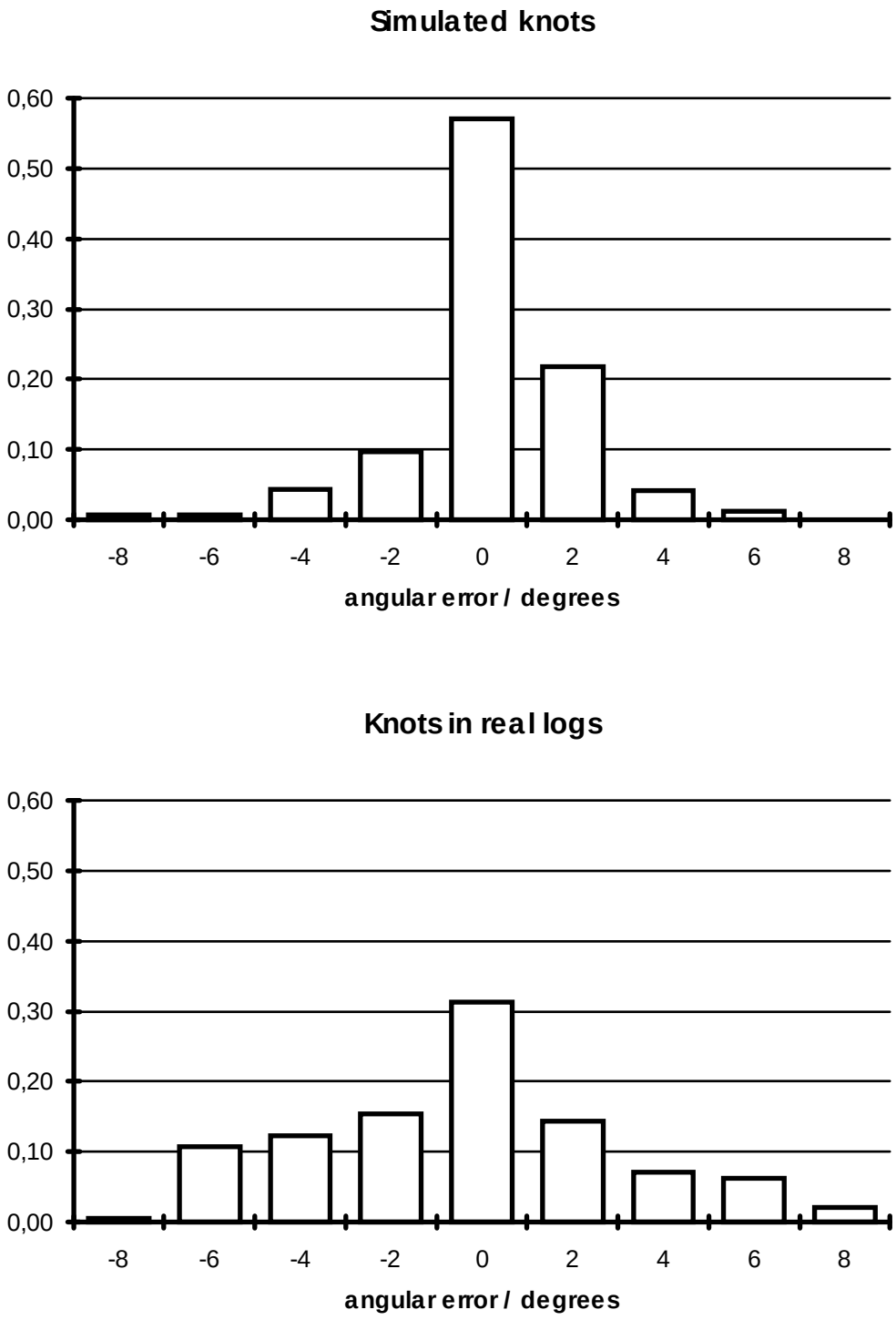


*Figure B8. Error distribution of rise angle β.*

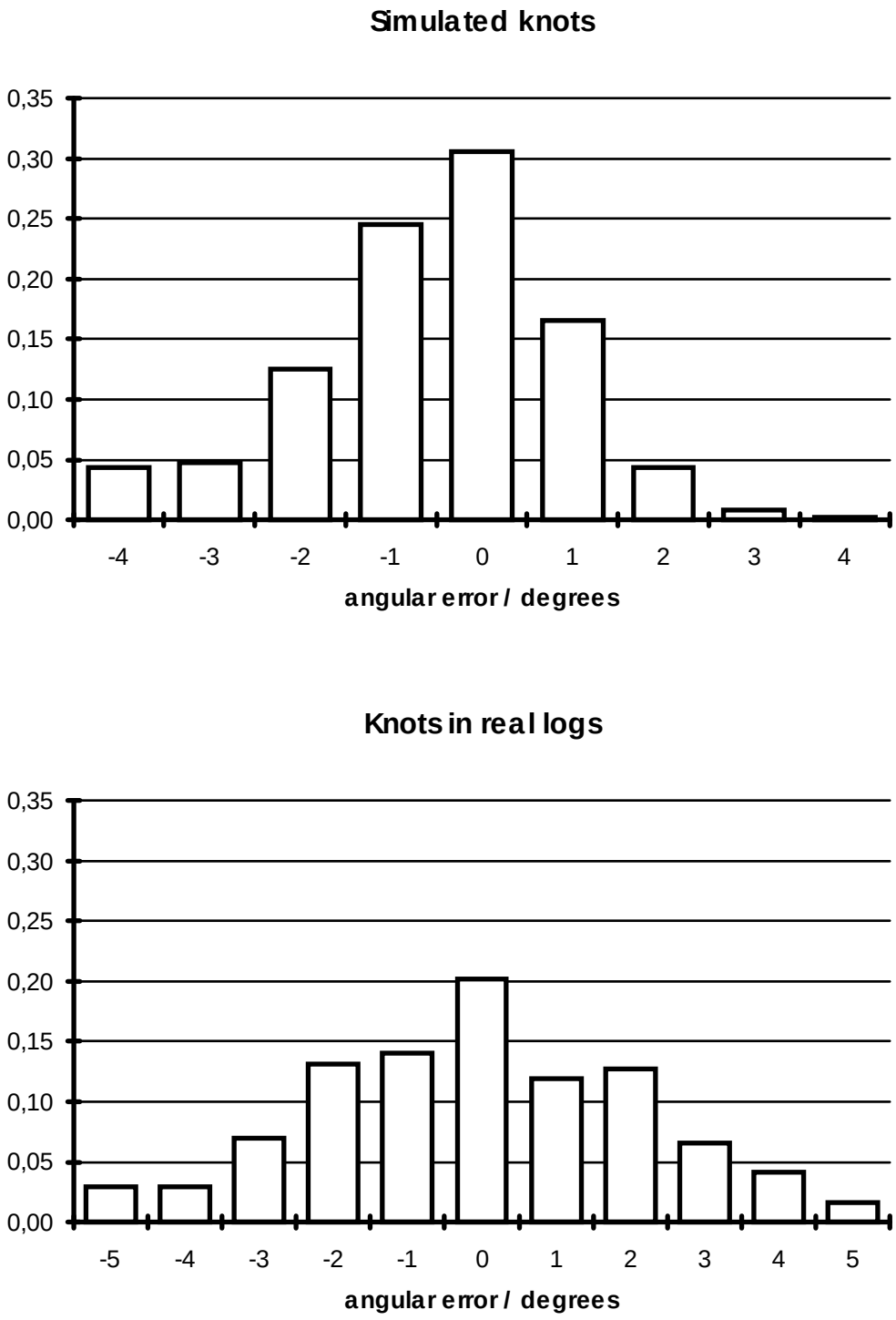


*Figure B9. Error distribution of opening angle $\gamma$.*

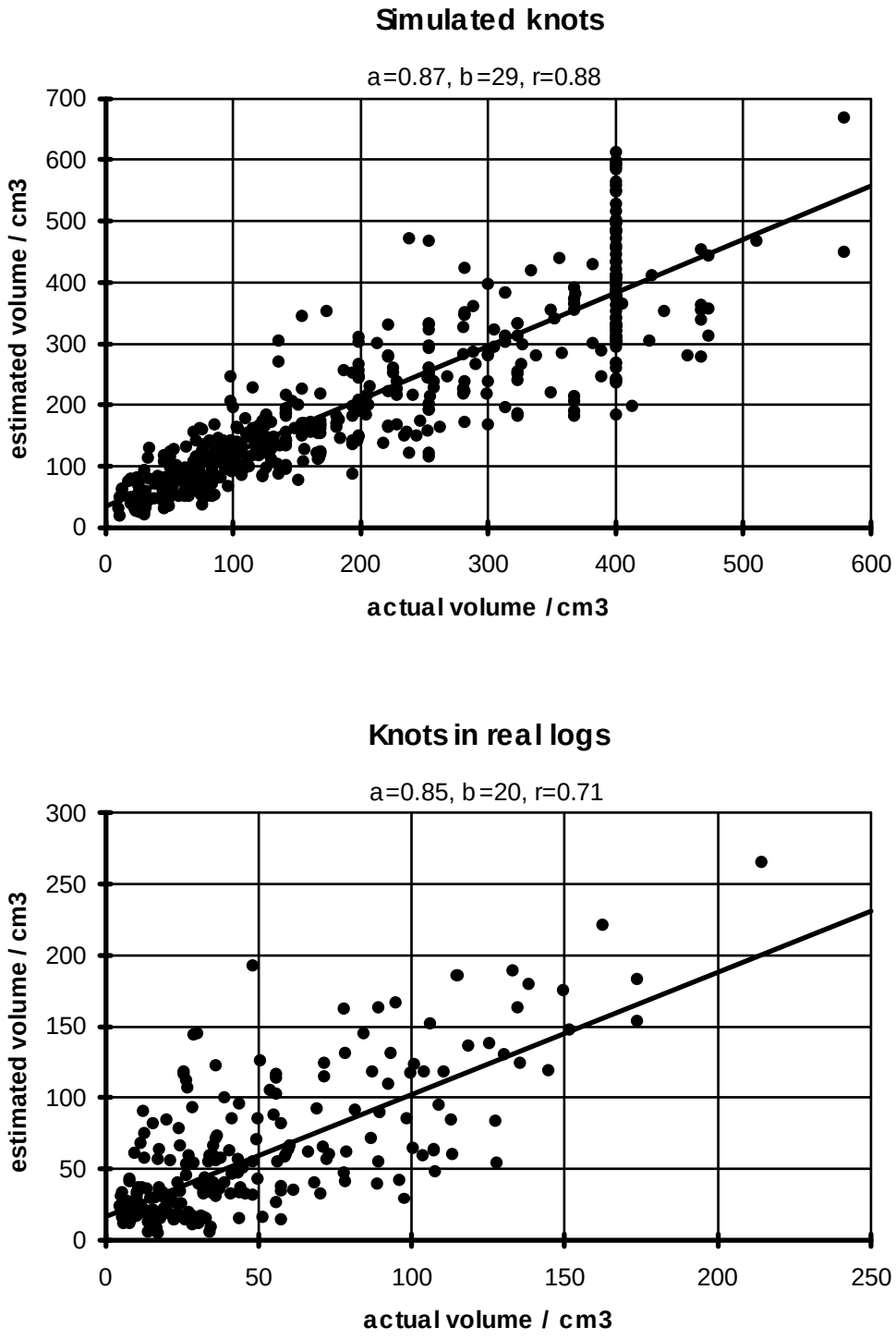


*Figure B10. Computed volume versus actual volume of individual knots. Parameters a and b are the coefficients of linear regression y = ax +b, and r is the corresponding correlation coefficient.*

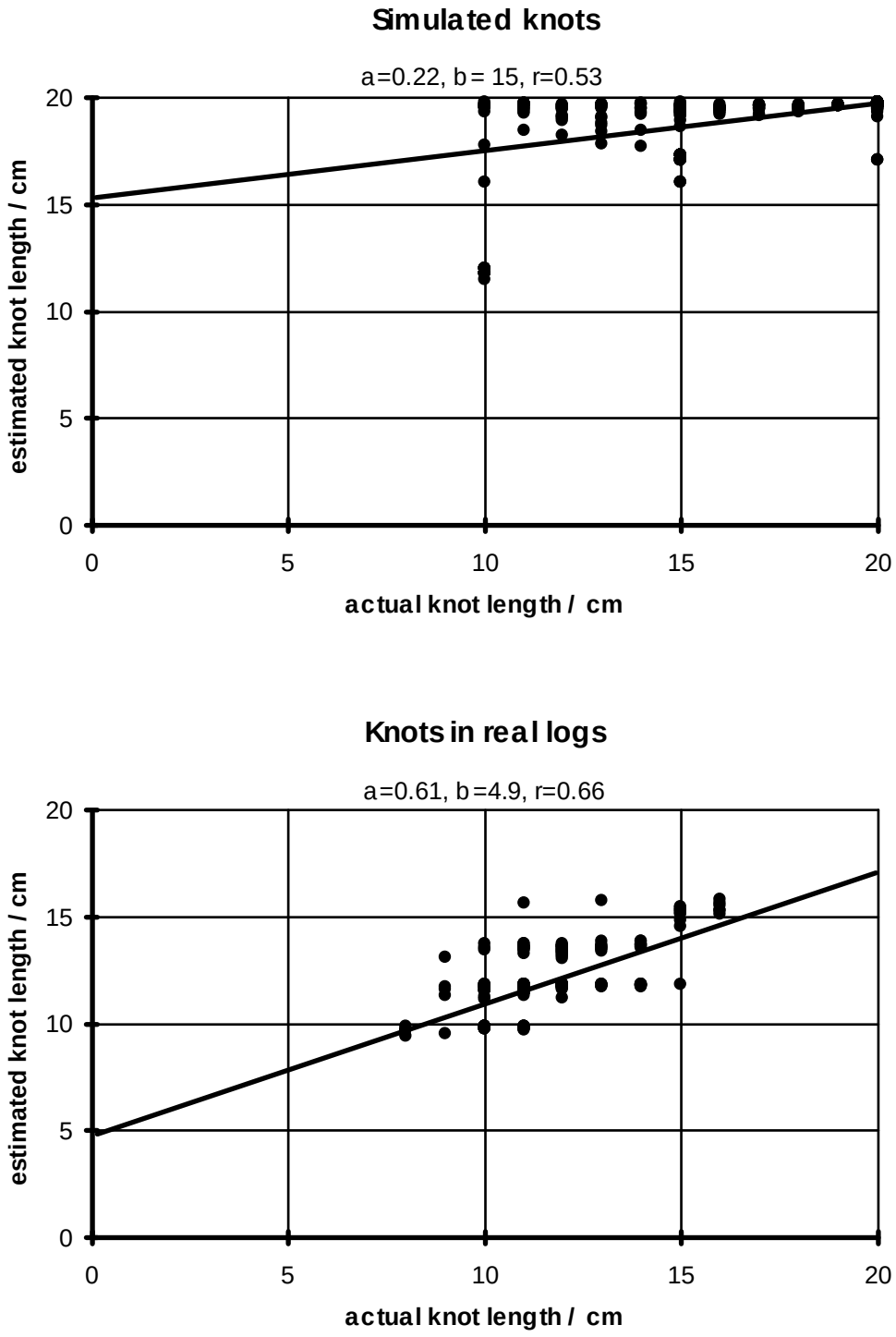


*Figure B11. Computed knot length versus actual knot length. Parameters a and b are the coefficients of linear regression y = ax +b, and r is the corresponding correlation coefficient.*

| Sarjanimeke | Sarjanumero | Vuosi |
|---|---|---|
| VTT Publications | | 1996 |

Tekijät
Markku Pietikäinen

Julkaisun nimi
Detection of knots in logs using x-ray imaging

| Sivuja | Liitesivuja | ISBN | |
|---|---|---|---|
| 70 | 18 | | |



Esittelyteksti

The study presents a method for computing three-dimensional properties of knots in logs from x-ray images. The basic idea comes from computed tomography, with the exception that only three projections are used. The number of projections cannot be much larger because the speed of the sawing process sets a tight limit for the imaging time.

Exact reconstruction of the object from three projections is not possible. However, good estimates for the size and co-ordinates of the knot patterns can be achieved with the method presented. The method uses *a priori* knowledge of typical shapes and densities of knots and stems, along with fuzzy reasoning when looking for candidate knot directions.

The performance of the method was experimented with simulations and analysing x-ray images of real logs.